Chapter 2
Supercontinuum Generation in Condensed Matter

Q. Z. Wang, P. P. Ho, and Robert R. Alfano

Abstract Self-phase modulation (**SPM**), induced-phase modulation (**IPM**), and cross-phase modulation (**XPM**) for supercontinuum generation are presented. Early day experimental measurements of supercontinuum in various materials are reviewed. Recent developments of supercontinuum generation covering from deep ultraviolet to far-infrared spectra are summarized in this chapter.

Keywords SPM · XPM · Supercontinuum · Nonlinear index of refraction · n_2

2.1 Introduction

Supercontinuum generation, the production of intense ultrafast broadband "white light" pulses, arises from the propagation of intense picosecond or shorter laser pulses through condensed or gaseous media. Various processes are responsible for continuum generation. These are called self-, induced-, and cross-phase modulations and four-photon parametric generation. Whenever an intense laser pulse propagates through a medium, it changes the refractive index, which in turn changes the phase, amplitude, and frequency of the incident laser pulse. A phase change can cause a frequency sweep within the pulse envelope. This process has been called *self-phase modulation (**SPM**)* (Alfano & Shapiro, 1970a). Nondegenerate *four-*

Q. Z. Wang (✉)
Technology Center 2600, United States Patent and Trademark Office, Alexandria, VA, USA
e-mail: quan-zhen.wang@uspto.gov

P. P. Ho
Department of Electrical Engineering, The City College of the City University of New York, New York, NY, USA
e-mail: pho@ccny.cuny.edu

R. R. Alfano
Department of Physics, The City College of the City University of New York, New York, NY, USA
e-mail: ralfano@ccny.cuny.edu

R. R. Alfano (ed.), *The Supercontinuum Laser Source*,
https://doi.org/10.1007/978-3-031-06197-4_2

*photon parametric generation (**FPPG**)* usually occurs simultaneously with the **SPM** process (Alfano & Shapiro, 1970a). Photons at the laser frequency parametrically generate photons to be emitted at Stokes and anti-Stokes frequencies in an angular pattern due to the required phase-matching condition. When a coherent vibrational mode is excited by a laser, stimulated Raman scattering (**SRS**) occurs. **SRS** is an important process that competes and couples with **SPM**. The interference between **SRS** and **SPM** causes a change in the emission spectrum resulting in *stimulated Raman scattering cross-**phase** modulation (**SRS-XPM**)* (Gersten et al., 1980). A process similar to **SRS-XPM** occurs when an intense laser pulse propagates through a medium possessing a large second-order χ^2 and third-order χ^3 susceptibility. Both second harmonic generation (**SHG**) and **SPM** occur and can be coupled together. The interference between **SHG** and **SPM** alters the emission spectrum and is called *second harmonic generation cross-phase modulation (**SHG-XPM**)* (Alfano et al., 1987). A process closely related to **XPM**, called *induced phase modulation (**IPM**)* (Alfano, 1986), occurs when a weak pulse at a different frequency propagates through a disrupted medium whose index of refraction is changed by an intense laser pulse. The phase of the weak optical field can be modulated by the time variation of the index of refraction originating from the primary intense pulse.

The first study of the generation and mechanisms of the ultrafast supercontinuum dates back to the years 1968–1972, when Alfano and Shapiro first observed the "white" picosecond continuum in liquids and solids (Alfano & Shapiro, 1970a). Spectra extending over ~6000 cm^{-1} in the visible and infrared wavelength region were observed. Over the years, improvements in the generation of ultrashort pulses from mode-locked lasers led to the production of wider supercontinua in the visible, ultraviolet, and infrared wavelength regions using various materials. Table 2.1 highlights the major accomplishments in this field over the past 20 years.

In this chapter, we focus on the picosecond supercontinuum generation in liquids, solids, and crystals. Supercontinuum generation in gases, **XPM**, and **IPM** is discussed by Corkum and Rolland (Chap. 7), Glownia et al. (Chap. 8), Baldeck et al. (Chap. 4), Agrawal (Chap. 3), and Manassah (Chap. 5), respectively.

2.2 Simplified Model

Before we go further, let us first examine the nonlinear wave equation to describe the self-phase modulation mechanism. A thorough theoretical study of supercontinuum generation has been dealt with in Chaps. 1, 3, and 5.

Table 2.1 Brief history of experimental continuum generation

Investigator	Year	Material	Laser wavelength/pulse width	Spectrum	Frequency (cm^{-1})	Process
Alfano, Shapiro	1968–1973	Liquids and solids	530 nm/8 ps or 1060 nm/8 ps	Visible and near **IR**	6000	**SPM**
Stolen et al.	1974–1976	Fibers	530 nm/ns	Visible UV,	500	**SPM**
Shank, Fork et al.	1983	Glycerol	620 nm/100 fs	visible, near **IR**	10,000	**SPM**
Corkum, Ho, Alfano	1985	Semiconductors Dielectrics	10 μm/6 ps	**IR**	1000	**SPM**
Corkum, Sorokin	1986	Gases	600 nm/2 ps 300 nm/0.5 ps	Visible and UV	5000	**SPM**
Alfano, Ho, Manassah, Jimbo	1986	Glass	1060 nm/530 nm/8 ps	Visible	1000	**IPM** (**XPM**)
Alfano, Ho, Wang, Jimbo	1986	ZnSe	1060 nm/8 ps	Visible	1000	**SHG-XPM** (**ISB**)
Alfano, Ho, Baldeck	1987	Fibers	530 nm/30 ps	Visible	1000	**SRS-XPM**

The optical electromagnetic field of a supercontinuum pulse satisfies Maxwell's equations:

$$\begin{aligned} \nabla \times \mathbf{E} &= -\tfrac{1}{c}\tfrac{\partial \mathbf{B}}{\partial t}, \\ \nabla \times \mathbf{H} &= \tfrac{1}{c}\tfrac{\partial \mathbf{D}}{\partial t} + \tfrac{4\pi}{c}\mathbf{J}, \\ \nabla \cdot \mathbf{D} &= 4\pi\rho \\ \nabla \cdot \mathbf{B} &= 0. \end{aligned} \tag{2.1}$$

Equations (2.1) can be reduced to (see Appendix)

$$\frac{\partial A}{\partial z} + \frac{1}{v_g}\frac{\partial A}{\partial t} = i\frac{\omega_0 n_2}{2c}|A|^2 A, \tag{2.2}$$

where $A(z, t)$ is the complex envelope of the electric field and $v_g = 1/(\partial k/\partial\omega)_{\omega_0}$ is the group velocity. The total refractive index n is defined by $n^2 = n_0^2 + 2n_0 n_2|A(t)|^2$, where n_2 is the key parameter called the nonlinear refractive index. This coefficient is responsible for a host of nonlinear effects: self- and cross-phase modulation, self-focusing, and the optical Kerr effect, to name the important effects. Equation (2.2) was derived using the following approximations: (1) linearly polarized electric field, (2) homogeneous radial fields, (3) slowly varying envelope, (4) isotropic and nonmagnetic medium, (5) negligible Raman effect, (6) frequency-independent nonlinear susceptibility $\chi^{(3)}$, and (7) neglect of group velocity dispersion, absorption, self-steepening, and self-frequency shift.

Denoting by a and α the amplitude and phase of the electric field envelope $A = ae^{i\alpha}$, Eq. (2.2) reduces to

$$\frac{\partial a}{\partial z} + \frac{1}{v_g}\frac{\partial a}{\partial t} = 0 \tag{2.3a}$$

and

$$\frac{\partial \alpha}{\partial z} + \frac{1}{v_g}\frac{\partial \alpha}{\partial t} = \frac{\omega_0 n_2}{2c}a^2. \tag{2.3b}$$

The analytical solutions for the amplitude and phase are

$$a(\tau) = a_0 F(\tau) \tag{2.4a}$$

and

$$\alpha(z, \tau) = \frac{\omega_0 n_2}{2c}\int_0^z a^2 dz' = \frac{\omega_0 n_2}{2c}a_0^2 F^2(\tau)\, z, \tag{2.4b}$$

where a_0 is the amplitude, $F(\tau)$ the pulse envelope, and τ the local time $\tau = t - z/v_g$. For materials whose response time is slower than pure electronic but faster than

molecular orientation (i.e., coupled electronic, molecular redistribution, libratory motion), the envelope is just the optical pulse shape. For a "pure" electronic response, the envelope should also include the optical cycles in the pulse shape.

The electric field envelope solution of Eq. (2.2) is given by

$$A(z,\tau) = a(\tau)\exp\left[i\frac{\omega_0 n_2}{2c}a_0^2 F^2(\tau)\,z\right]. \tag{2.5}$$

The main physics behind the supercontinuum generation by self-phase modulation is contained in Eq. (2.5) and is displayed in Fig. 2.1. As shown in Fig. 2.1a, the index change becomes time dependent, and therefore, the phase of a pulse propagating in a distorted medium becomes time dependent, resulting in self-phase modulation. The electric field frequency is continuously shifted (Fig. 2.1c) in time. This process is most important in the generation of femtosecond pulses (see Chap. 10 by Johnson and Shank).

Since the pulse duration is much larger than the optical period $2\pi/\omega_0$ (slowly varying approximation), the electric field at each position τ within the pulse has a specific *local* and *instantaneous frequency* at given time that is given by

$$\omega(\tau) = \omega_0 + \delta\omega(\tau), \tag{2.6a}$$

where

$$\delta\omega(\tau) = -\frac{\partial\alpha}{\partial\tau} = -\frac{\omega_0}{2c}n_2 a_0^2 z\frac{\partial F^2(\tau)}{\partial\tau}. \tag{2.6b}$$

The $\delta\omega(\tau)$ is the frequency shift generated at a particular time location τ within the pulse shape. This frequency shift is proportional to the derivative of the pulse envelope, which corresponds to the generation of new frequencies resulting in wider spectra.

Pulses shorter than the excitation pulse can be produced at given frequencies. It was suggested by **Y.R.** Shen many years ago that Alfano and Shapiro in 1970 most likely produced femtosecond pulses via supercontinuum generation. Figure 2.1c shows the frequency distribution within the pulse shape. The leading edge, the pulse peak, and the trailing edge are red shifted, nonshifted, and blue shifted, respectively.

The spectrum of **SPM** pulses is obtained by taking the Fourier transform of the complex temporal envelope $A(z, \tau)$:

$$A(\Omega) = \frac{1}{2\pi}\int_{-\infty}^{\infty} A(z,\tau)\exp[i\Omega\tau]\,d\tau, \tag{2.7}$$

Where $\Omega = \omega - \omega_0$. The intensity spectrum is given by

$$S(\Omega z) = \frac{c}{4\pi}|A(\Omega, z)|^2. \tag{2.8}$$

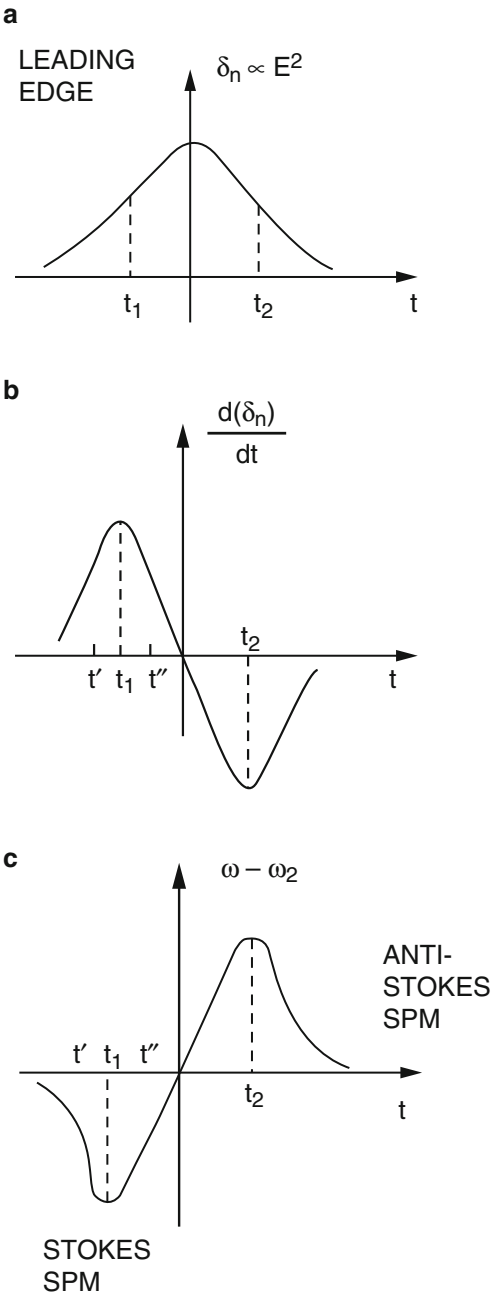

Fig. 2.1 A simple mechanism for **SPM** for a nonlinear index following the envelope of a symmetrical laser pulse: (**a**) time-dependent nonlinear index change; (**b**) time rate of change of index change; (**c**) time distribution of **SPM**-shifted frequencies $\omega(t) - \omega_0$

In practical cases, the phase of $A(z, \tau)$ is large compare with π, and the stationary phase method leads to

$$\omega(z)_{\max} = \frac{\omega_0}{2c} n_2 a_0^2 \left[\left. \frac{\partial F^2}{\partial \tau} \right|_{\tau_1} - \left. \frac{\partial F^2}{\partial \tau} \right|_{\tau_2} \right] z. \tag{2.9}$$

The intensity

$$\begin{aligned} S(\Omega, z) = & \left(\tfrac{c}{4\pi}\right)\left(\tfrac{4\pi c}{\omega_0 n_2 z}\right)\left\{ F^2(\tau') / \left. \tfrac{\partial F^2}{\partial \tau^2} \right|_{\tau'} + F^2(\tau'') / \left. \tfrac{\partial^2 F^2}{\partial \tau^2} \right|_{\tau''} \right. \\ & + 2 \frac{F(\tau') F(\tau'')}{\left[\left. \partial^2 F^2 / \partial \tau^2 \right|_{\tau'} \left. \partial^2 F^2 / \partial \tau^2 \right|_{\tau''} \right]^{1/2}} \\ & \left. \times \cos\left[\Omega(\tau' - \tau'') + \tfrac{\omega_0}{2c} n_2 a_0^2 z \left(F^2(\tau') - F^2(\tau'') \right) \right] \right\}, \end{aligned} \tag{2.10}$$

where $\Delta\omega_{\max}$ is the maximum frequency spread, τ_1 and τ_2 are the pulse envelope inflection points, and τ' and τ'' are the points of the pulse shape that have the same frequency.

An estimate of the modulation frequency $\delta\omega_M$ can be made by calculating the maximum number of interference minima and dividing this number into the maximum frequency broadening. A straightforward calculation leads to

$$\delta\omega_M \approx 2\pi \left. \frac{\partial F^2}{\partial \tau} \right|_{\tau_1} / F^2(\tau_1) \approx 2\pi \left. \frac{\partial F^2}{\partial \tau} \right|_{\tau_2} / F^2(\tau_2). \tag{2.11}$$

For a Gaussian laser pulse given by

$$F(\tau) = \exp\left[-\tau^2 / 2\tau_0^2 \right], \tag{2.12}$$

the modulation frequency of the **SPM** spectrum is (Alfano, 1972)

$$\delta\omega_M = \frac{4\pi}{\tau_0} \text{or } \delta\,\overline{v}_M = \frac{2}{\tau_0 c}. \tag{2.13}$$

Using this relation, the average modulation period of 13 cm^{-1} corresponds to an initial pulse duration of 5 ps emitted from mode-locked Nd: glass laser. The maximum frequency extent in this case is (Alfano, 1972)

$$\Delta\omega_{\max} \approx \frac{\omega_0 n_2 a_0^2 z}{c\tau_0}. \tag{2.14}$$

The maximum frequency shift (Eq. 2.14) indicates the following salient points:

- The frequency extent is inversely proportional to the pumping pulse duration. The shorter the incoming pulse, the greater the frequency extent. The first white

light band supercontinuum pulses were generated using picosecond laser pulses (Alfano & Shapiro, 1970a, b).
- The spectral broadening is proportional to n_2. The supercontinuum generation can be enhanced by increasing the nonlinear refractive index. This is discussed in detail in Sect. 2.6.
- The spectral broadening is linearly proportional to amplitude a_0^2. Therefore, multiple-excitation laser beams of different wavelengths may be used to increase the supercontinuum generation. This leads to the basic principle behind **IPM** and **XPM**. These processes are described by Baldeck et al. (Chap. 4) and Manassah (Chap. 5).
- The spectral broadening is proportional to ω_0 and z.

The chirp – the temporal distribution of frequency in the pulse shape – is an important characteristic of **SPM** broadened pulse. In the linear chirp approximation, the chirp coefficient C is usually defined by the phase relation

$$\alpha = C\tau^2. \tag{2.15}$$

For a Gaussian electric field envelope and linear approximation, the envelope reduces to

$$F^2(\tau) = \exp\left[-\tau^2/\tau_0^2\right] \approx 1 - \tau^2/\tau_0^2. \tag{2.16}$$

The linear chirp coefficient derived from Eqs. (2.5) and (2.16) becomes

$$C = \left(\frac{\omega_0}{2c}\right)\left(\frac{n_2 a_0^2 z}{\tau_0^2}\right). \tag{2.17}$$

Typical calculated **SPM** spectra are displayed in Fig. 2.2. The spectral densities of the **SPM** light are normalized, and β is defined as $\beta = \left(n_2 a_0^2 \omega_0 z\right)/2c$, which measures the strength of the broadening process. Figure 2.2a shows the spectrum for a material response time slower than pure electronic but faster than molecular orientation for $\beta = 30$ and $\tau = 0.1$ ps. The extent of the spectrum is about 7000 cm^{-1}. Figure 2.2b shows the **SPM** spectrum for a quasipure electronic response for $\beta = 30$ and $\tau = 0.1$ ps. Typical **SPM** spectral characteristics are apparent in these spectra.

2.3 Experimental Arrangement for SPM Generation

To produce the supercontinuum, an ultrafast laser pulse is essential with a pulse duration in the picosecond and femtosecond time region. A mode-locked laser is used to generate picosecond and femtosecond light pulses. Table 2.2 lists the available mode-locked lasers that can produce picosecond and femtosecond laser

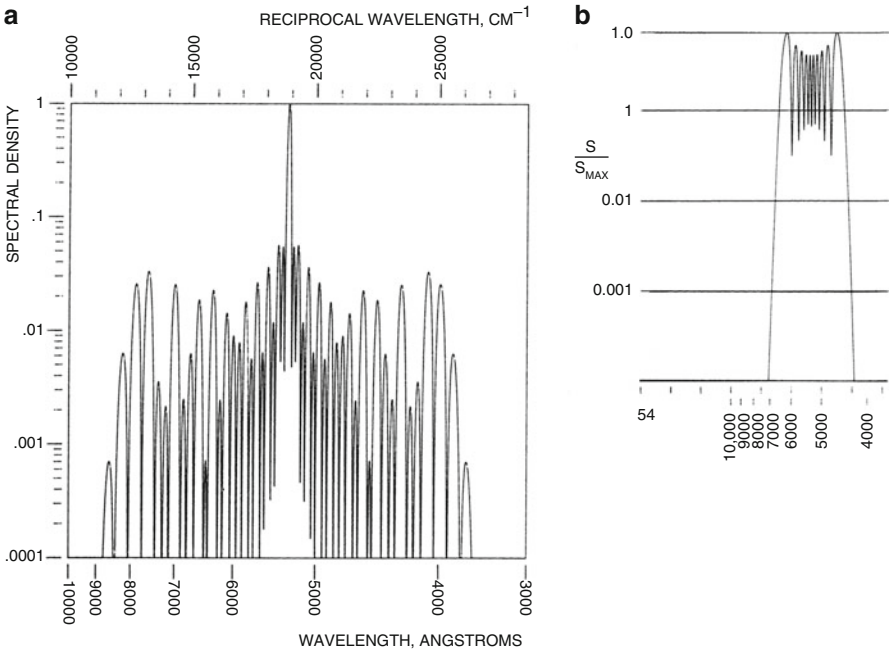

Fig. 2.2 Calculated **SPM** spectrum: (**a**) for response time slower than pure electronic but faster than molecular orientation: $\beta = 30$ and $\tau = 0.1$ ps; (**b**) for pure electronic response: $\beta = 30$ and $\tau = 0.1$ ps. (From Alfano, 1972)

Table 2.2 Available ultrafast mode-locked lasers

Oscillator	Wavelength (nm)	Pulse duration
Ruby	694.3	30 ps
YAG	1064	30 ps
Silicate glass	1060	8 ps
Phosphate glass	1054	6 ps
Dye	Tunable (SYNC or flash lamp)	5–10 ps
Dye + CO_2 + semiconductor switches	9300	1–10 ps
Dye (CPM)	610–630	100 fs
Dye + pulse compression (SYNC)	Tunable	300 fs
Dye + CPM (prisms in cavity)	620	27–60 fs
Dye + SPM + pulse compression (prisms and grating pairs)	620	6–10 fs

pulses. Measurements performed in the 1970s used a mode-locked Nd:glass laser with output at 1.06 μm with power of ~5×10^9 W and the second harmonic (**SHG**) at 530 nm with power of 2×10^8 W. Typically, one needs at least a few microjoules of 100-fs pulse passing through a 1-mm sample to produce continuum.

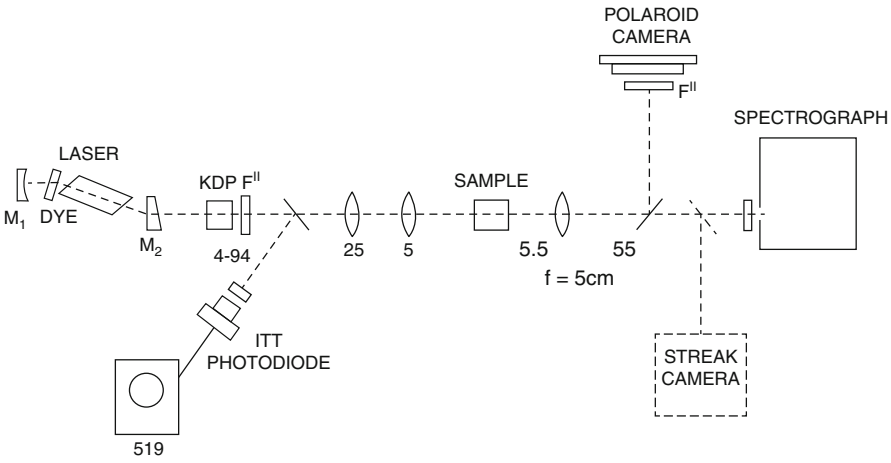

Fig. 2.3 Experimental arrangement for generating and observing supercontinuum and self-focusing. (From Alfano, 1972)

A typical experimental setup for ultrafast supercontinuum generation is shown in Fig. 2.3. Both spectral and spatial distributions are measured. The 8-ps **SHG** pulse of 5 mJ is reduced in size to a collimated 1.2-mm-diameter beam across the sample by an inverted telescope. For weaker excitation pulses, the beam is focused into the sample using a 10- to 25-cm focal lens. The typical sample length used is 10–15 cm for picosecond pulses and 0.1–1 cm for 100-f pulses. The intensity distribution of the light at the exit face of the sample was magnified 10 times and imaged on the slit of a spectrograph. The spectrum of each individual filament within the slit was displayed. Usually, there were 5–20 filaments. A thin quartz-wedge beam splitter was used to photograph filament formation of the Stokes (anti-Stokes) side of the spectra; three type 3–68 and three type 3–67 (two type 5–60) Corning filters were used to prevent the 530-nm direct laser light from entering the spectrograph. To reduce nonfilament light, a wire 2 mm in diameter was sometimes placed at the focal point of the imaging lens. Previously, spectra were taken on Polaroid type 57 film. At present, video systems such as an Silicon-intensified target (**SIT**) camera together with a **PC** computer are commonly used to display the spectra. Today, to obtain temporal information about the supercontinuum, a streak camera is added to the experimental system.

2.4 Generation of Supercontinuum in Solids

In the following sections, we review the experimental measurements of supercontinuum generated in condense matter. Topics discussed include supercontinuum

generation in various kinds of solids and liquids, optical glass fibers, liquid argon, liquid and solid krypton, magnetic crystals, and dielectric crystals.

The mechanisms behind **SPM** are discussed in Chap. 1 by Shen and Yang. In general, various mechanisms are responsible for **SPM** in condensed matter and give rise to the coefficient of the intensity-dependent refractive index n_2. These are the orientational Kerr effect, electrostriction, molecular redistribution, librations, and electronic distribution. In suitably chosen media (central-symmetric molecules), these frequency-broadening mechanisms may be distinguished from the electronic mechanism through their different time responses (Lallemand, 1966). The relation times for these mechanisms are given approximately by (Brewer & Lee, 1968)

$$\tau \text{ (orientation)} = \frac{4\pi}{3}\eta a^3/kT > 10^{-12}s, \tag{2.18}$$

$$\tau \text{ (molecular types)} = \frac{\langle x^2\rangle}{D} = \frac{6\pi\eta a\langle x^2\rangle}{kT} > 10^{-12}s, \tag{2.19}$$

$$\tau \text{ (libration about field)} = \sqrt{\frac{2I}{\alpha E_0^2}} > 10^{-12}s, \tag{2.20}$$

$$\tau \text{ (electronic)} = \frac{2\pi a_0\hbar}{e^2} > 1.5\times 10^{-16}s, \tag{2.21}$$

where η is the viscosity ($\eta = 0.4$ cp for liquids and $\eta = 10^6$ cp for glasses); a is the molecular radius; D is the diffusion coefficient ($\geq 10^{-5}$ cm/s for liquids) and x is the diffusion distance of the clustering, ~10^{-8} cm; I is the moment of inertia, $I_{\text{argon}} = 9.3\times 10^{-38}$ esu and $I_{CCl_4} = 1.75\times 10^{-38}$ esu; α is the polarizability, $\alpha_{\text{argon}} = 1.6\times 10^{-14}$ esu and $a_{CCl_4} = 1.026\times 10^{-24}$ esu; and E_0 is the amplitude of the electric field, taken as 10^5 esu, which is close to the atomic field. The response time for an electron distortion is about the period of a Bohr orbit, ~1.5×10^{-16} s. Thus, typical calculated relaxation time responses for diffusional motions are >10^{-11} s, while the electronic distortion response time is ~150 as.

With picosecond light pulses, Brewer and Lee (1968) showed that the dominant mechanism for filament formation should be electronic in very viscous liquids. Molecular rocking has been suggested as the cause of broadening and self-focusing in CS_2. The molecules are driven by the laser field to rock about the equilibrium position of a potential well that has been set up by the neighboring molecules. This mechanism is characterized by a relaxation time:

$$\tau_1 = \frac{\eta}{G} = 2.3\times 10^{-13}s, \tag{2.22}$$

where G is the shear modulus ~1.5×10^{10} dynes/cm and viscosity $\eta = 3.7\times 10^{-3}$ p for CS_2.

In solids, mechanisms giving rise to the coefficient of the intensity-dependent refractive index n_2 for picosecond pulse excitation are either direct distortion of electronic clouds around nuclei or one of several coupled electronic mechanisms: librational distortion, where electronic structure is distorted as the molecule rocks; electron-lattice distortion, where the electron cloud distorts as the lattice vibrates; and molecular distortion, where electronic shells are altered as the nuclei redistribute spatially. The electrostriction mechanism is rejected because it exhibits a negligible effect for picosecond and femtosecond pulses.

Typical supercontinuum spectra generated in solids and liquids using 8-ps pulses at 530 nm are displayed in Fig. 2.4. All continuum spectra are similar despite the different materials.

2.4.1 Supercontinuum in Glasses

Spectra from the glass samples show modulation (see Fig. 2.4a). The spectral modulation ranged from as small as a few wave numbers to hundreds of wave numbers. The filament size was approximately 5–50 μm. Typically, 5–20 small-scale filaments were observed. Occasionally, some laser output pulses from the samples did not show modulation or had no regular modulation pattern. Typical Stokes sweeps from these filaments were 1100 cm^{-1} in extradense flint glass of length 7.55 cm and 4200 cm^{-1} in both borosilicate crown (**BK**-7) and light barium (**LBC**-1) glass of length 8.9 cm. Sweeps on the anti-Stokes side were typically 7400 cm^{-1} in BK and **LBC** glasses. The sweep is polarized in the direction of the incident laser polarization for unstrained glasses.

2.4.2 Supercontinuum in Quartz

SPM spectra from quartz using an 8-ps pulse at 530 nm are similar to the spectra from glasses displayed in Fig. 2.4a. Typical Stokes sweeps from the filaments were 3900 cm^{-1} in a quartz crystal of length 4.5 cm, and the anti-Stokes sweeps were 5500 cm^{-1}.

2.4.3 Supercontinuum in NaCl

Sweeps of 3900 cm^{-1} in NaCl of length 4.7 cm to the red side of 530 nm were observed. Sweeps on the anti-Stokes side were about 7300 cm^{-1}. Some of the spectra show modulation with ranges from a few wave numbers to hundreds of wave numbers. Some laser shots showed no modulation or no regular modulation pattern. For unstrained NaCl, the supercontinuum light is polarized in the direction of the incident laser polarization.

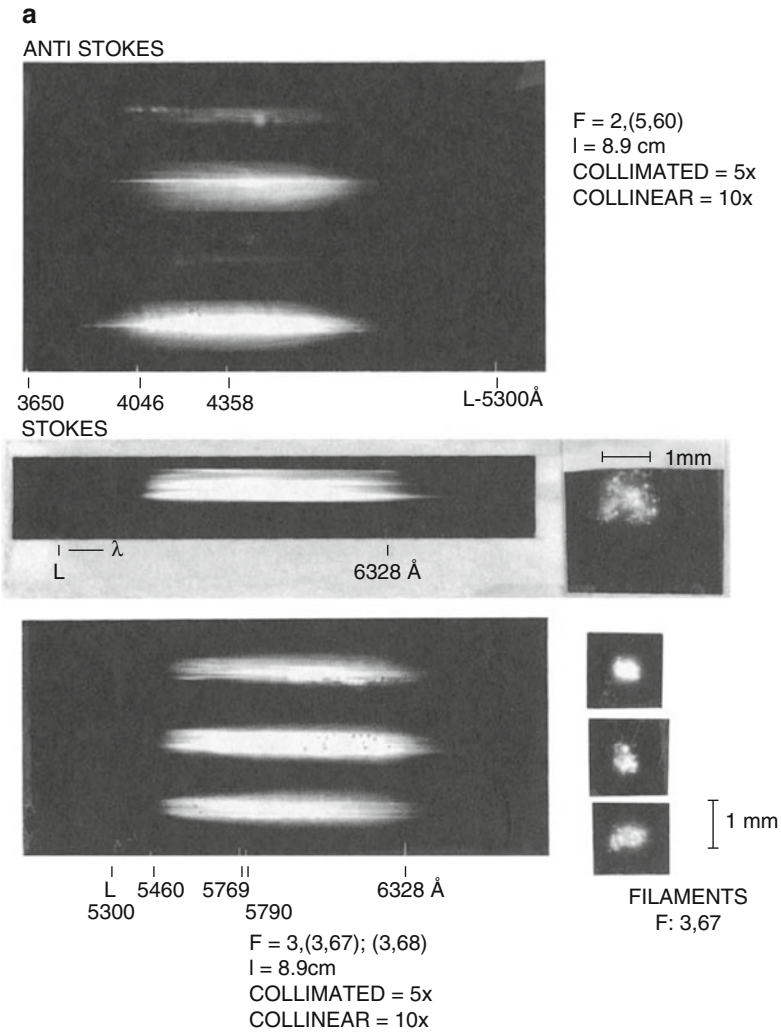

Fig. 2.4 Supercontinuum spectra from various kind of solids and liquids. (**a**) Stokes and anti-Stokes **SPM** from **BK**-7 glass and filament formation for different laser shots. The filaments are viewed through Corning 3–67 filters. (**b**) Stokes and anti-Stokes **SPM** from calcite for different laser shots. The laser beam propagates as an O-wave through the sample. (**c**) Stokes and anti-Stokes **SPM** spectra from calcite for different laser shots. The laser beam propagates as an E-wave. (From Alfano, 1972)

2.4.4 Supercontinuum in Calcite

Sweeps of 4400 cm^{-1} and 6100 cm^{-1} to the Stokes and anti-Stokes sides of 530 nm were observed in a calcite crystal of length 4.5 cm (see Fig. 2.4b). Some

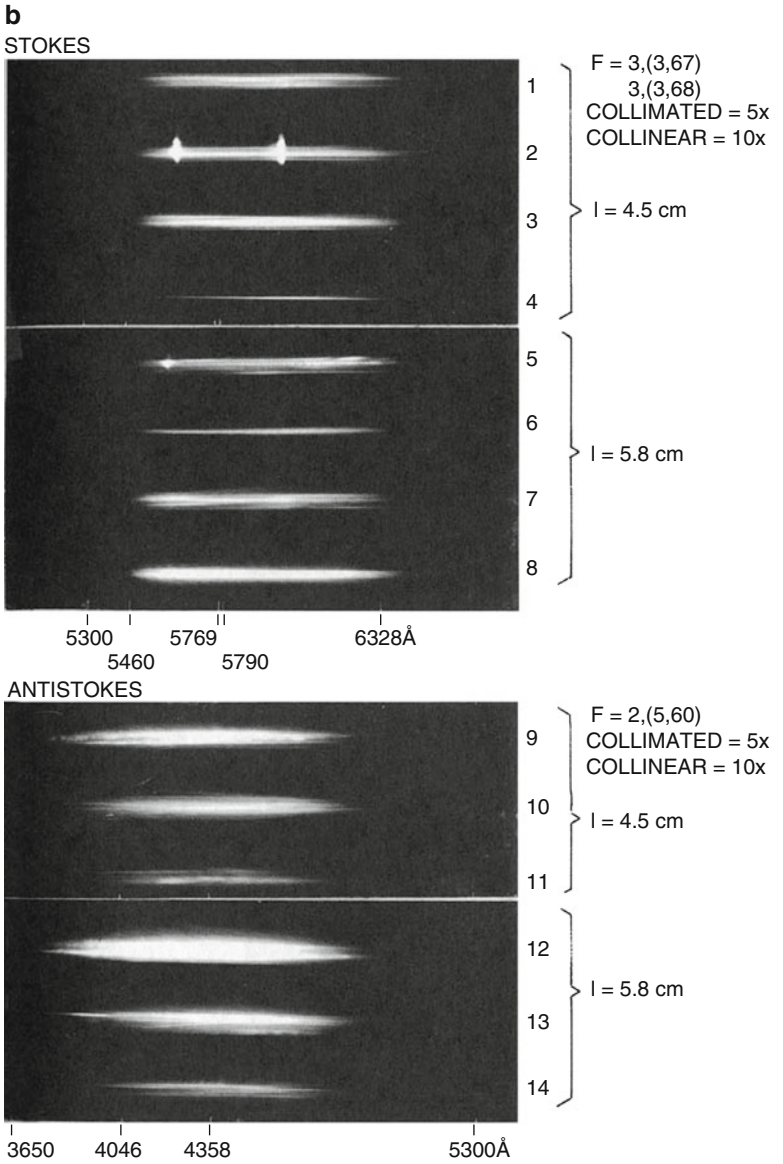

Fig. 2.4 (continued)

spectra showed modulation structure within the broadened spectra; some showed no modulation or no regular modulation pattern. The exit supercontinuum light has same polarization as the incident laser. The **SRS** threshold is lower for laser light traveling as an **O**-wave than an **E**-wave. **SPM** dominates the **E**-wave spectra.

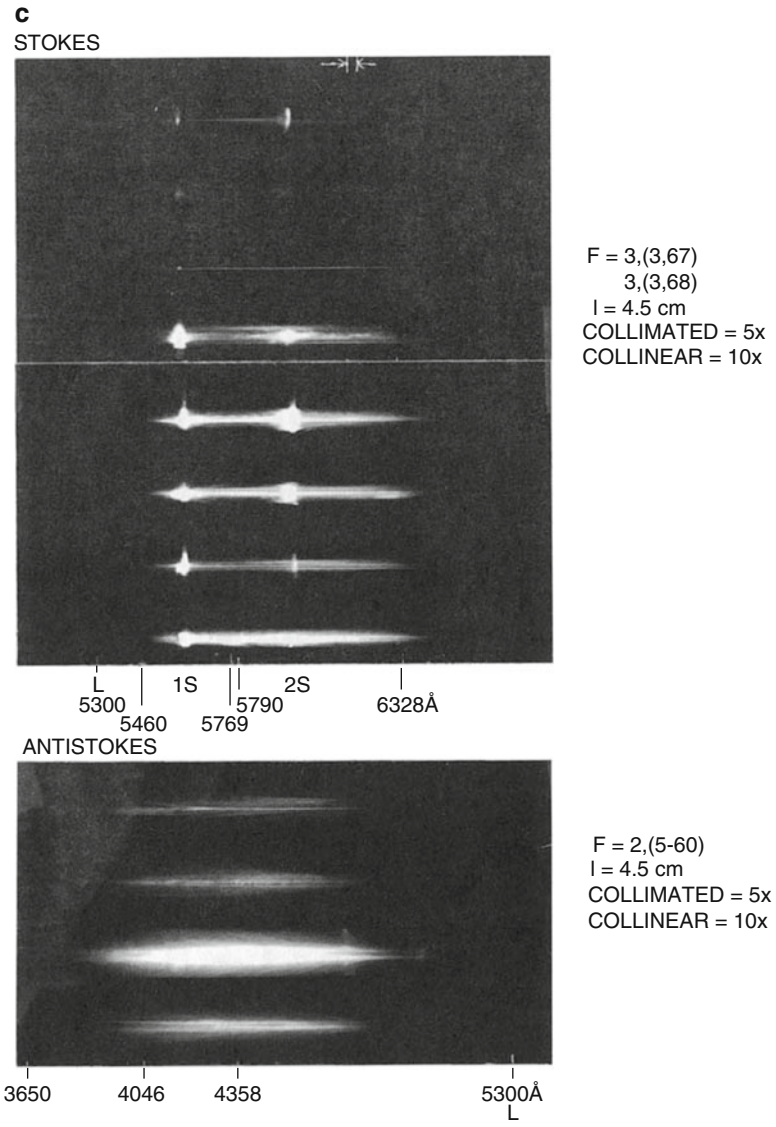

Fig. 2.4 (continued)

2.4.5 Supercontinuum in KBr

A high-power broadband coherent source in the near- and medium-infrared region can be realized by passing an intense 1.06-μm picosecond pulse through a **KBr** crystal. Figure 2.5 shows the spectra from 10-cm-long **KBr** crystal with excitation

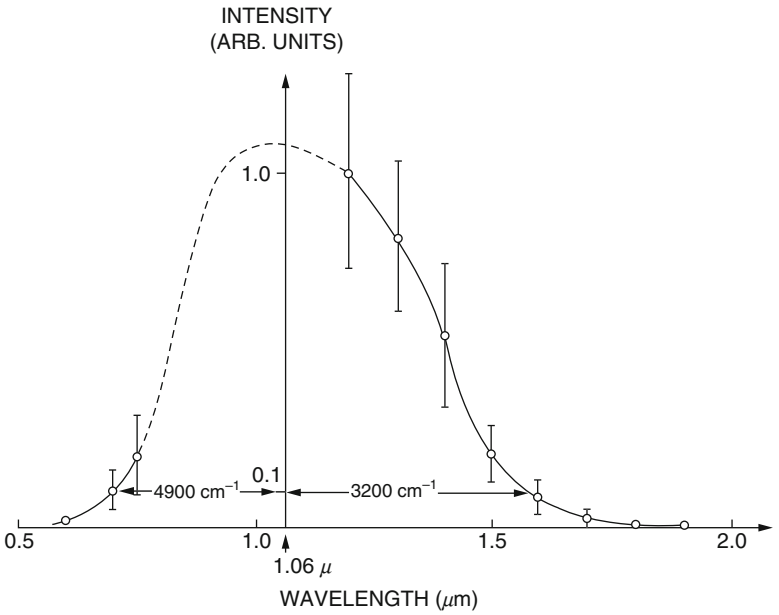

Fig. 2.5 Relative emission intensity versus emission wavelength for **KBr**. Exciting wavelength = 1.06 μm. (From Yu et al., 1975)

of a 9-ps, 10^{11} W/cm^2 pulse at 1.06 μm. On the Stokes side, the maximum intensity occurs at 1.2 μm. When the signal drops to 10^{-1}, the span of the spectral broadening is $\Delta\nu_s = 3200$ cm^{-1} on the Stokes side and $\Delta\nu_a = 4900$ cm^{-1} on the anti-Stokes side. Beyond 1.6 mm, the signal level falls off rapidly. At 1.8 μm, the signal is 10^{-2}, and at 2 mm, no detectable signal can be observed (Yu et al., 1975).

2.4.6 Supercontinuum in Semiconductors

Infrared supercontinuum spanning the range 3–14 μm can be obtained when an intense picosecond pulse generated from a CO_2 laser is passed into GaAs, AgBr, ZnSe, and CdS crystals (Corkum et al., 1985).

The supercontinuum spectra measured from a 6-cm-long Cr-doped GaAs crystal and a 3.8-cm AgBr crystal for different laser pulse durations and intensities and plotted in Figs. 1.6 and 1.7, respectively. The signals were normalized for the input laser energy and the spectral sensitivity of filters, grating, and detectors. Each point represents the average of three shots. The salient feature of the curves displayed in Figs. 2.6 and 2.7 is that the spectral broadening spans the wavelength region from 3 to 14 μm. The wave number spread on the anti-Stokes side is much greater than that on the Stokes side. From data displayed in Fig. 2.6, the maximum

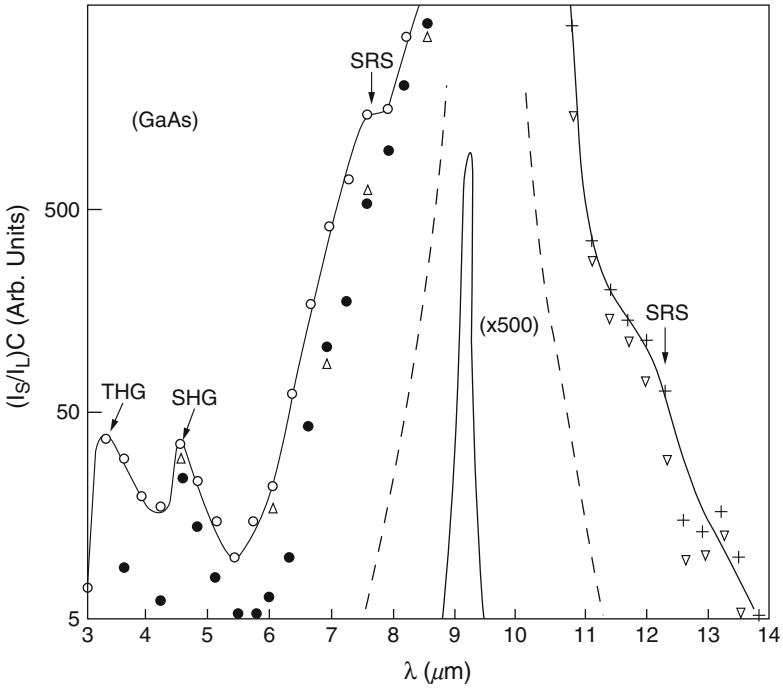

Fig. 2.6 Supercontinuum spectra from a 6-cm-long Cr-doped GaAs crystal. (From Corkum et al., 1985)

anti-Stokes spectral broadening is $\Delta\omega_a = 793\ \text{cm}^{-1}$. Including second and third harmonic generation (**SHG** and **THG**), it spans 2000 cm^{-1}. On the Stokes side, $\Delta\omega_s = 360\ \text{cm}^{-1}$, yielding a value of $\delta\omega_a/\delta\omega_s \sim 2.2$. For AgBr, Fig. 2.7 shows that $\Delta\omega_a = 743\ \text{cm}^{-1}$ and $\Delta\omega_s = 242\ \text{cm}^{-1}$, yielding $\Delta\omega_a/\Delta\omega_s \sim 3$.

The spectral broadening mechanism for the supercontinuum can originate from several nonlinear optical processes. These include self-phase modulation, the four-wave parametric effect, higher-order harmonic generation, and stimulated Raman scattering. In Fig. 2.6, the supercontinuum from the GaAs has two small peaks at 4.5 and 3.3 μm. These arise from the SHG and THG, respectively. Small plateaus are located at 7.5 and 12 μm. These arise from the first-order anti-Stokes and Stokes-stimulated Raman scattering combined with **SPM** about these wavelengths. The **SPM** is attributed to an electronic mechanism.

Summarizing the important experimental aspects of the spectra in condensed matter, the spectra are characterized by very large spectral widths and a nonperiodic or random substructure. Occasionally, a periodic structure interference minimum and maximum are observed. The modulation frequencies range from a few cm^{-1} to hundreds of cm^{-1}, and some modulation progressively increases away from the central frequency. The Stokes and anti-Stokes spectra are approximately equal in intensity and roughly uniform. The extents on the Stokes and anti-Stokes sides are

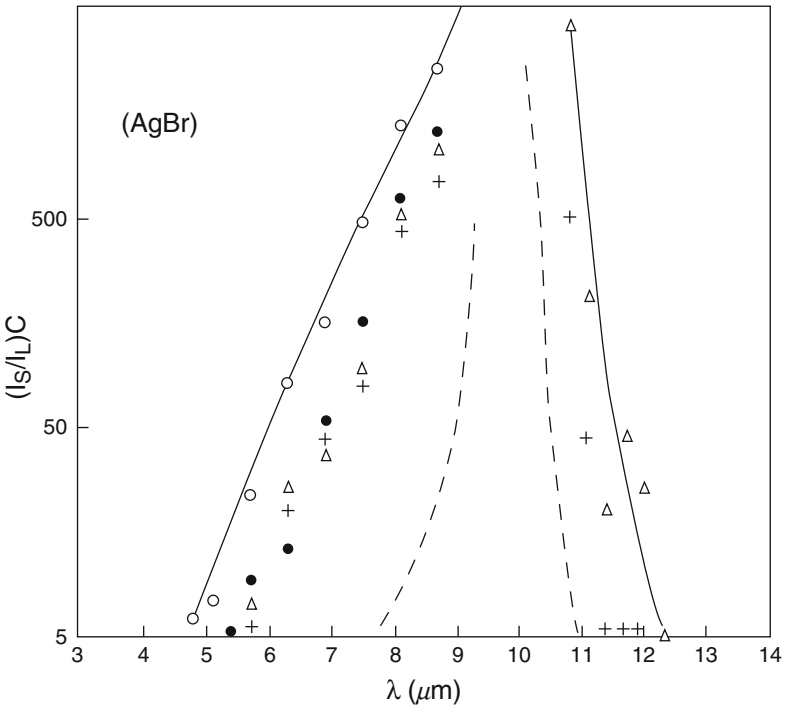

Fig. 2.7 Supercontinuum spectra from a 3.8-cm-long AgBr crystal. (From Corkum et al., 1985)

not symmetric. The peak intensity at the central frequency is 10^2–10^3 the intensity of the **SPM** spectra at a given frequency.

2.5 Generation of Supercontinuum in Liquids

Nonlinear optical effects in solids are very effective; however, damage generated in solid media often limits their usefulness for ultrashort high-power effects. Various kinds of inorganic and organic liquids are useful media for generating picosecond or femtosecond supercontinuum light pulses since they are self-healing media. The supercontinuum spectra produced in liquids (Alfano, 1972) are similar to the spectra displayed in Fig. 2.4 (Alfano, 1972). The following highlights the supercontinuum phenomena in the various favorite liquid media of the authors. These liquids give the most intense and uniform supercontinuum spectral distributions.

2.5.1 Supercontinuum in H_2O and D_2O

The supercontinuum generated in H_2O and D_2O by the second harmonic of a mode-locked neodymium glass laser spanned several thousand wave numbers. The time duration was equal to or less than the picosecond pulse that generated it (Busch et al., 1973). The continuum extended to below 310 nm on the anti-Stokes side and to the near-**IR** region on the Stokes side. There were sharp absorptions at 450 nm in the H_2O continuum and at 470 nm in the D_2O continuum resulting from the inverse Raman effect (Alfano & Shapiro, 1970b; Jones & Stoicheff, 1964). Focusing a 12-mJ, 1060-nm single pulse 14 ps in duration into 25 cm of liquid D_2O resulted in a continuum that showed practically no structure, extending from 380 to at least 800 nm and highly directional and polarized (Sharma et al., 1976). Enhancing the supercontinuum intensity using water with ions is discussed in Sect. 2.10.

2.5.2 Supercontinuum in CCl_4

Another favorite liquid for producing a supercontinuum is CCl_4, in which the spectra produced are similar to the spectra displayed in Fig. 2.4. A typical flat white supercontinuum extending from 430 nm through the visible and near infrared could be produced by focusing an 8-ps pulse at 1060 nm with about 15 mJ pulse energy into a cell containing CCl_4 (Magde & Windsor, 1974).

2.5.3 Supercontinuum in Phosphoric Acid

Orthophosphoric acid was found to be a useful medium for generating picosecond continuum light pulses ranging from the near UV to the near **IR**. By focusing a pulse train from a mode-locked ruby laser into a 10-cm-long cell containing phosphoric acid (60% by weight) solution in water by an 8-cm focal lens, a supercontinuum from near 450 nm to the near **IR** was obtained. The supercontinuum spectra contain structure arising from Raman lines (Kobayashi, 1979).

2.5.4 Supercontinuum in Polyphosphoric Acid

The supercontinuum from polyphosphoric acid was generated by focusing an optical pulse at 694.3 nm with 100 mJ pulse energy and a pulse width of 28 ps into a cell of any length from 2 to 20 cm containing polyphosphoric acid. It reaches 350 nm on the anti-Stokes side, being limited by the absorption of polyphosphoric acid,

and 925 nm on the Stokes side, being cut off by limitations of **IR** film sensitivity (Nakashima & Mataga, 1975).

2.6 Supercontinuum Generated in Optical Fibers

The peak power and the interaction length can be controlled better in optical fibers than in bulk materials. Optical fibers are particularly interesting material for nonlinear optical experiments. In this section, we discuss supercontinuum generation in glass optical fibers. Details of the use of **SPM** for pulse compression are discussed in other chapters.

The generation of continua in glass optical fibers was performed by Stolen et al. in 1974. Continua covering ~500 cm^{-1} were obtained. Shank et al. (1982) compressed 90-fs optical pulses to 30-fs pulses using **SPM** in an optical fiber followed by a grating compressor. Using the **SPM** in an optical fiber with a combination of prisms and diffraction gratings, they were able to compress 30 fs to 6 fs (Fork et al., 1987; also see Chap. 10 by Johnson and Shank).

A typical sequence of spectral broadening versus input peak power using 500-fs pulses (Baldeck et al., 1987b) is shown in Fig. 2.8. The spectra show **SPM** characteristic of heavy modulation. The spectral extent is plotted against the energy in Fig. 2.9 for 500-fs pulses (Baldeck et al., 1987b). The relative energy of each pulse was calculated by integrating its total broadened spectral distribution. The supercontinuum extent increased linearly with the pulse intensity. The fiber length dependence of the spectral broadening is plotted in Fig. 2.10. The broadening was found to be independent of the length of the optical fiber for $l > 10$ cm. This is due to group velocity dispersion. The **SPM** spectral broadening occurs in the first few centimeters of the fiber for such short pulses (Baldeck et al., 1987b).

In multimode optical fibers, the mode dispersion is dominant and causes pulse distortion. Neglecting the detailed transverse distribution of each mode, the light field can be expressed by

$$E(t) = \sum_i a_i A_i(t) \exp\left[i\omega_0 t - ik_i z\right], \tag{2.23}$$

where ω_0 is the incident laser frequency; a_i, $A_i(t)$, and $k = n_i\,\omega_0/c$ are the effective amplitude, electric field envelope function at the local time $\tau = t - z/v_{gi}$, and wave number of mode *i*, respectively; and v_{gi} is the group velocity of mode *i*. The effective refractive index of mode *i* is denoted by n_i and

$$n_i = n_{0i} + n_{2i}|E(t)|^2, \tag{2.24}$$

where n_{0i} and n_{2i} are the linear refractive index and the nonlinear coefficient of the *i*th mode, respectively. The nonlinearities of different modes are assumed to be the

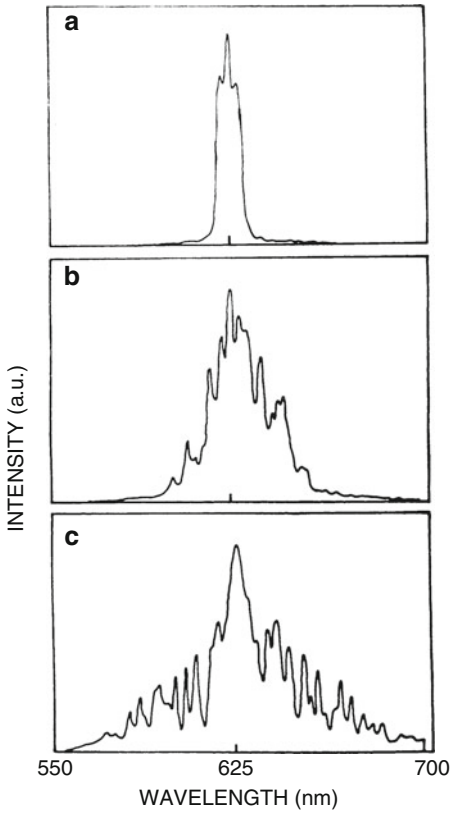

Fig. 2.8 Sequence of spectral broadening versus increasing input energy in a single-mode optical fiber (length = 30 cm). The intensity of the 500-fs pulse was increased from (**a**) to (**c**). (From Baldeck et al., 1987b)

same, that is, $n_{2i} = n_2$. Substituting Eq. (2.21) into Eq. (2.20), we obtain

$$E(t) = \sum a_i A_i(t) \exp\left[i\omega_0 t - i n_{0i}\omega_0 z/c - i\Delta\phi(t)\right], \tag{2.25}$$

where

$$\Delta\phi(t) = (n_2\omega_0 z/c)\,|E(t)|^2. \tag{2.26}$$

After inserting Eq. (2.23) into Eq. (2.26), the time-dependent phase factor $\Delta\phi(t)$ can be expanded in terms of E_i (t):

$$\Delta\phi(t) = \sum_i \sum_j (n_2\omega_0 z/c)\, a_i a_j A_i(t) A_j(t) \exp\left[i\left(n_{0i} - n_{0j}\right)\omega_0 z/c\right]. \tag{2.27}$$

In the picosecond time envelope, the terms of $i \neq j$ oscillate rapidly. Their contributions to the time-dependent phase factor are washed out. The approximate

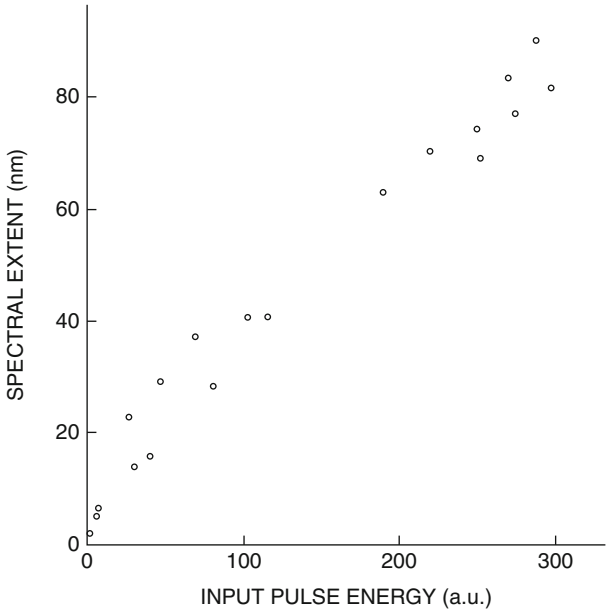

Fig. 2.9 Supercontinuum spectra versus input pulse energy in a single-mode optical fiber (length = 30 cm) for a 500-fs pulse. (From Baldeck et al., 1987b)

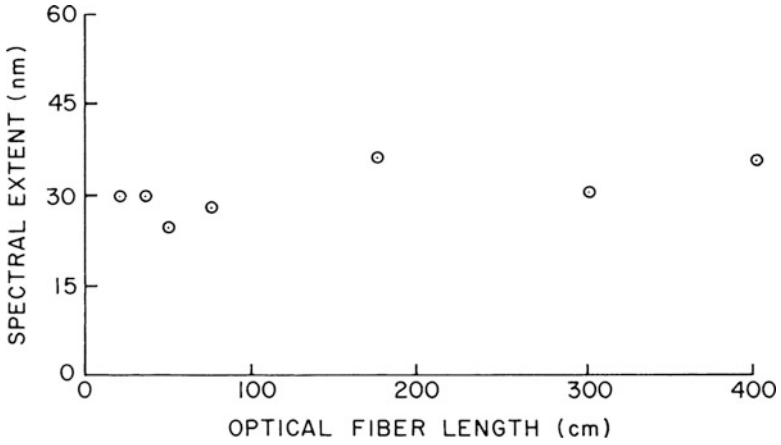

Fig. 2.10 Supercontinuum spectra versus optical fiber length for a 500-fs pulse. (From Baldeck et al., 1987b)

$\Delta\phi(t)$ has the form

$$\Delta\phi = \sum_i (n_2\omega_0 z/c)\, a_i^2 A_i^2(t). \tag{2.28}$$

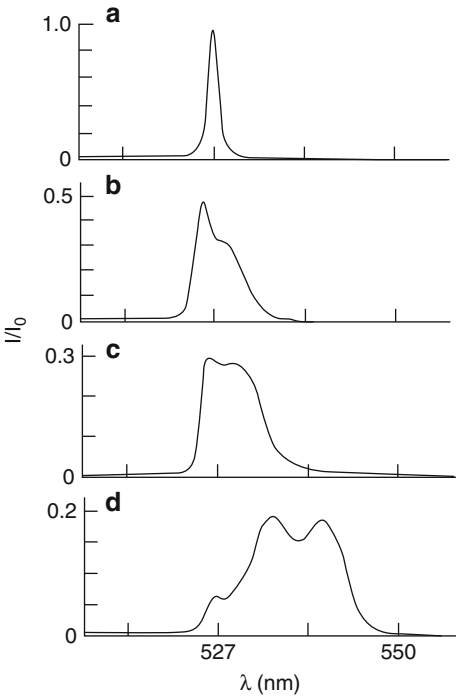

Fig. 2.11 Output spectra for 8-ps laser pulses at 527 nm propagating through different lengths of multimode optical fibers: (**a**) no fiber; (**b**) 22 cm; (**c**) 42 cm; (**d**) 84 cm. (From Wang et al., 1989)

The pulse shape changes due to the different group velocities of various modes. When most of the incident energy is coupled into the lower modes, the pulse will have a fast rising edge and a slow decay tail since the group velocity is faster for lower-order mode. This feature was observed using a streak camera. Therefore, the $\Delta\phi(t, z)$ of Eq. (2.28) will also have a fast rising edge and a slow decay tail. The time derivative of the phase $\Delta\phi(t, z)$ yields an asymmetric frequency broadening.

Figure 2.11 shows the spectral continuum generated from multimode glass optical fibers using 8-ps pulses at 530 nm. The spectral broadening is asymmetric about the incident laser frequency. It is shifted much more to the Stokes side than to the anti-Stokes side. The observed spectra did not show a modulation. This can be explained by the spectral resolution of the measurement system. The calculated modulation period is about 0.13 nm, which is much smaller than the resolution of the measurement system (about 1 nm) (Wang et al., 1989).

2.7 Supercontinuum Generation in Rare-Gas Liquids and Solids

Continuum generation is a general phenomenon that occurs in all states of matter. A system for testing the role of the electronic mechanism is rare-gas liquids and solids

(Alfano & Shapiro, 1970a). Rare-gas liquids are composed of atoms possessing spherical symmetry. Thus, there are no orientational, librational, or electron-lattice contributions to the nonlinear refractive index n_2. However, interrupted rocking of argon can occur in which a distorted atom can rock about an equilibrium value before it collides with other atoms. Contributions to the nonlinear refractive index might be expected from electrostriction, molecular redistribution, interrupted rocking, and a distortion of the electron clouds:

$$n_2 = n_{2\text{ELECTRONIC}} + n_{2\text{MR}} + n_{2\text{LIBRATION}} + n_{2\text{ELECTROSTR}}. \tag{2.29}$$

Electrostriction is ruled out because picosecond exciting pulses are too short. Molecular redistribution arises from fluctuations in the local positional arrangement of molecules and can contribute significantly to n_2. However, n_2 due to all mechanisms except electronic was estimated to be ~2×10^{-14} esu for liquid argon from depolarized inelastic-scattering data. Electronic distortion ($n_2 = 6 \times 10^{-14}$ esu) slightly dominates all nonlinear index contributions (Alfano & Shapiro, 1970a; Alfano, 1972). Furthermore, the depolarized inelastic light-scattering wing vanishes in solid xenon, implying that the molecular redistribution contribution to n_2 vanishes in rare-gas solids. Observations of self-focusing and SPM in rare-gas solids appear to provide a direct proof that atomic electronic shells are distorted from their spherical symmetry under the action of the applied field. However, both pure electronic and molecular redistribution mechanisms contribute to n_2 in rare-gas liquids. The response time of the system for a combination of both of these mechanisms lies between 10^{-15} and 10^{-12} s. For femtosecond and subpicosecond pulses, the dominant mechanism for n_2 and SPM is electronic in origin.

The experimental setup used to generate and detect a supercontinuum in rare-gas liquids and solids is the same as that shown in Fig. 2.3 with the exception that the samples are placed in an optical dewar.

Typical supercontinuum spectra from rare-gas liquids and solids are displayed in Fig. 2.12. Sweeps of 1000–6000 cm^{-1} were observed to both the Stokes and anti-Stokes sides of 530 nm in liquid argon. Modulation ranges from a few cm^{-1} to hundreds of cm^{-1}. Similar spectral sweeps were observed in liquid and solid krypton.

A most important point is that the threshold for observing SPM in liquid krypton is 0.64 ± 0.12 that in liquid argon. The SPM threshold ratio of solid and liquid krypton is 0.86 ± 0.15. In liquid argon, SPM spectra appear at a threshold power of ~0.5 GW focused in a 12-cm sample. The swept light is also collimated, polarized, and modulated. These observations rule out dielectric breakdown.

The refractive index in rare-gas liquids is given by $n_{||} = n_0 + n_2\langle E^2\rangle$, where $n_{||}$ is the refractive index parallel to the field. $\langle E^2\rangle^{1/2}$ is the rms value of the electric field. The electronic nonlinear refractive index in rare-gas liquids is given by

$$n_2 = \left[\left(n_0^2 + 2\right)^4 / 81 n_0\right] \pi N \rho, \tag{2.30}$$

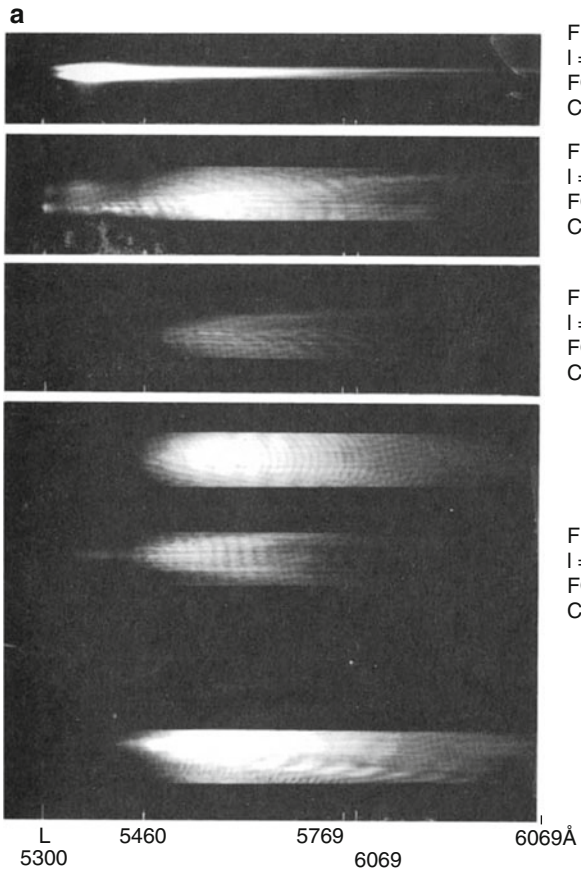

Fig. 2.12 Supercontinuum spectra for picosecond laser pulses at 530 nm passing through rare-gas liquids and solids; (**a**) Stokes SPM from liquid argon for different laser shots; (**b**) anti-Stokes SPM for liquid argon for different laser shots; (**c**) Stokes SPM for liquid and solid krypton for different laser shots. (From Alfano, 1972)

where n_0 is the linear refractive index, ρ is the second-order hyperpolarizability, and N is the number of atoms per unit volume. The term $n_2 = 0.6 \times 10^{-13}$ esu in liquid argon and $\simeq 1.36 \times 10^{-13}$ in liquid krypton. For liquid argon and liquid and solid krypton, the refractive indices are taken as 1.23, 1.30, and 1.35, respectively (McTague et al., 1969). Intense electric fields distort atoms and produce a birefringence. The anisotropy in refractive index between light traveling with the wave vector parallel and perpendicular to the applied electric field is given by (Alfano, 1972)

$$\delta n_{||} - \delta n_{\perp} = \frac{1}{3} n_2 E_0^2, \tag{2.31}$$

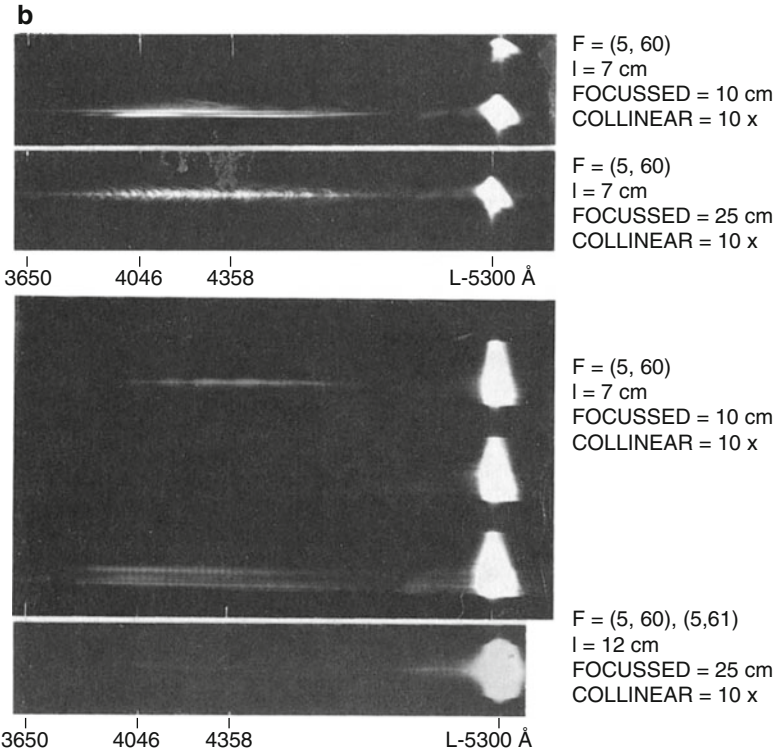

Fig. 2.12 (continued)

where $\delta n_{||}$ and $\delta n_{\perp}$ are the changes in refractive indices parallel and perpendicular to the field. The value of $n_2 E_0^2$ is ~5 × 10^{-5}V/m in liquid argon when E_0~1.5 × 10^7V/m (~4 × 10^{11}W/cm^2). This change in index explains the self-focusing and SPM described above which was observed by Alfano and Shapiro in 1970. Similar SPM effects occur in organic and inorganic liquids, often accompanied by SRS and inverse Raman effects.

2.8 Supercontinuum Generation in Antiferromagnetic $KNiF_3$ Crystals

The influence of magnetic processes on nonlinear optical effects is an interesting topic. In this section, we discuss the supercontinuum generation associated with the onset of magnetic order in a $KNiF_3$ crystal (Alfano et al., 1976). Light at 530 nm is well suited for the excitation pulse because $KNiF_3$ exhibits a broad minimum in its absorption (Knox et al., 1963) between 480 and 610 nm.

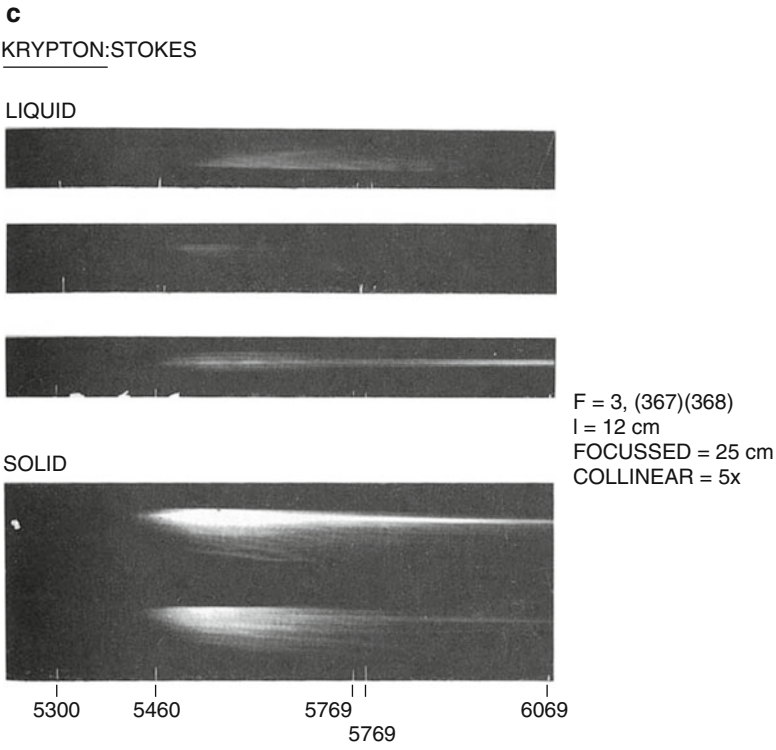

Fig. 2.12 (continued)

Typical spectra from an unoriented 5-cm-long $KNiF_3$ single crystal are displayed in Fig. 2.13 for 530-nm picosecond excitation (Alfano et al., 1976). The spectra are characterized by extensive spectral broadening ranging up to ~3000 cm^{-1} to either side of the laser frequency. The intensity, although not the spectral broadening, of the output exhibited the large temperature dependence illustrated in Fig. 2.14. There is no sharp feature at 552 nm, the position expected for stimulated Raman scattering by the 746-cm^{-1} magnon pair excitation. Usually, the spectra were smooth; however, occasionally structure was observed. A periodic structure with a modulation frequency of tens to hundreds of wave numbers was evident. The frequency broadening light is also polarized in the same direction as the incident 530-nm pulse. This property is the same observed in glass, crystals, and liquids (see Sects. 2.3, 2.4, 2.5, and 2.6). Self-focusing was also observed, usually in the form of 10 to 40 small self-focused spots 5–20 μm in diameter at the exit face of the crystal. Using a focused beam, optical damage could also be produced. It should be emphasized that spectral broadening was always observed even in the absence of self-focusing, damage, or periodic spectral intensity modulation.

Figure 2.15 shows the output intensity at 570 nm as a function of input intensity for two temperatures: above and below the Néel temperature. The output intensity

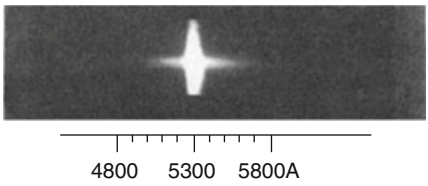

Fig. 2.13 Spectra for picosecond laser pulse at 530 nm passing through 5-cm-long $KNiF_3$. (From Alfano et al., 1976)

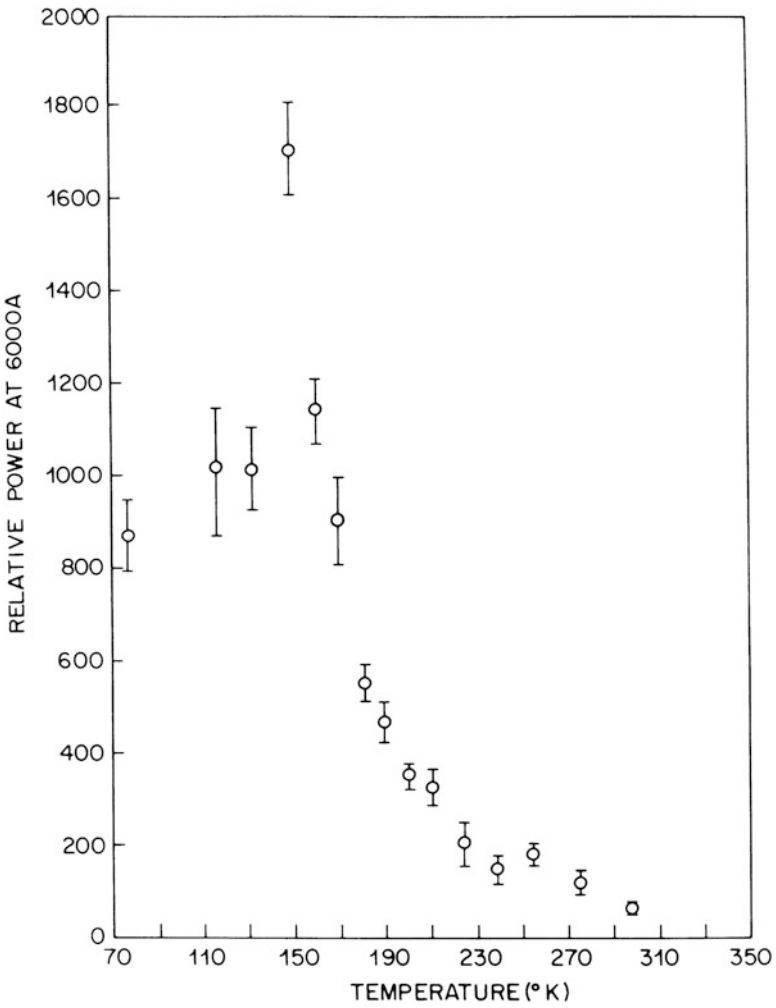

Fig. 2.14 Intensity of the frequency-broadening emission from $KNiF_3$ as a function of temperature at fixed pump intensity at 552 nm. (From Alfano et al., 1976)

is approximately exponential in the input intensity at both temperatures. However, the slope is more than a factor of two larger at 77 K than at 300 K. The rapid rise

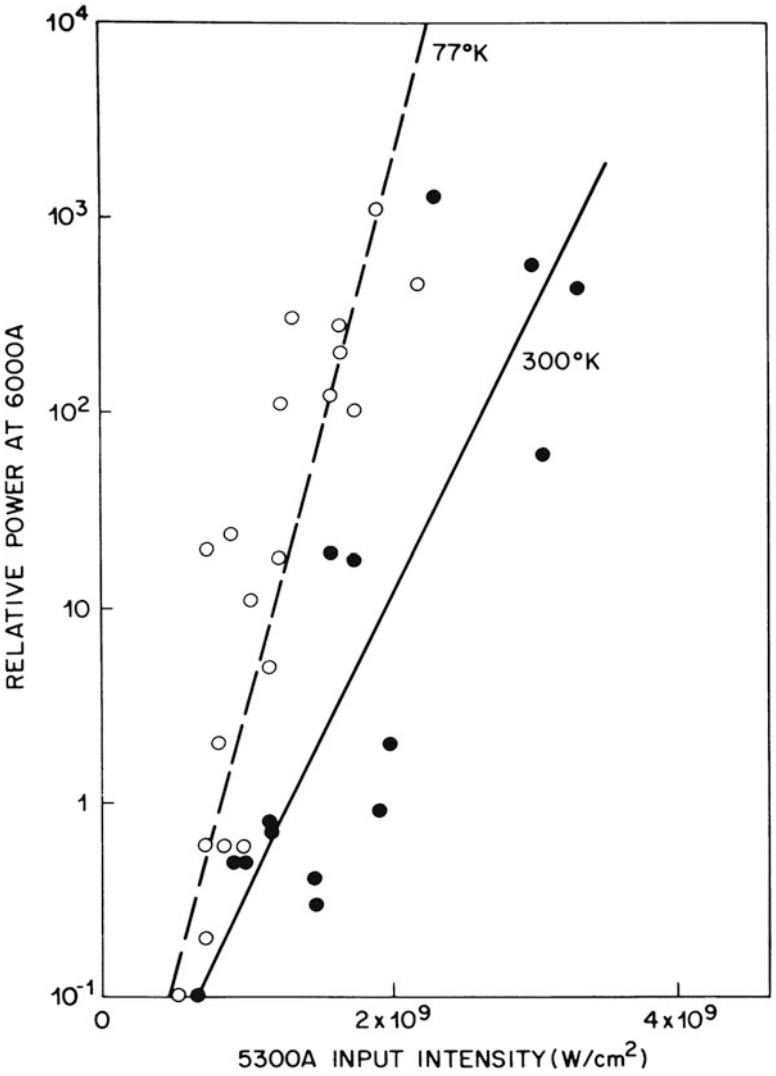

Fig. 2.15 Intensity dependence of continuum spectra at 570 nm from $KNiF_3$ as a function of pumping laser intensity at fixed lattice temperature

in conversion efficiency of four orders of magnitude within a small interval of input intensity is indicative of an amplification process with very large gain. Identical curves were obtained at 551 and 600 nm output wavelengths. The similarity in results for several output frequencies shows that simple stimulated magnon pair scattering is not the dominant process. If it were, one would expect the behavior at 552 nm to differ considerably from that at other wavelengths.

The most novel experimental results in $KNiF_3$ are the large (~20×) intensity increases below T_N. Spectra at 552, 570, and 600 nm behave identically – within experimental error – consistent with the observations in Fig. 2.15. The temperature dependence of the relative **peak** intensity for the spontaneous magnon pair scattering in the $KNiF_3$ sample (using 514.5 nm laser light) was measured and is potted in Fig. 2.14. For $KNiF_3$, the magnon pair scattering accounts for the entire inelastic light scattering and therefore for the non-σ electronic contribution to χ^3 (Hellwarth et al., 1975). The temperature dependence is compelling evidence for the magnetic origin of the low-temperature-enhanced nonlinear optical spectral broadened intensity.

The observation can be semiquantitatively accounted for in terms of a temperature-dependent spin contribution to the overall nonlinear susceptibility $\chi_{ijkl}^{(3)}$ that governs four-photon parametric mixing as the primary process. In general, $\chi^{(3)}$ may be written as a sum of electronic and Raman contributions (Levenson & Bloembergen, 1974). For $KNiF_3$, we may consider the latter to consist solely of the magnon pair Raman scattering contribution (Chinn et al., 1971; Fleury et al., 1975), which we can approximate as a Lorentzian:

$$\chi_{ijkl}^{(3)}(-\omega_3, \omega_1, \omega_1, -\omega_2) = \chi_E^{(3)} + K\frac{\alpha_{ij}^m \alpha_{kl}^m + \alpha_{il}^m \alpha_{jk}^m}{\omega_m - (\omega_1 - \omega_2) + i\Gamma_m}. \tag{2.32}$$

Here, ω_m and Γ_m denote the temperature-dependent frequency and linewidth, respectively, of the magnon pair excitations, a_{ij}^m is the magnon pair polarizability, and $\chi_E^{(3)}$ is the usual nonresonant, temperature-independent "electronic" contribution from nonlinear distortion of the electronic orbits. The second term in Eq. (2.32) is called magnetic $\chi_M^{(3)}$. Since the **integrated intensity** of the spontaneous magnon pair Raman spectrum, which is ~ $|\alpha^m|^2$, has been measured and found to be essentially temperature independent (Chinn et al., 1971; Fleury et al., 1975), the only quantities in Eq. (2.32) that vary significantly with temperature are ω_m and Γ_m. The observed temperature independence of the extent of spectral broadening, $\delta\omega$, may be explained by noting that $\delta\omega \sim 2\Delta\omega n_2 k E_1^2 l$ due to self-phase modulation. Here, $\Delta\omega$ is the spectral width of the input pulse, k is its propagation constant, E_1 is the field amplitude, and l is the path length. n_2 is the nonlinear refractive index, which contains a purely electronic contribution, σ, and a contribution proportional to the integrated Raman scattering cross section (Hellwarth et al., 1975). Since neither σ nor $|\alpha^m|^2$ is temperature dependent in $KNiF_3$, n_2, and therefore, $\Delta\omega$ should not vary either, in agreement with observations.

The observed strong temperature dependence of the intensity of the frequency-broadened spectrum (see Fig. 2.14) arises from the resonant term in Eq. (2.32) through the primary process $2\omega_1 \rightarrow \omega_2 + \omega_3$, which is strongest when $\omega_2 = \omega_1 + \omega_m$ and increases as Γ_m decreases (on cooling below the Néel temperature). That is, the resonant contribution to $\chi^{(3)}$ in Eq. (2.31) varies with temperature in the same way as the peak spontaneous magnon pair cross section: $\Gamma_m^{-1}(T)$. However, the individual contribution to $\chi^{(3)}$ cannot be directly

inferred from the dependence of the broadened spectrum. This is because the latter receives significant contributions from secondary processes of the form $\omega_1 + \omega'_2 \rightarrow \omega'_3 + \omega_4$, etc., in which products of the primary process interact with the pump to smooth the spectral distribution and wash out the sharp features that the resonant spin nonlinearity produces in the primary process. The large values of pump intensity and source spectral width make possible strong amplification in spite of imprecise phase matching in the forward direction. Such behavior (washing out of stimulated Raman features by the spectral broadening process) has frequently been observed in both liquids and crystals. Thus, a full quantitative description of the nonlinear optical processes in $KNiF_3$ is not yet possible.

2.9 Generation of Supercontinuum Near Electronic Resonances in Crystals

Since the active medium of a laser possesses well-defined electronic energy levels, knowledge of SPM near electronic levels is of paramount importance. SPM near electronic levels of a PrF_3 crystal have been investigated experimentally and theoretically to gain additional information on the SPM process – in particular, on the role played by the electronic levels and on how the continuum spectrum evolves through and beyond the electronic absorption levels (Alfano et al., 1974).

Experimentally, the Stokes and anti-Stokes spectrum and filament formation from the PrF_3 crystal are investigated under intense picosecond pulse excitation at the wavelength of 530 nm. The c axis of the crystal is oriented along the optical axis. The intensity distribution at the exit face of the crystal is magnified by 10× and imaged on the slit of a Jarrell-Ash $\frac{1}{2}$-m-grating spectrograph so that the spectrum of each filament can be displayed. The spectra are recorded on Polaroid type 57 film. No visible damage occurred in the PrF_3 crystal.

The PrF_3 crystal was chosen for the experiment because its electronic levels are suitably located on the Stokes and anti-Stokes sides of the 530-nm excitation wavelength. The absorption spectra of a – $\frac{1}{2}$-mm-thick PrF_3 crystal and the energy level scheme of Pr^{3+} ions are shown in Fig. 2.16. The fluorides of Pr have the structure of the naturally occurring mineral tysonite with D^4_{34} symmetry.

Typical spectra of frequency broadening from PrF_3 about 530 nm are shown in Fig. 2.17 for different laser shots. Because of the absorption associated with the electronic level, it is necessary to display the spectrum over different wavelength ranges at different intensity levels. In this manner, the development of the SPM spectrum through the electronic absorption levels can be investigated. Using appropriate filters, different spectral ranges are studied and displayed in the following figures: in Fig. 2.18a, the Stokes side for frequency broadening $\overline{v}_B > 100\ \text{cm}^{-1}$ at an intensity level (I_{SPM}) of ~10^{-2} of the laser intensity (I_L), in Fig. 2.18b, the Stokes side for $\overline{v}_B > 1500\ \text{cm}^{-1}$ at $I_{\text{SPM}} \sim 10^{-4}\ I_L$, in Fig. 2.18c, the anti-Stokes side for $\overline{v}_B > 100\ \text{cm}^{-1}$ at $I_{\text{SPM}} \sim 10^{-2}\ I_L$, and in Fig. 2.18d, the anti-Stokes side

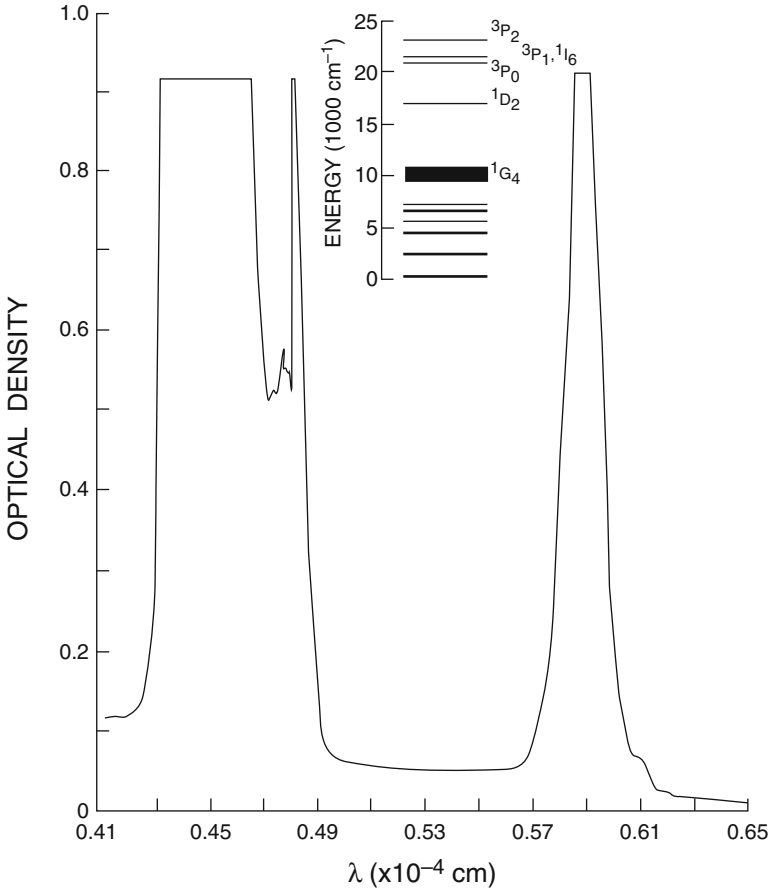

Fig. 2.16 Absorption spectra of 0.5-mm-thick PrF_3 crystal; insert is the level scheme of Pr^{3+} ions. (From Alfano et al., 1974)

for $\overline{\upsilon}_B > 1500\ \text{cm}^{-1}$ at $I_{\text{SPM}} \sim 10^{-4}\ I_L$. Usually, 50–100 small-scale filaments 5–50 μm in diameter are observed.

Several salient features are evident in the spectra displayed in Figs. 2.17 and 2.18. In Fig. 2.17, the Stokes and anti-Stokes spectra are approximately equal in intensity and frequency extent. The peak intensity at the central frequency is ~100 times the intensity of the SPM at a given frequency. The extent of the frequency broadening is ~1500 cm^{-1}, ending approximately at the absorption lines. Occasionally, a periodic structure of minima and maxima is observed that ranges from a few cm^{-1} to 100 cm^{-1}, and for some observations, no modulation is observed. Occasionally, an absorption band appears on the anti-Stokes side of the 530-nm line whose displacement is 430 cm^{-1}. In Fig. 2.18, the main feature is the presence of a much weaker superbroadband continuum whose frequency extends through and

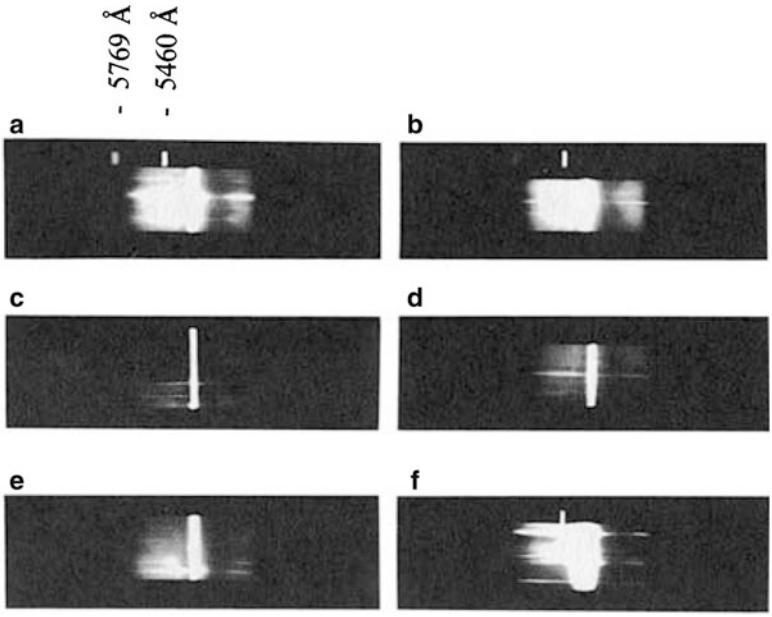

Fig. 2.17 Spectra from PrF_3 excited by 4-ps laser pulses at 530 nm; neutral density (ND) filters: (**a**) ND = 1.5; (**b**) ND = 1.5; (**c**) ND = 2.0; (**d**) ND = 2.0; (**e**) ND = 1.7; (**f**) ND = 1.4. A wire is positioned after the collection lens at the focal length. (From Alfano et al., 1974)

past the well-defined absorption lines of the Pr^{3+} ion to a maximum frequency of >3000 cm^{-1} on the Stokes side (end of film sensitivity) and >6000 cm^{-1} on the anti-Stokes side. The intensity of the continuum at a given frequency outside absorption lines is ~10^{-4} the laser intensity.

The observed absorption lines on the anti-Stokes side of 530 nm are located at 441.5, 465.3, and 484.5 nm and on the Stokes side at 593 and 610.9 nm. These lines correspond within ±0.7 nm to the absorption lines measured with a Cary 14. The absorption lines measured from the Cary spectra are ~3 cm^{-1} at 611.2 nm, 62 cm^{-1} at 5938.8 nm, 46 cm^{-1} at 485.2 nm, and >100 cm^{-1} at 441.2 nm. Figure 2.19 compares the Stokes absorption spectra of a PrF_3 crystal photographed with a $\frac{1}{2}$-m Jarrell-Ash spectrograph with different broadband light sources. Figure 2.19a was obtained with light emitted from a tungsten lamp passing through a $\frac{1}{2}$-mm PrF_3 crystal, Fig. 2.19b was obtained with the Stokes side of the broadband picosecond continuum generated in BK-7 glass passing through a $\frac{1}{2}$-mm PrF_3, and Fig. 2.19c was obtained with the broadband light generated in a 5-cm PrF_3 crystal. Notice that the absorption line at 611.1 nm is very pronounced in the spectra obtained with the continuum generated in PrF_3, whereas with conventional absorption techniques, it is barely visible. The anti-Stokes spectrum obtained with light emitted from a tungsten filament lamp passing through a $\frac{1}{2}$-mm PrF_3 crystal is shown in Fig. 2.20a. This is

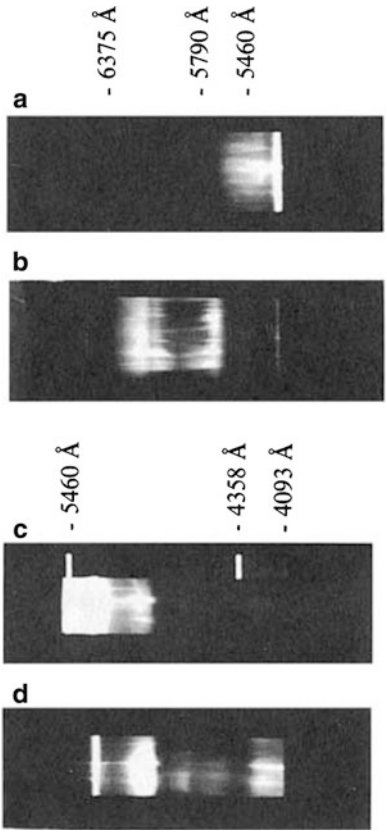

Fig. 2.18 Spectra on the Stokes and anti-Stokes sides of the 530-nm excitation: (**a**) Stokes side, Corning 3–68 filter, wire inserted, ND = 2.0; (**b**) Stokes side, Corning 3–66 filter, wire inserted; (**c**) anti-Stokes side, wire inserted, ND = 1.0; (**d**) anti-Stokes side, Corning 5–61, wire inserted. (From Alfano et al., 1974)

compared with the spectrum obtained with broadband light generated in a 5-cm PrF_3 crystal shown in Fig. 2.20b.

The angular variation of the anti-Stokes and Stokes spectral emission from PrF_3 is displayed in Fig. 2.21. The light emitted from the sample is focused on the slit of a $\frac{1}{2}$-m Jarrell-Ash spectrograph with a 5-cm focal length lens with the laser beam positioned near the bottom of the slit so that only the upper half of the angular spectrum curve is displayed. In this fashion, a larger angular variation of the spectrum is displayed. Emission angles >9° go off slit and are not displayed. This spectrum is similar to four-photon emission patterns observed from glass and liquids under picosecond excitation.

The experimental results show that a discontinuity in intensity occurs when the self-phase modulation frequency extends beyond the absorption line frequency. This is due to almost total suppression of the signal beyond the absorption resonance (Alfano et al., 1974). A similar argument and conclusion hold for the blue side of the laser line. The residual weak intensity that exists beyond the absorption line is not due to SPM. It can arise, however, from three-wave mixing. Since there was a continuum of frequencies created by SPM, it might be possible for three such

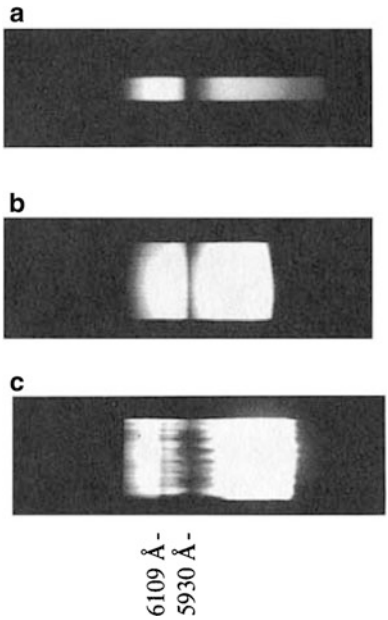

Fig. 2.19 Comparison of the Stokes absorption spectra of PrF_3 photographed with different light sources: (**a**) light emitted from a tungsten lamp is passed through 0.5-cm-thick crystal; (**b**) SPM light emitted from BK-7 glass is passed through 0.5-mm-thick crystal; (**c**) SPM light is generated within the 5-cm PrF_3. (From Alfano et al., 1974)

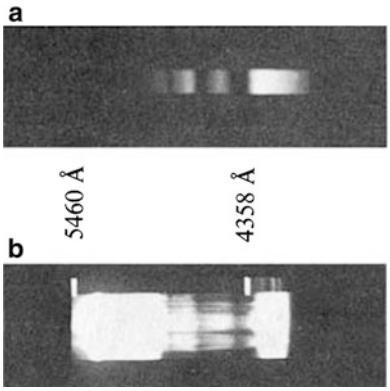

Fig. 2.20 Comparison of the anti-Stokes absorption spectrum of PrF_3 photographed with (**a**) light emitted from a tungsten lamp passing through 0.5-mm-thick crystal and (**b**) SPM light generated within the 5-cm PrF_3. (From Alfano et al., 1974)

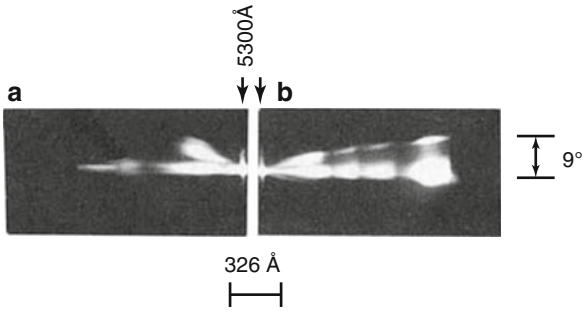

Fig. 2.21 Angular variation of the (**a**) Stokes and (**b**) anti-Stokes spectral patterns emitted from PrF3 crystal: (**a**) Corning 4 (3–67) filters, ND = 1.0; (**b**) Corning 2 (5–60) filters. (From Alfano et al., 1974)

frequencies, ω_1, ω_2, and ω_3, to mix to create a signal at frequency $\omega_1 + \omega_2 - \omega_3$ that lies beyond the absorption line. Since the frequencies are chosen from a continuum, it is also possible for phase matching to be achieved. For the spectrum in the domain between the laser frequency and the absorption line, the extent of self-broadening is proportional to the intensity. Since the energy in the pulse is proportional to the product of the frequency extent and the intensity spectrum, the intensity spectrum remains approximately constant. The observed absorption band in the continuum on the anti-Stokes side about 400 cm^{-1} away from the excitation frequency (see Fig. 2.17) is probably due to the inverse Raman effect (Jones & Stoicheff, 1964). The observed absorption band is located in the vicinity of strong Raman bands: 401, 370, and 311 cm^{-1}.

A curious feature of the associated weak broadband spectrum is the existence of a pronounced absorption line at a position (611.2 nm) where the linear absorption would be expected to be rather weak. A possible explanation for this is as follows: Imagine tracing the spatial development of the phase modulation spectrum. At a short distance, where the bounds of the spectrum have not yet intersected a strong absorption line, the spectrum is reasonably flat. On intersecting the absorption line, the spectrum abruptly drops (Alfano et al., 1974). The mechanism of FFPG is presumably responsible for the appearance of the signal beyond the absorption line limit. This explanation is also supported by the appearance of the angular emission pattern (see Fig. 2.21). As the spectrum continues to develop, one reaches a point where the limit of the regenerated spectrum crosses a weak absorption line. One can again expect a drastic drop in the spectrum at the position of this line. At still greater distances, renewed four-photon parametric regeneration accounts for the feeble signal. A continuum is generated behind absorption bands due to contributions from SPM, three-wave mixing (TWM), and FFPG.

2.10 Enhancement of Supercontinuum in Water by Addition of Ions

The most common liquids used to generate a continuum for various applications are CCl_4, H_2O, and D_2O. In most applications of the ultrafast supercontinuum, it is necessary to increase the conversion efficiency of laser excitation energy to the supercontinuum. One method for accomplishing this is based on the induced- or cross-phase modulation. Another way is to increase n_2 in materials. In this section, chemical means are used to obtain a tenfold enhancement of the ultrafast supercontinuum in water by adding Zn^{2+} or K^+ ions (Jimbo et al., 1987) for 8-ps pulse generation.

The optical Kerr gate (OKG) (Ho & Alfano, 1979) was used to measure the nonlinear refractive index of the salt solutions. The primary and second harmonic light beams were separated by a dichroic mirror and then focused into a 1-cm-long sample cell filled with the same salt solutions that produced the ultrafast

supercontinuum pulse enhancements. The size of the nonlinear index of refraction, n_2, was determined from the transmission of the probe beam through the OKG.

Three different two-component salt solutions of various concentrations were tasted. The solutes were KCl, $ZnCl_2$, and K_2ZnCl_4. All measurements were performed at 20 ± 1 °C. Typical spectra of ultrafast supercontinuum pulses exhibited both SPM and FPPG features. The collinear profile arising from SPM has nearly the same spatial distribution as the incident 8-ps, 530-nm laser pulse. The two wings correspond to FPPG pulse propagation. The angle arises from the phase-matching condition of the generated wavelength emitted at different angles from the incident laser beam direction. FPPG spectra sometimes appear as multiple cones and sometimes show modulated features. SPM spectra also show modulated patterns. These features can be explained by multiple filaments.

Typical ultrafast supercontinuum pulse spectra on the Stokes side for different aqueous solutions and neat water, measured with the optical multichannel analyzer, are shown in Fig. 2.22. The salient features in Fig. 2.22 are a wideband SPM spectrum together with the stimulated Raman scattering of the OH stretching vibration around 645 nm. The addition of salts causes the SRS signal to shift toward the longer-wavelength region and sometimes causes the SRS to be weak (Fig. 2.22a). The SRS signal of pure water and dilute solution appears in the hydrogen-bonded OH stretching region (~3400 cm^{-1}). In a high-concentration solution, it appears in the nonhydrogen-bonded OH stretching region (~3600 cm^{-1}). The latter features of SRS were observed in an aqueous solution of $NaClO_4$ by Walrafen (1972).

To evaluate quantitatively the effect of cations on ultrafast supercontinuum generation, the ultrafast supercontinuum signal intensity for various samples at a fixed wavelength was measured and compared. Figure 2.23 shows the dependence of the supercontinuum (mainly from the SPM contribution) signal intensity on salt concentration for aqueous solutions of K_2ZnCl_4, $ZnCl_2$, and KCl at 570 nm (Fig. 2.23a) and 500 nm (Fig. 2.23b). The data were normalized with respect to the average ultrafast supercontinuum signal intensity obtained from neat water. These data indicated that the supercontinuum pulse intensity was highly dependent on salt concentration and that both the Stokes and the anti-Stokes sides of the supercontinuum signals from a saturated K_2ZnCl_4 solution were about 10 times larger than from neat water. The insets in Fig. 2.23 are the same data plotted as a function of K^+ ion concentration for KCl and K_2ZnCl_4 aqueous solutions. Solutions of KCl and K_2ZnCl_4 generate almost the same amount of supercontinuum if the K^+ cation concentration is same, even though they contain different amounts of Cl^- anions. This indicates that the Cl^- anion has little effect on generation of the supercontinuum. The Zn^{2+} cations also enhanced the supercontinuum, though to a lesser extent than the K^+ cations.

The measurements of the optical Kerr effect and the ultrafast supercontinuum in salt-saturated aqueous solutions are summarized in Table 2.3. The measured n_2 (pure H_2O) is about 220 times smaller than n_2 (CS_2). The value $G_{SPM}(\lambda)$ represents the ratio of the SPM signal intensity from a particular salt solution to that from neat water at wavelength λ. G_{Kerr} is defined as the ratio of the transmitted intensity

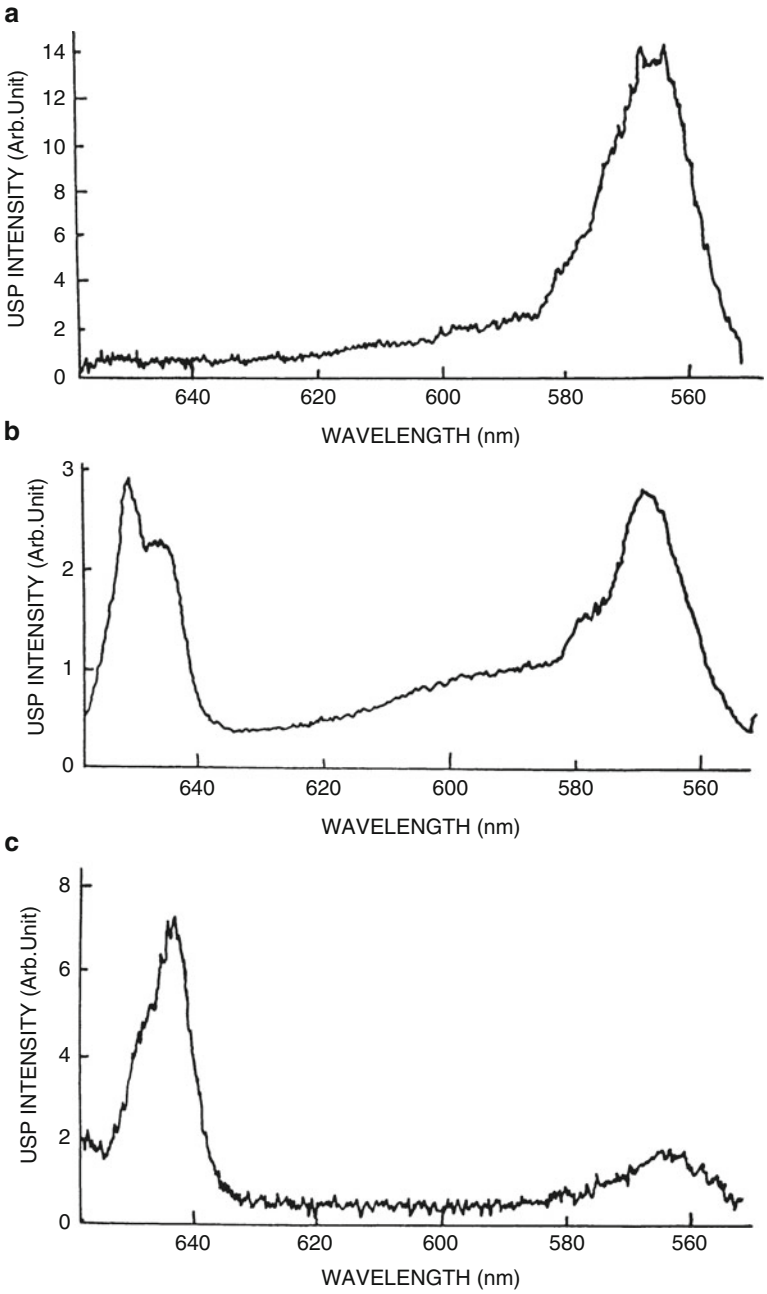

Fig. 2.22 SPM spectrum of (**a**) saturated K_2ZnCl_4 solution, (**b**) 0.6-m K_2ZnCl_4, and (**c**) pure water. The SRS signal (645 nm) is stronger in pure water, and it disappears in high-concentration solution. (From Jimbo et al., 1987)

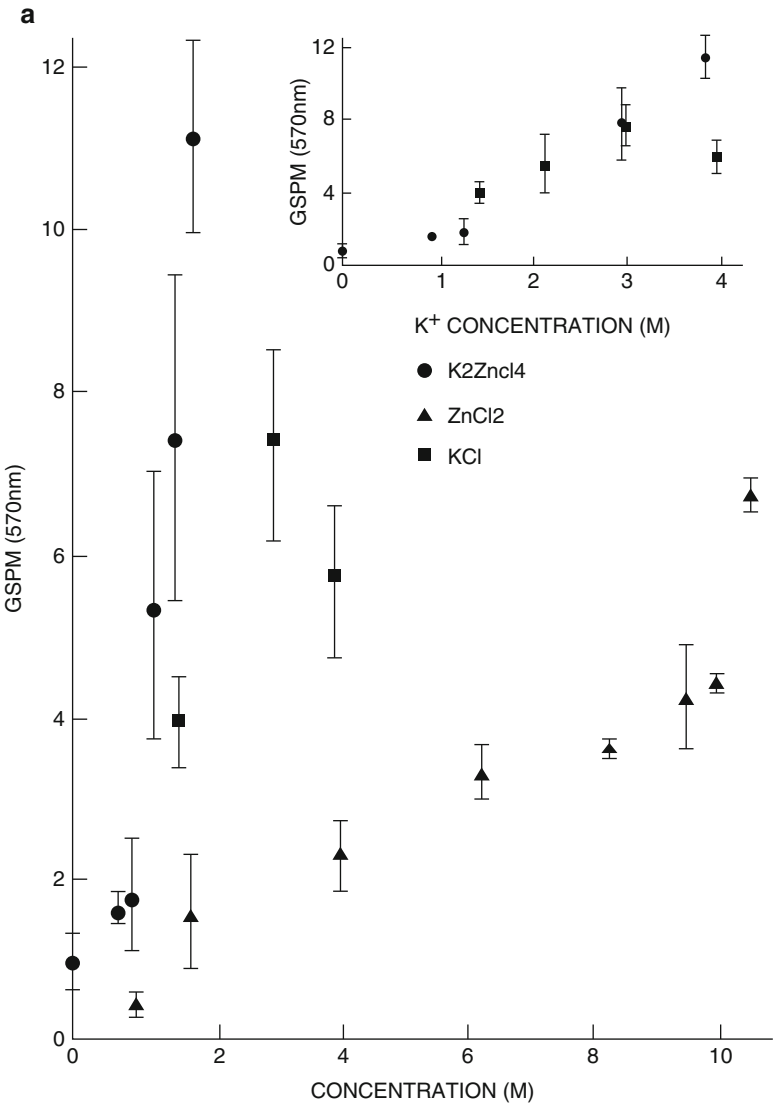

Fig. 2.23 Salt concentration dependence of the SPM signal (**a**) on the Stokes side and (**b**) on the anti-Stokes side 20 °C. Each data point is the average of about 10 laser shots. The inserts are the same data plotted as a function of K^+ ion concentration for KCl and K_2ZnCl_4 aqueous solutions. (From Jimbo et al., 1987)

caused by a polarization change of the probe beam in a particular salt solution to that in neat water; G_{Kerr} is equal to $[n_2 \text{ (particular solution)}/n_2 \text{ (water)})]^2$. Table 2.3 shows that, at saturation, K_2ZnCl_4 produced the greatest increase in the supercontinuum. Although $ZnCl_2$ generated the largest enhancement of the optical Kerr effect, it did

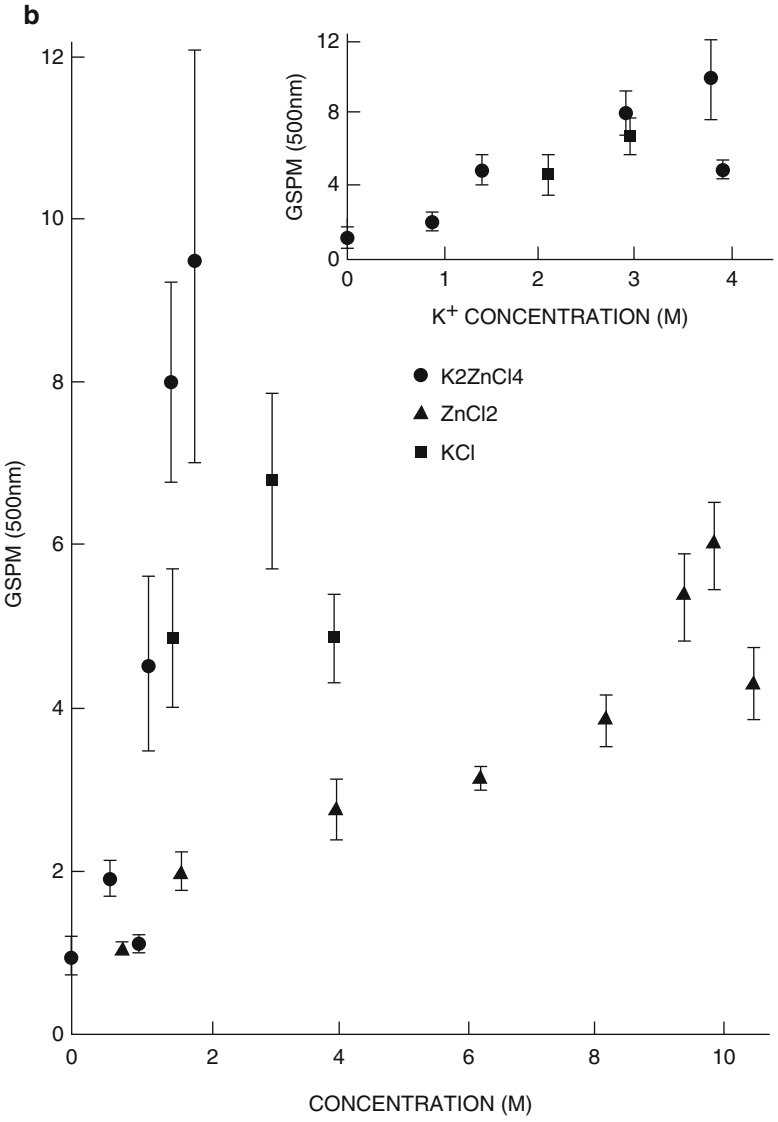

Fig. 2.23 (continued)

not play an important role in the enhancement of the ultrafast supercontinuum (a possible reason for this is discussed below). The optical Kerr effect signal from saturated solutions of $ZnCl_2$ was about 2–3 times greater than that from saturated solutions of K_2ZnCl_4.

The enhancement of the optical nonlinearity of water by the addition of cations can be explained by the cations' disruption of the tetrahedral hydrogen-bonded

Table 2.3 Enhancement of the supercontinuum and optical Kerr effects signals in saturated aqueous solutions at 20 °C[a]

Signal	K_2ZnCl_4 (1.9 M)	KCl (4.0 M)	$ZnCl_2$ (10.6 M)
$G_{SPM}(570)$	11 ± 1	5.6 ± 0.9	6.6 ± 0.4
$G_{SPM}(500)$	9.5 ± 2.5	4.9 ± 0.2	4.3 ± 0.5
G_{Kerr}	16 ± 1	6.1 ± 1.4	35 ± 9

[a] $G_{SPM}(\lambda) = [I_{SPM}(\lambda)/I_{laser}(530\ nm)]_{solution}/[I_{SPM}(\lambda)/I_{laser}(530\ nm)]_{water}$

water structures and their formation of hydrated units (Walrafen, 1972). Since the nonlinear index n_2 is proportional to the number density of molecules, hydration increases the number density of water molecules and thereby increases n_2. The ratio of the hydration numbers of Zn^{2+} and K^+ has been estimated from measurements of G_{Kerr} and compared with their values based on ionic mobility measurements. At the same concentration of KCl and $ZnCl_2$ aqueous solution, (G_{Kerr} generated by $ZnCl_2$ solution)/(G_{Kerr} generated by KCl solution) = $[N(Zn^{2+})/N(K^+)]^2 \sim 2.6$, where $N(Zn^{2+}) \sim 11.2 \pm 1.3$ and $N(K^+) \sim 7 \pm 1$ represent the hydration numbers for the Zn^{2+} and K^+ cations, respectively. The calculation of the hydration number of $N(Zn^{2+})/N(K^+) \sim 1.5$ is in good agreement with the Kerr nonlinearity measurements displayed in Table 2.3.

In addition, from our previous measurements and discussions of nonlinear processes in mixed binary liquids (Ho & Alfano, 1978), the total optical nonlinearity of a mixture modeled from a generalized Langevin equation was determined by the coupled interactions of solute–solute, solute–solvent, and solvent–solvent molecules. The high salt solution concentration may contribute additional optical nonlinearity to the water owing to the distortion from the salt ions and the salt-water molecular interactions.

The finding that Zn^{2+} cations increased G_{Kerr} more than G_{SPM} is consistent with the hydration picture. The transmitted signal of the OKG depends on Δn, while the ultrafast supercontinuum signal is determined by $\partial n/\partial t$. The ultrafast supercontinuum also depends on the response time of the hydrated units. Since the Zn^{2+} hydrated units are larger than those of K^+, the response time will be longer. These effects will be reduced for longer pulses. Two additional factors may contribute to part of the small discrepancy between G_{SPM} and G_{kerr} for $ZnCl_2$. The first one is related to the mechanism of δn generation in which χ_{1111} is involved in the generation of SPM while the difference $\chi_{1111} - \chi_{1112}$ is responsible for the optical Kerr effect. The second is the possible dispersion of n_2 because of the difference in wavelength between the exciting beams of the ultrafast supercontinuum and the optical Kerr effects.

The optical Ker effect is enhanced 35 time by using $ZnCl_2$ as a solute, and the ultrafast supercontinuum is enhanced about 10 times by using K_2ZnCl_4 as a solute. The enhancement of the optical nonlinearity has been attributed to an increase in the number density of water molecules owing to hydration and the coupled interactions of solute and solvent molecules. Addition of ions can be used to increase n_2 for SPM generation and gating.

2.11 Temporal Behavior of SPM

In addition to spectral features, the temporal properties of the supercontinuum light source are important for understanding the generation and compression processes. In this section, the local generation, propagation, and pulse duration reduction of SPM are discussed.

2.11.1 Temporal Distribution of SPM

In Sect. 2.1, using the stationary phase method, it was described theoretically that the Stokes and anti-Stokes frequencies should appear at well-defined locations in time within leading and trailing edges of the pump pulse profile (Alfano, 1972). Theoretical analyses by Stolen and Lin (1978) and Yang and Shen (1984) obtained similar conclusions.

Passing an 80-fs laser pulse through a 500-μm-thick ethylene glycol jet stream, the pulse duration of the spectrum in time was measured by the autocorrelation method (Fork et al., 1983). These results supported the SPM mechanism for supercontinuum generation. In the following, the measurements of the distribution of various wavelengths for the supercontinuum generated in CCl_4 by intense 8-ps laser pulses (Li et al., 1986) are presented. Reduction of the pulse duration using the SPM principle is discussed in Sect. 10.3.

The incident 530-nm laser pulse temporal profile is shown in Fig. 2.24. The pulse shape can be fitted with a Gaussian distribution with duration $\tau(\text{FWHM}) = 8$ ps. The spectral and temporal distributions of the supercontinuum pulse were obtained by measuring the time difference using a streak camera. The measured results are shown as circles in Fig. 2.25. Each data point corresponds to an average of about six laser shots. The observation is consistent with the SPM and group velocity dispersion. To determine the temporal distribution of the wavelengths generated within a supercontinuum, the group velocity dispersion effect (Topp & Orner, 1975) in CCl_4 was corrected. Results corrected for both the optical delay in the added filters and the group velocity are displayed as triangles in Fig. 2.25. The salient feature of Fig. 2.25 indicates that the Stokes wavelengths of the continuum lead the anti-Stokes wavelengths.

Using the stationary phase SPM method [Eqs. 2.6a and 2.6b], the generated instantaneous frequency ω of the supercontinuum can be expressed by

$$\omega(t) - \omega_L = -(\omega_L l/c)\,\partial(\Delta n)/\partial t, \tag{2.33}$$

where ω_L is the incident laser angular frequency, l is the length of the sample, and Δn is the induced nonlinear refractive index n_2E^2. A theoretical calculated curve for the sweep is displayed in Fig. 2.26 by choosing appropriate parameters to fit the experimental data of Fig. 2.25. An excellent fit using a stationary phase model

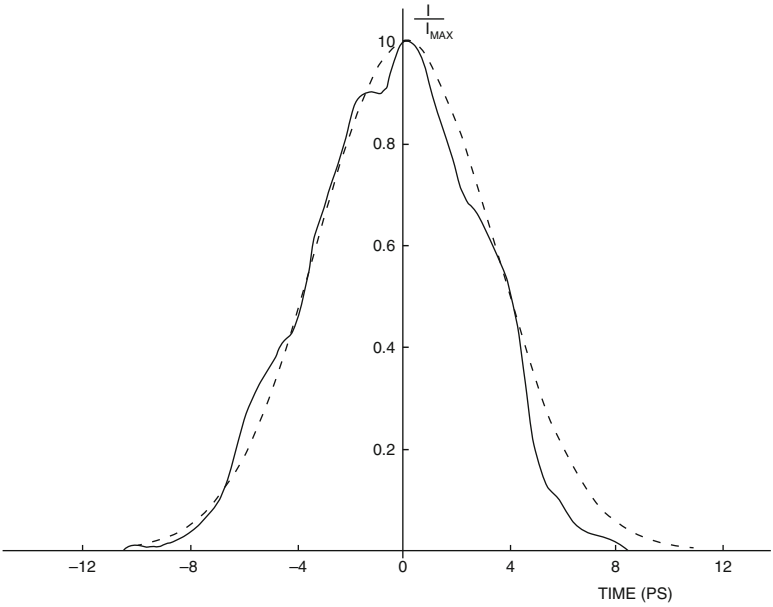

Fig. 2.24 Temporal profile of a 530-nm incident laser pulse measured by a 2-ps-resolution streak camera. The dashed line is a theoretical fit to an 8-ps EWHM Gaussian pulse. (From Li et al., 1986)

up to maximum sweep demonstrates that the generation mechanism of the temporal distribution of the supercontinuum arises from the SPM. During the SPM process, a wavelength occurs at a well-defined time within the pulse. The above analysis will be supported by the additional experimental evidence for SPM described in Sect. 10.3 (see Fig. 2.29).

2.11.2 Local Generation and Propagation

The dominant mechanisms responsible for the generation of the ultrafast supercontinuum as mentioned in Sects. 2.1 and 2.2 are SPM, FPPG, XPM, and SRS. In the SPM process, a newly generated wavelength could have bandwidth-limited duration at a well-defined time location (Alfano, 1972) in the pulse envelope. In the FPPG and SRS processes, the duration of the supercontinuum pulse could be shorter than the pump pulse duration due to the high gain about the peak of the pulse. In either case, the supercontinuum pulse will be shorter than the incident pulse at the local spatial point of generation. These pulses will be broadened in time due to the group velocity dispersion in condensed matter (Ho et al., 1987).

Typical data on the time delay of 10-nm-bandwith pulses centered at 530, 650, and 450 nm wavelengths of the supercontinuum generated from a 20-cm-long cell

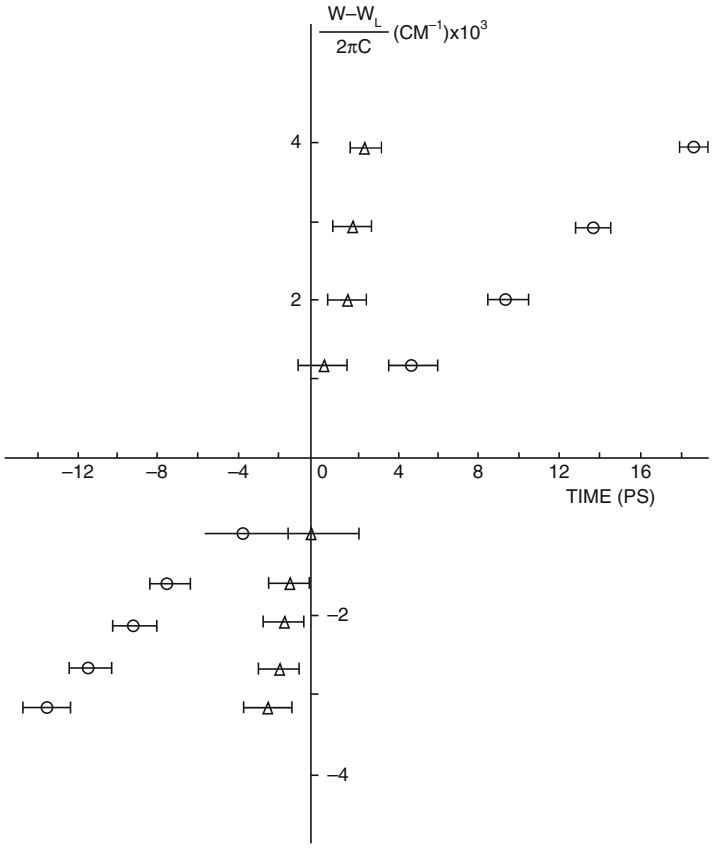

Fig. 2.25 Measured supercontinuum temporal distribution at different wavelengths: (o) data points with correction of the optical path in filters; (Δ) data points with correction of both the optical path in filters and group velocity dispersion in liquid. (From Li et al., 1986)

filled with CCl_4 are displayed in Fig. 2.27. The peak locations of 530, 650, and 450 nm are −49, −63, and −30 ps, respectively. The salient features in Fig. 2.27 (Ho et al., 1987) indicate that the duration of all 10-nm-band supercontinuum pulses is only 6 ps, which is shorter than the incident pulse of 8 ps, the Stokes side (650 nm) of the supercontinuum pulse travels ahead of the pumping 530 nm by 14 ps, and the anti-Stokes side (450 nm) of the supercontinuum pulse lags the 530 nm by 10 ps.

If the supercontinuum could be generated throughout the entire length of the sample, the Stokes side supercontinuum pulse generated by the 530-nm incident laser pulse at $z = 0$ cm of the sample would be ahead of the 530-nm incident pulse after propagating through the length of the sample. Over this path, 530 nm could continuously generate the supercontinuum pulse. Thus, the Stokes side supercontinuum generated at the end of the sample coincides in time with the 530-nm incident pulse. In this manner, a supercontinuum pulse centered at a particular

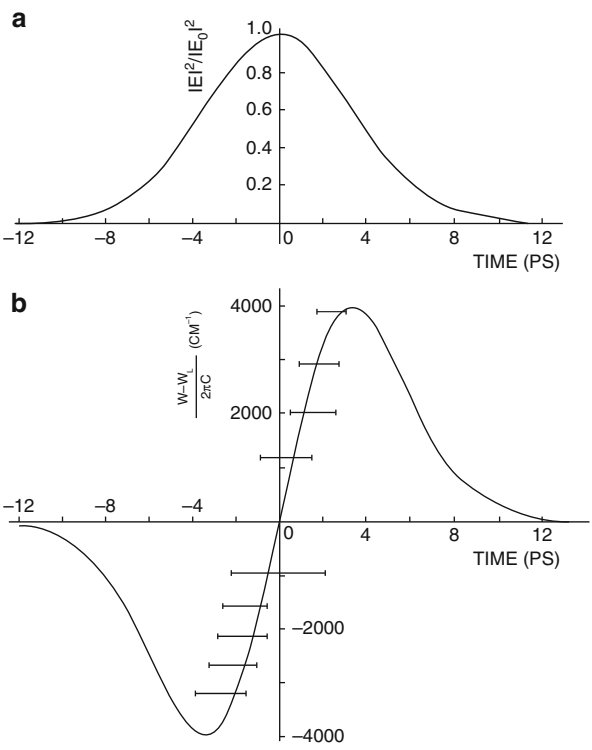

Fig. 2.26 Comparison of the measured temporal distribution of supercontinuum with the SPM model. (From Li et al., 1986)

Stokes frequency could have a pulse greater than the incident pulse extending in time from the energy of the 530-nm pulse to the position where the Stokes frequency was originally produced at $z \sim 0$ cm. From a similar consideration, the anti-Stokes side supercontinuum pulse would also be broadened. However, no slow asymmetric tail for the Stokes pulse or rise for the anti-Stokes pulse is displayed in Fig. 2.27. These observation suggest the local generation of supercontinuum pulses.

A model to describe the generation and propagation features of the supercontinuum pulse has been formulated based on local generation. The time delay of Stokes and anti-Stokes supercontinuum pulses relative to the 530-nm pump pulse is accounted for by the filaments formed ~5 cm from the sample cell entrance window. The 5-cm location is calculated from data in Fig. 2.27 by using the equation

$$T_{530} - T_{\text{supercon.}} = \Delta x \left(\frac{1}{v_{530}} - \frac{1}{v_{\text{supercon.}}} \right), \tag{2.34}$$

where Δx is the total length of supercontinuum pulse travel in CCl_4 after the generation. T_{350} and $T_{\text{supercon.}}$ are the 530-nm and supercontinuum pulse peak time locations in Fig. 2.27, and v_{530} and v_{supercon} are the group velocities of the 530-nm and supercontinuum pulses, respectively.

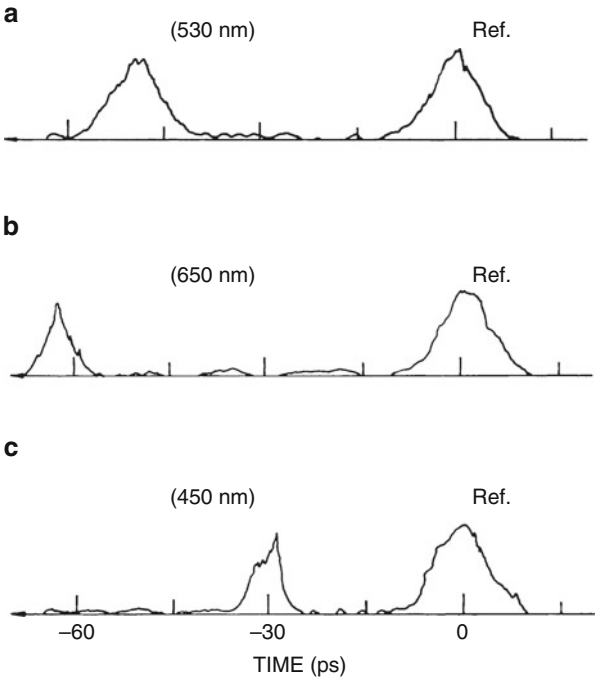

Fig. 2.27 Temporal profiles and pulse locations of a selected 10-nm band of a supercontinuum pulse at different wavelengths propagated through a 20-cm-long CCl4 cell: (**a**) $\lambda = 530$ nm; (**b**) $\lambda = 650$ nm; (**c**) $\lambda = 450$ nm. Filter effects were compensated. (From Ho et al., 1987)

The duration of the supercontinuum pulse right at the generation location is either limited by the bandwidth of the measurement from the SPM process or shortened by the parametric generation process. In either cases, a 10-nm-bandwidth supercontinuum pulse will have a shorter duration than the incident pulse. After being generated, each of these 10-nm-bandwidth supercontinuum pulses will travel through the rest of the sample and will continuously generated by the incident 530 nm over a certain interaction length before these two pulses walk off. The interaction length can be calculated as (Alfano, 1972)

$$l = \tau \frac{v_{530} v_{\text{supercon.}}}{v_{530} - v_{\text{supercon.}}}, \tag{2.35}$$

where l is the interaction length over the pump, and the supercontinuum pulses stay spatially coincident by less than the duration (FWHM) of the incident pump pulse, and τ is the duration of the supercontinuum pulse envelope. From Eq. (2.35), one can estimate the interaction length from the measured τ of the supercontinuum pulse. Using parameters $\tau = 6$ ps, $v_{530} = c/l.4868$, and $v_{\text{supercon.}} = c/l.4656$, the

interaction length $l = 8.45$ cm is calculated. This length agrees well with the measured beam waist length of 8 cm for the pump pulse in CCl4.

Since no long tails were observed from the supercontinuum pulses to the dispersion delay times of the Stokes and anti-Stokes supercontinuum pulses, the supercontinuum was not generated over the entire length of 20 cm but only over 1–9 cm. This length is equivalent to the beam waist length of the laser in CCl4. The length of the local SPM generation over a distance of 8.45 cm yields a possible explanation for the 6-ps supercontinuum pulse duration. In addition, a pulse broadening of 0.3 ps calculated from the group velocity dispersion of a 10-nm band at 650-nm supercontinuum traveling over 20 cm of liquid CCl4 is negligible in this case.

Therefore, the SPM pulses have shorter durations than the pump pulse and were generated over local spatial domains in the liquid cell.

2.11.3 SPM Pulse Duration Reduction

The principle behind the pulse narrowing based on the spectral temporal distribution of the SPM spectrally broadened in time within the pulse is described in Sects. 2.2 and 10.1. At each time t within the pulse, there is a frequency $\omega(t)$. When a pulse undergoes SPM, the changes in the optical carrier frequency within the temporal profile are greatest on the rising and falling edges, where the frequency is decreased and increased, respectively. Near the peak of the profile, and in the far leading and trailing wings, the carrier frequency structure is essentially unchanged. The maximum frequency shift is proportional to the intensity gradient on the sides of the pulse, and this determines the position of the outer lobes of the power spectrum. If these are then attenuated by a spectral window of suitably chosen width, the wings of the profile where the high- and low-frequency components are chiefly concentrated will be depressed, while the central peak will be largely unaffected. The overall effect is to create a pulse that is significantly narrower in time than the original pulse duration. A file can be used to select a narrow portion of the pulse, giving rise to a narrower pulse in time.

A threefold shortening of 80-ps pulses to 30 ps from an Nd:YAG laser broadened from 0.3 to 4 Å after propagation through 125 m of optical fiber with a monochromator as a spectral window was demonstrated using this technique (Gomes et al., 1986). The measurements of pulses at different wavelengths of the frequency sweep of supercontinuum pulses generated by 8-ps laser pulses propagating in CCl_4 show that the continuum pulses have a shorter duration (~6 ps) than the pumping pulses (Li et al., 1986).

A major advance occurred when a 25-ps laser pulse was focused into a 5-cm-long cell filled with D_2O. A continuum was produced. Using 10-nm-bandwidth narrowband filters, tunable pulses of less than 3 ps in the spectral range from 480 to 590 nm (Fig. 2.28) were produced (Dorsinville et al., 1987).

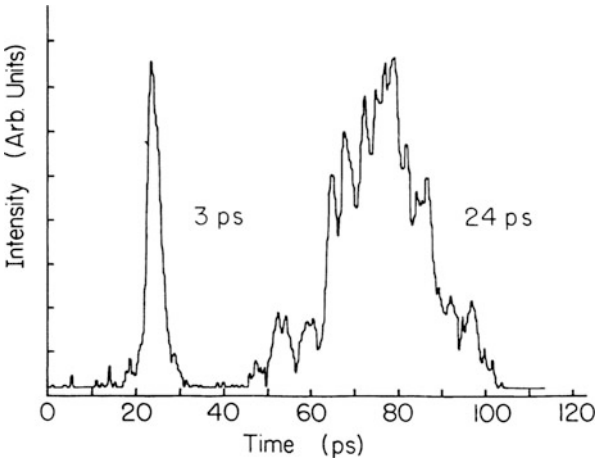

Fig. 2.28 Streak camera temporal profile of the 25-ps, 530-nm incident laser pulse and 10-nm-bandwidth pulse at 580 nm. The 3-ps pulse was obtained by spectral filtering a SPM frequency continuum generated in D_2O. (From Dorsinville et al., 1987)

To identify the SPM generation mechanism, the temporal distribution of the continuum spectrum was determined by measuring the time delay between the continuum and a reference beam at different wavelengths using a streak camera. The results are displayed in Fig. 2.29, which is similar to data displayed in Fig. 2.25. The time delay was ~22 ps for a 140-nm change in wavelength; as predicted by the SPM mechanism, the Stokes wavelength led the anti-Stokes wavelength (Alfano, 1972). The delay due to group velocity over a 5-cm D_2O cell for the 140-nm wavelength change is less than 3 ps.

The remaining 18 ps is well accounted for by the SPM mechanism using a 25-ps (FWHM) pulse and the stationary phase method (Alfano, 1972). Furthermore, a 10-nm selected region in the temporal distribution curve corresponds to an ~2.6-ps width matching the measured pulse duration (Fig. 2.28). This observation suggests that by using narrower bandwidth filters, the pulse duration can be shortened to the uncertainty limit.

2.12 Higher-Order Effects on Self-Phase Modulation

A complete description of SPM-generated spectral broadening should take into account higher-order effects such as self-focusing, group velocity dispersion, self-steepening, and initial pulse chirping. Some of these effects are described by Suydam (Chap. 6), Shen (Chap. 1), and Agrawal (Chap. 3). These effects will influence the observed spectral profiles.

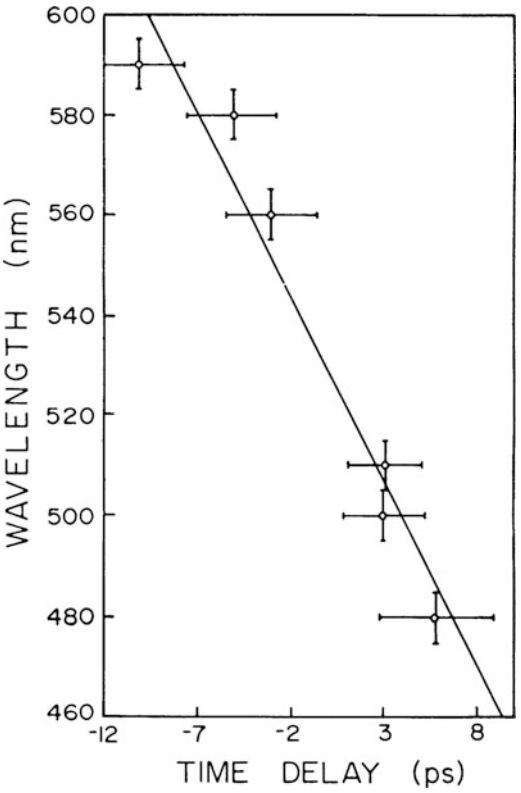

Fig. 2.29 Continuum temporal distribution at different wavelengths. Horizontal error bars correspond to 10-nm bandwidths of the filter. (From Dorsinville et al., 1987)

2.12.1 Self-Focusing

In the earliest experiments using picosecond pulses, the supercontinuum pulses were often generated in small-scale filaments resulting from the self-focusing of intense laser beams (Alfano, 1972). Self-focusing arises from the radial dependence of the nonlinear refractive index $n(r) = n_0 + n_2E^2(r)$ (Shen, 1984; Auston, 1977). It has been observed in many liquids, bulk materials (Shen, 1984), and optical fibers (Baldeck et al., 1987a). Its effects on the continuum pulse generation can be viewed as good and bad. On the one hand, it facilitates the spectral broadening by concentrating the laser beam energy. On the other hand, self-focusing is a random and unstable phenomenon that is not controllable. Femtosecond supercontinua are generated with thinner samples than picosecond supercontinua, so it can reduce but not totally eliminate self-focusing effects.

2.12.2 Dispersion

Group velocity dispersion (GVD) arises from the frequency dependence of the refractive index. These effects are described by Agrawal (Chap. 3). The first-order GVD term leads to a symmetric temporal broadening (Marcuse, 1980). A typical value for the broadening rate arising from $\partial^2 k/\partial\omega^2$ is 500 fs/m-nm (in silica at 532 nm). In the case of supercontinuum generation, spectral widths are generally large (several hundred nanometers), but interaction lengths are usually small (<1 cm). Therefore, the temporal broadening arising from GVD is often negligible for picosecond pulses but is important for femtosecond pulses. Limitations on the spectral extent of supercontinuum generation are also related to GVD. Although the spectral broadening should increase linearly with the medium length (i.e., $\Delta\omega(z)_{\max} = \omega_0\, n_2\, a^2\, z/c\, \Delta\tau$), it quickly reaches a maximum as shown in Fig. 2.10. This is because **GVD**, which is large for pulses having **SPM**-broadened spectra, reduces the pulse peak power a^2 and broadens the pulse duration $\Delta\tau$. As shown in Fig. 2.25, the linear chirp parameter is decreased by the **GVD** chirp in the normal dispersion regime. This effect is used to linearize chirp in the pulse compression technique.

The second-order term $\partial^3 k/\partial\omega^3$ has been found to be responsible for asymmetric distortion of temporal shapes and modulation of pulse propagation in the lower region of the optical fiber (Agrawal & Potasek, 1986). Since the spectra of supercontinuum pulses are exceptionally broad, this term should also lead to asymmetric distortions of temporal and spectral shapes of supercontinuum pulses generated in thick samples. These effects have been observed.

In multimode optical fibers, the mode dispersion dominates and causes distortion of the temporal shapes. This in turn yields asymmetric spectral broadening (Wang et al., 1989).

2.12.3 Self-Steepening

Pulse shapes and spectra of intense supercontinuum pulses have been found to be asymmetric (De Martini et al., 1967). There are two potential sources of asymmetric broadening in supercontinuum generation. The first one is the second-order **GVD** term. The second one is self-steepening, which is intrinsic to the **SPM** process and occurs even in nondispersion media. Details of the effects of self-steepening can be found in Suydam (Chap. 6), Shen and Yang (Chap. 1), and Manassah (Chap. 5).

Because of the intensity and time dependence of the refractive index, $n = n_0 + n_2 E(t)^2$, the supercontinuum pulse peak sees a higher refractive index than its edges. Because $v = c/n$, the pulse peak travels slower than the leading and trailing edges. This results in a sharpened trailing edge. Self-steepening occurs and more blue-shifted frequencies (sharp trailing edge) are generated than red frequencies. Several theoretical approaches have given approximate solutions for the electric

field envelope distorted by self-steepening and asymmetric spectral extent. Actual self-steepening effects have not been observed in the time domain.

2.12.4 Initial Pulse Chirping

Most femtosecond and picosecond pulses are generated with initial chirps. Chirps arise mainly from **GVD** and **SPM** in the laser cavity. As shown in Fig. 2.30, the spectral broadening is reduced for positive chirps and enhanced for negative chirps in the normal dispersion regime. The spectral distribution of SPM is also affected by the initial chirp.

2.13 High-Resolution Spectra of Self-Phase Modulation in Optical Fibers

In bulk materials, self-focusing plays an important role in the SPM process, and the spectral-broadening changes significantly from laser shot to shot. To obtain a stable, repeatable SPM spectrum, one would like to keep the cross section constant over the entire propagation distance in the medium. Optical fibers are ideal materials for this type of investigation because the beam cross section of a guided wave would be constant and the self-focusing effect can be neglected. The spectral features of SPM in optical fibers measured by a piezoelectrically scanned planar Fabry–Perot interferometer with the resolution of approximately one-third of the laser linewidth were pioneered by Stolen and Lin (1978), using a 180-ps laser pulse. Measurements performed on the fine structures of the SPM spectra of picosecond laser pulses by use of a grating spectrometer with a spectral resolution higher than one-tenth of the laser linewidth and comparing the spectral profiles with the results calculated by use of the SPM model are discussed in the following.

2.13.1 Reduced Wave Equation

The optical electromagnetic field of a propagating optical pulse must satisfy Maxwell's equations. From Maxwell's equations, one can obtain the wave equation that describes the amplitudes of light pulses propagating in optical fibers [See Eq. (A.19) in Appendix]:

$$\frac{\partial A}{\partial z} + \frac{1}{v_g}\frac{\partial A}{\partial t} + i\frac{1}{2}k^{(2)}\frac{\partial^2 A}{\partial t^2} = i\frac{\omega_0 n_2}{c}|A|^2 A, \tag{2.36}$$

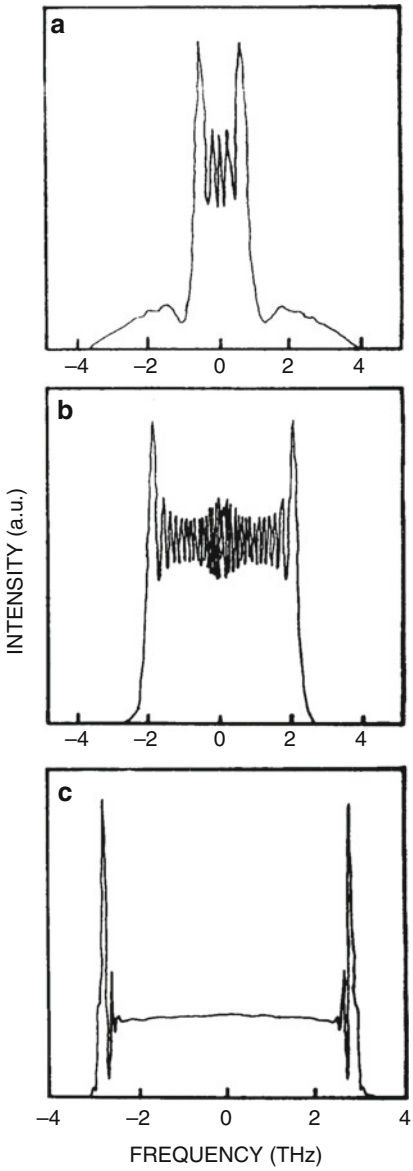

Fig. 2.30 Influence of initial pulse chirping on **SPM**-broadened spectra in optical fibers. Peak power = 1000 W. (**a**) $C = 50$; (**b**) $C = 0$; (**c**) $C = -50$ [see Eq. (2.17)]. (From Baldeck et al., 1987b)

The third term on the left-hand side of this equation is the dispersion term. The absorption of the optical fiber and the higher-order nonlinearities have been neglected in obtaining Eq. (2.36).

Changing the variables

$$\tau = t - \frac{z}{v_g}, \tag{2.37}$$

$$z = z' \tag{2.38}$$

and denoting by a and α the amplitude and the phase of the electric envelope, respectively, A can be expressed as

$$A(z, \tau) = a(z, \tau) \exp[i\alpha(z, \tau)], \tag{2.39}$$

where τ is the local time of the propagating optical pulse.

Because the fiber lengths used in the experiment are much smaller than the dispersion lengths, which can be calculated to be a few kilometers, the dispersion term in Eq. (2.36) can be neglected. Therefore, Eq. (2.36) further reduces to

$$\frac{\partial a}{\partial z} = 0 \tag{2.40}$$

$$\frac{\partial \alpha}{\partial z} = \frac{\omega_0 n_2}{c} a^2 \tag{2.41}$$

The analytical solutions for Eqs. (2.40) and (2.41) can be obtained as

$$a(\tau) = a_0 F(\tau) \tag{2.42}$$

$$\alpha(z, \tau) = \frac{\omega_0 n_2}{c} \int_0^z a^2(z', \tau)\, dz' = \frac{\omega_0 n_2}{c} {a_0}^2 F^2(\tau)\, z, \tag{2.43}$$

where a_0 is the amplitude, and $F(t)$ is the pulse envelope of the input optical pulse.

Because the pulse duration is much larger than the optical period $2\pi/\omega_0$, the electric field at each τ within the pulse has a specific local and instantaneous frequency that is given by

$$\omega(\tau) = \omega_0 + \delta\omega(\tau) \tag{2.44}$$

where

$$\delta\omega(\tau) = -\frac{\partial \alpha}{\partial \tau} = -\frac{\omega_0 n_2}{c} {a_0}^2 \frac{\partial F^2(\tau)}{\partial \tau} z \tag{2.45}$$

$\delta\omega(\tau)$ is the frequency shift generated at a particular local time τ within the pulse envelope. This frequency shift is proportional to the derivative of the pulse envelope with respect to τ, the nonlinear refractive index, and the intensity of the pulse.

It can be obtained by the complex-field spectral profiles $E(z, \omega - \omega_0)$ of the optical pulse affected by SPM by computing the Fourier transformation of its temporal pulse distribution as

$$\begin{aligned} E\,(z, \omega - \omega_0) &= \tfrac{1}{2\pi} \int A\,(z, \tau) \exp\left(-i\omega_0\tau\right) \exp\left(i\omega\tau\right) d\tau \\ &= \tfrac{1}{2\pi} \int a\,(z, \tau) \exp\left[\left(i\alpha\left(z, \tau\right)\right]\right] \exp\left[i\,(\omega - \omega_0)\,\tau\right] d\tau \end{aligned} \tag{2.46}$$

The spectral-intensity distribution of the pulse is given by

$$|E\,(z, \omega - \omega_0)|^2. \tag{2.47}$$

Figure 2.31 shows a set of numerical solutions of Eq. (2.47) for laser pulses at 532 nm. The initial pulse shape is Gaussian. The spectrum of the input laser is shown in Fig. 2.31a. The length of the optical fiber used in the calculation is 1 m. As the intensity of the input laser pulse increases, the spectrum of the output signal broadens. Large-intensity oscillations occur at the same time because of the interference. In the same spectrum, the width of the maxima near the input laser frequency is smaller than that farther away from the input laser frequency. The outmost maxima have the largest widths. The salient feature of SPM is the spectral broadening which is accompanied by oscillations structure. The structure in the spectra consists of many maximum peaks (Max) where the outermost peaks are more intense (Also see Agrawal, Chap. 3). These oscillations are caused by interference. The maximum phase $\theta_{\max}$ is given by number of maxima peaks in the SPM spectra by peaks:

$$\text{Phase}_{\text{Max}} = \theta_{\max} = (\text{Max} - 1/2)\,\pi. \tag{2.48}$$

For example, Fig. 2.31e has max phase = 9½π and Fig. 2.31f has max phase = 12½π.

For different spectra, the widths of the maxima at the same wavelength of the spectra of higher-intensity laser pulses are smaller than are those for the lower-intensity pulses. The peak intensities of the outermost maxima for all the different intensities remain the largest, as can be seen in Fig. 2.31b–f. The SPM phase change is $\theta = \omega n_2 I(t) z/c$. The peak of pulse gives rises to 1 radian after propagating a distance given by:

$$L_{\text{spm}} = c/\omega n_2 I_p \tag{2.49}$$

After traveling a distance given by 5π L_{spm}, the phase change at the peak will be 5π.

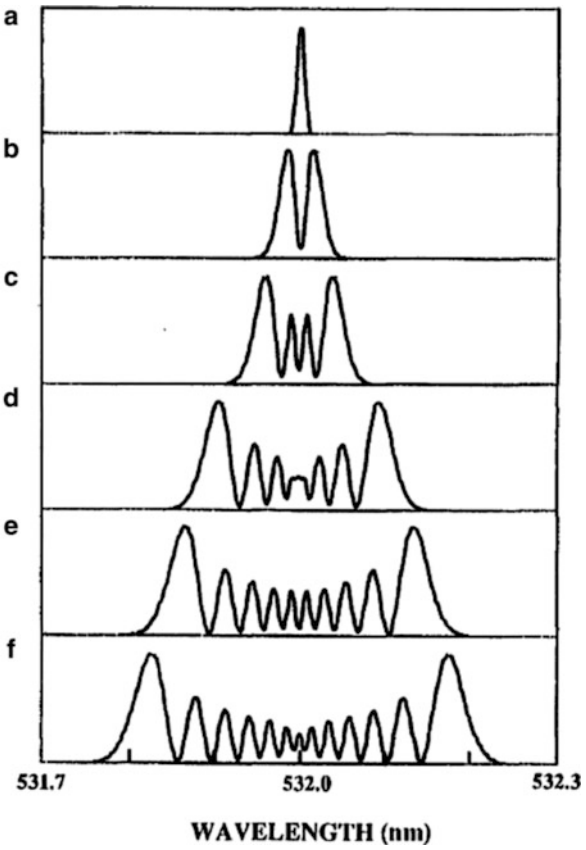

Fig. 2.31 Calculated SPM spectra of 532-nm laser pulses propagating in an optical fiber. The core diameter of the optical fiber was 2.5 μm. $n_2 = 3.2 \times 10^{-16}$ cm^2/W. (**a**) Input laser, (**b**) $P_0 = 110$ W, (**c**) $P_0 = 225$ W, (**d**) $P_0 = 460$ W, (**e**) $P_0 = 630$ W, Max = 10 and Max Phase = 9½π, (**f**) $Po = 790$ W, Max = 13 and Max Phase = 12½π. (From Wang et al., 1994a, b)

The numerical solutions of expression (2.47) for laser pulses at 1064 nm are displayed in Fig. 2.32. The results are similar to those displayed in Fig. 2.31 for laser pulses at 532 nm.

2.13.2 Experiment

The experimental arrangement used to measure high-resolution spectra of self-phase modulation in optical fibers is illustrated in Fig. 2.33. A 10-Hz mode-locked Quantel Nd:YAG laser system was used to generate laser pulses at 1064 nm and pulses at 532 nm. The 1/*e* pulse durations were 39 and 28 ps, respectively, and the pulse energies were approximately 2 μJ and 200 nJ for 1064 and 532 nm, respectively. A set of color filters was used to select the wavelengths of the laser pulses. The laser pulses were coupled into a 1-m optical fiber with a 20× microscope objective lens. A set of neutral-density filters was used in front of the microscope objective lens

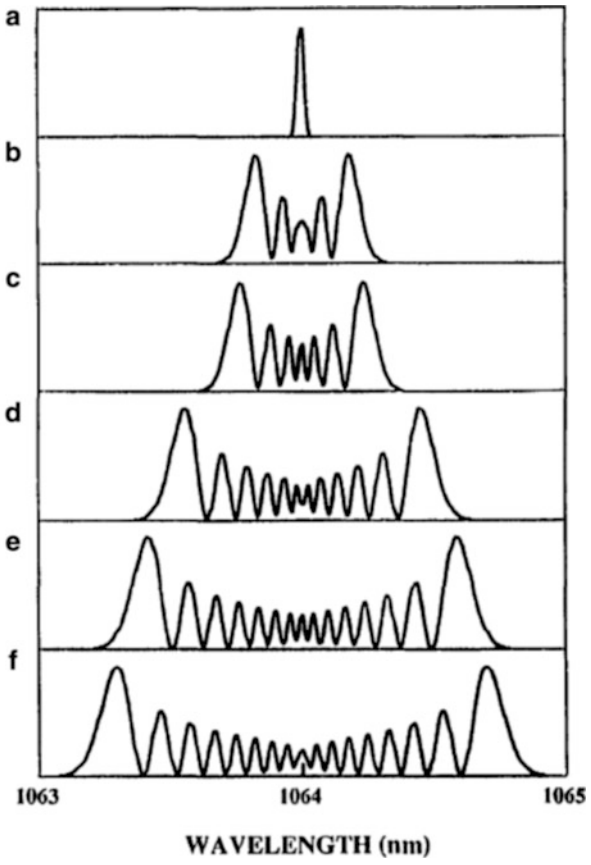

Fig. 2.32 Calculated SPM spectra of 1064-nm laser pulses propagating in an optical fiber. The core diameter of the optical fiber was 4 μm. $n_2 = 2.28 \times 10^{-16}$ cm^2/W. (**a**) Input laser, (**b**) $P_0 = 1800$ W, (**c**) $P_0 = 2300$ W, (**d**) $P_0 = 3900$ W, (**e**) $P_0 = 4900$ W, (**f**) $P_0 = 5700$ W. (From Wang et al., 1994a, b)

to control the pulse energy coupled into the optical fiber. The optical signal pulse was collected with a 20× microscope objective lens. The beam after the collecting lens was split into two. One beam was used to monitor intensities of the pulses coupled into the optical fiber by a photomultiplier tube. The other beam was passed through a spectral analysis system consisting of a 1-m spectrometer combined with a computer controlled CCD camera. The resolution of the spectral analysis system was 0.05 A/pixel for light at the 532-nm region and 0.1 A/pixel at the 1064-nm region.

Optical fibers with a core diameter of 2.5 μm and a cladding diameter of 127 μm were purchased from Corning Inc. The numerical aperture of these fibers is 0.11. Optical fibers with a core diameter of 4 μm and a cladding diameter of 125 μm were purchased from Newport Corporation. Their numerical aperture is 0.1. The optical fibers with a core diameter of 4 μm support a single mode for 1064-nm laser pulses and multimodes for 532-nm laser pulses. The 2.5-μm-core optical fibers support a single mode for 532-nm laser pulses. No detectable 1064-nm laser pulse was coupled into the 2.5-μm-core optical fiber.

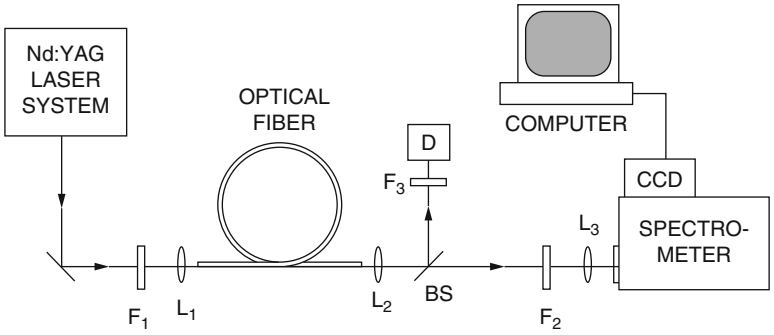

Fig. 2.33 Experimental arrangement. F_1, a set of color and neutral-density filters; F_2, F_3, neutral-density filters; L_1, L_2, 20× microscope objectives; L_3, lens. (From Wang et al., 1994a, b)

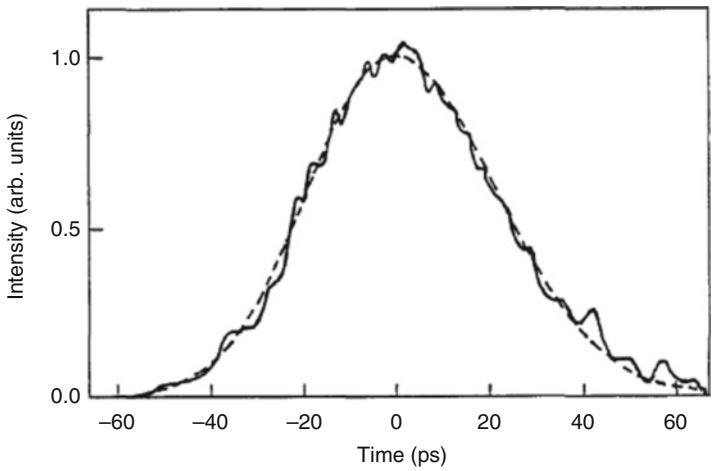

Fig. 2.34 Input laser pulse shape. The laser pulse is slightly asymmetric. The leading edge is shorter than the trailing edge. The dashed curve shows a theoretical fit to the pulse. (From Wang et al., 1994a, b)

Figure 2.34 displays an input laser pulse at 532 nm measured with a Hamamatsu 2-ps streak camera. The laser pulse is slightly asymmetric. The leading edge is shorter than the trailing edge. The dashed curve shows a theoretical fit to the pulse. Because the 532-nm pulse is the second-harmonic generation of the laser pulse at 1064 nm, the pulse width of the 1064-nm pulse is $\sqrt{2}$ times that of the 532 nm pulse, and the pulse shapes are similar.

The output spectra of the laser pulses at 532 nm with different pulse energies propagating in a 1-m optical fiber or core diameter 2.5 μm are displayed in Fig. 2.35. The salient feature of the spectra shown in Fig. 2.35 is that the spectra of the output signal pulses broaden toward both the Stokes and the anti-Stokes sides. The spectral broadening increases as the power of the input pulse increases.

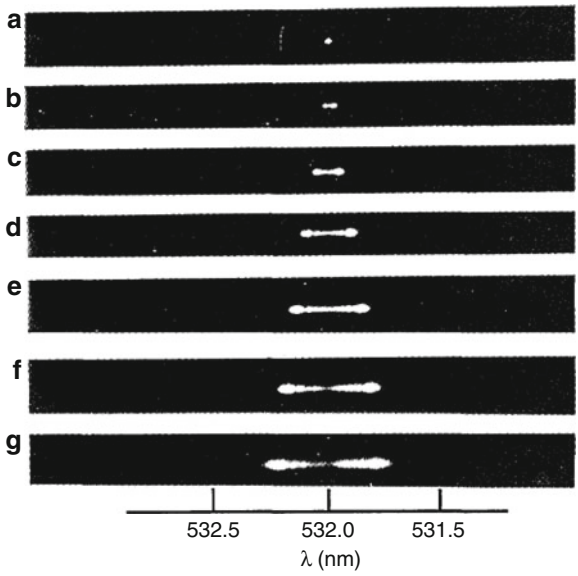

Fig. 2.35 Video display of the spectra of 532-nm laser pulses propagating in a 1-m 2.5−/−Lm-core optical fiber with different peak powers. (**a**) Input laser, (**b**) $P_0 = 110$ W, (**c**) $P_0 = 225$ W, (**d**) $P_0 = 460$ W, (**e**) $P_0 = 630$ W, (**f**) $P_0 = 790$ W, and (**g**) $P_0 = 270$ W. (From Wang et al., 1994a, b)

In addition, the broadened spectra have large intensity oscillations. In the same spectrum, the oscillation period is smaller near the central frequency and larger near both ends of the broadened spectrum. For all the spectra of different input power, the outermost maxima intensities have the largest intensities. The left-hand column of Fig. 2.34 displays some spectral curves of the broadened spectra shown in Fig. 2.35. The outermost maximum intensity on the anti-Stokes side is larger than that on the Stokes side in the same spectral curve. There are two main differences between the experimental observations shown in Figs. 2.35 and 2.36 and the theoretical calculations shown in Fig. 2.31. First, the spectral broadening of calculated spectra are symmetric about the input laser line, whereas the spectral broadening to the Stokes side is larger than that to the anti-Stokes side in the experimental observations. Second, the intensities of the maxima in the calculated spectra are symmetric about the laser line, whereas the intensities of the anti-Stokes-side maxima are larger than the corresponding maxima on the Stokes side. These two differences arise from the asymmetric input laser pulse. A set of numerical solutions of expression (2.47) with the asymmetrical experimental input laser pulse shown in Fig. 2.33 is displayed in the right-hand column of Fig. 2.34. These calculated spectra agree well with the experimental observations.

Note that no fitting parameters were used in the theoretical calculations. All the parameters used in the calculations are deduced from experimental measurements.

Figure 2.37 shows the spectra of the laser pulses at 1064 nm with different pulse energies propagating in a 1-m optical fiber of 4-μm diameter. The spectral curves are displayed in the left-hand column of Fig. 2.38. A set of numerical solutions of expression (2.47) with the asymmetrical experimental input laser pulse is shown in the right-hand column of Fig. 2.38. For the best fit of the experimental spectra, we

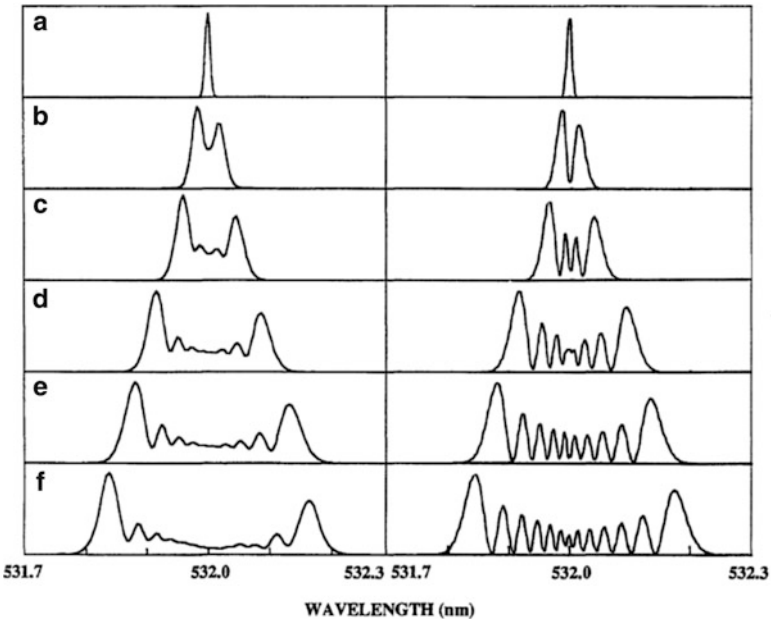

Fig. 2.36 Digital-intensity spectral curves of 532-nm laser pulses propagating in a I-m 2.5-μm-core optical fiber with different peak powers. The left-hand column shows the experimental results, and the right-hand column displays the numerical simulations. (**a**) Input laser, (**b**) $P_0 = 110$ W, (**c**) $P_0 = 225$ W, (**d**) $P_0 = 460$ W, (**e**) $P_0 = 630$ W, (**e**) $P_0 = 790$ W. (From Wang et al., 1994a, b)

used $n_2 = 2.28 \times 10^{-16}$ cm^2/W in the calculations, which is approximately 0.7 times its value for 532 nm.

2.13.3 Discussion

The SPM spectra of laser pulses at wavelengths of 532 and 1064 nm were measured with a high-resolution-grating spectral analysis system. The substructures of the SPM spectra for single-mode operations were observed and were compared with the theoretical results. The measured spectra and those calculated from SPM theory agree well for short pulses propagating in optical fibers. The subspectral structure can be useful in increasing the accuracy of the all-optical information coding. The numerical results also show that the third-order nonlinearity of the optical fibers for 1064 nm is approximately 0.7 times the value for 532 nm.

Whereas the modulation structures of the calculated spectral profiles with the SPM model fit the observed spectra, there is some difference in that the measured spectra always show a weak peak at the input laser frequency. This peak can be qualitatively understood by means of the transverse distribution of the intensity of

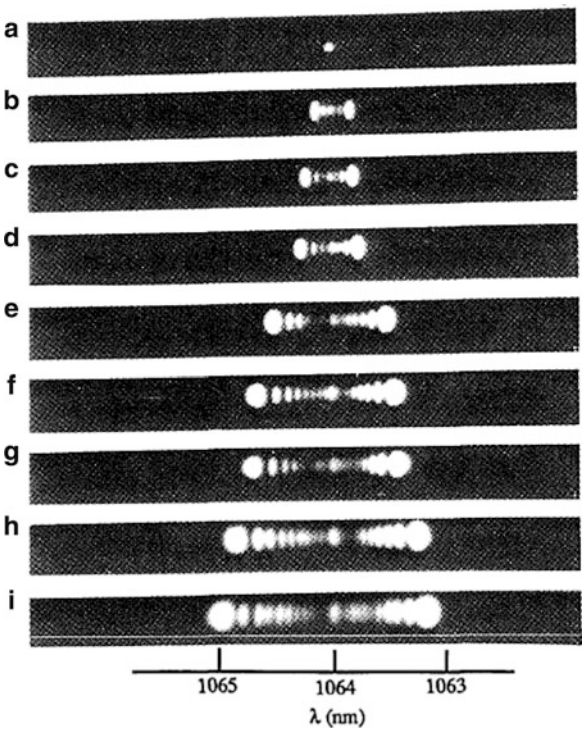

Fig. 2.37 Video display of the spectra of 1064-nm laser pulses propagating in a 1-m 4-μm-core optical fiber with different peak powers. (**a**) Input laser, (**b**) $P_0 = 1800$ W, (**c**) $P_0 = 2300$ W, (**d**) $P_0 = 3100$ W, (**e**) $P_0 = 3920$ W, (**f**) $P_0 = 4900$ W, (**g**) $P_0 = 5700$ W, (**h**) $P_0 = 6900$ W, (**i**) $P_0 = 7800$ W. (From Wang et al., 1994a, b)

the laser pulse in the optical fiber. In the calculations, it is assumed that the intensity of the optical pulse is uniformly distributed over the transverse cross section of the core of the optical fiber, whereas the laser pulse has a Gaussian distribution in the cross section for the lowest mode in practice. The laser light at the outermost area of the fiber core remains at its input wavelength because of the low intensity. The SPM process occurs near the center of the optical fiber core, where the laser pulse has the highest intensity.

Various groups have suggested that the continuum generated by picosecond pulses was not due to SPM because the extent of the spectrum was not in agreement with the SPM mechanism. The measurements and theoretical fittings clearly demonstrate the importance of using a well-defined spatial and temporal beam profile to compare experimental results with theory to confirm the SPM mechanism for continuum generation.

2.13.4 UV Supercontinuum Lower Limit in Holey Fibers

Two of important characteristics of the supercontinuum are (1) short and long wavelength extent from UV to NIR and (2) to keep the pulse structure simple to

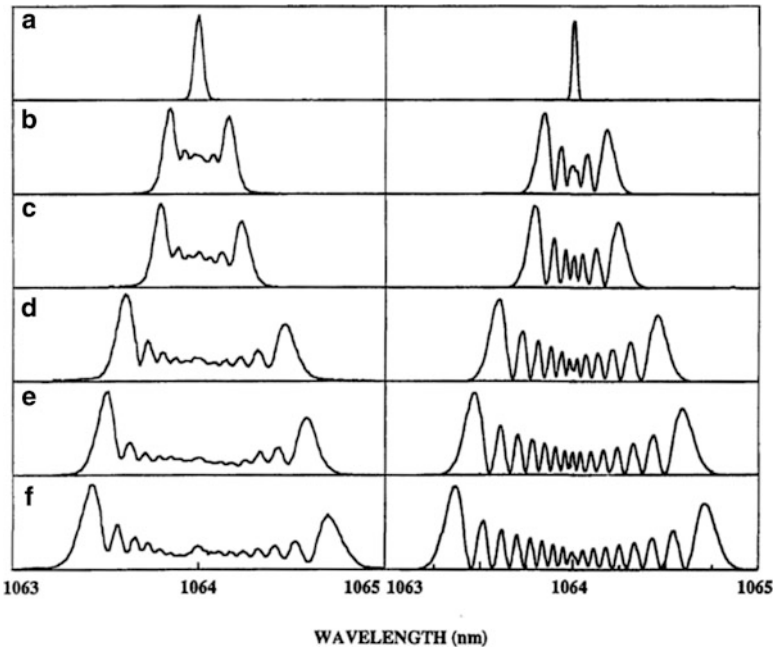

Fig. 2.38 Digital-intensity spectral curves of 1064-nm laser pulses propagating in a 1-m 2.5-μm-core optical fiber with different peak powers. The left-hand column shows the experimental results, and the right-hand column displays the numerical simulations. (**a**) Input laser, (**b**) $P_0 = 1800$ W, (**c**) $P_0 = 2300$ W, (**d**) $P_0 = 3900$ W, (**e**) $P_0 = 4900$ W, (**f**) $P_0 = 5700$ W. (From Wang et al., 1994a, b)

one pulse. It is important to operate in the normal dispersion regime or have all-normal dispersion holey fiber (see Chap. 6 by Alex Heidt) and/or keep the fiber length long enough where self-phase modulation operates.

Typically, the short wavelength limit of SC generation in a 5 μm size holey optical fiber is to about 380–400 nm, and the long wavelength can extend to 2400 nm. The UV SC limit most likely arises from linear (1P) and nonlinear two photon absorption (2PA) process from the IMAG part χ_1 of n_0 and χ_3 of n_2 to about 280 nm using tapered optical PC fibers of 620 nm diameter. The index of refraction: $n = n_0 + n_0 i + (n_2 r + n_2 i)E^2$ has real and imaginary parts for linear and nonlinear parts of the n. The UV SC generation down to $\lambda = 280$ nm (see Stark et al., 2012) is limited by 2PA and is ideal for optically exciting proteins and DNA of biological materials. See the Chap. 5 authored by Taylor and Travers in this SC book for more details on UV cutoff via 2PA and Chap. 6 authored by Heidt et al. in this book.

2.14 High-Resolution Spectra of Cross-Phase Modulation in Optical Fibers

Cross-phase modulation (XPM) is a two-(or more) beam analog or the self-phase modulation (SPM) process. It is similar to SPM, but the phase modulation is caused by the nonlinear refractive index change induced by other more intense optical pulses. When a weak optical pulse is propagating with a strong optical pulse, the phase of the weak optical pulse is modulated by the index change induced by the strong optical pulse to produce spectral broadening. This process is called XPM, which plays an important role in some ultrabroad supercontinuum generations.

XPM in optical fibers can be isolated under certain conditions so that the features of XPM can be observed. In this section, experiments performed on the fine structures of the SPM and XPM of picosecond laser pulses using a grating spectrometer with a spectral resolution higher than one tenth of the laser linewidth will be presented. Measured spectral profiles have been compared and discussed with the calculations of the SPM and XPM model (in Sect. 2.13).

2.14.1 Reduced Wave Equation

Similar to that in Sect. 2.13, from Maxwell's equations, one can obtain the wave equation that describes the amplitudes of light pulses propagating in optical fibers for XPM:

$$\frac{\partial A_1}{\partial z}+\frac{1}{v_{g1}}\frac{\partial A_1}{\partial t}+i\frac{1}{2}k_1^{(2)}\frac{\partial^2 A_1}{\partial t^2}=i\frac{\omega_0 n_2(\omega_1)}{c}\left(|A_1|^2+2|A_2|^2\right)A_1, \tag{2.50a}$$

$$\frac{\partial A_2}{\partial z}+\frac{1}{v_{g2}}\frac{\partial A_2}{\partial t}+i\frac{1}{2}k_2^{(2)}\frac{\partial^2 A_2}{\partial t^2}=i\frac{\omega_0 n_2(\omega_2)}{c}\left(|A_2|^2+2|A_1|^2\right)A_2, \tag{2.50b}$$

where ω_1 and ω_2 are the carrier frequencies of the pump and the probe pulses, and υ_{g1} and υ_{g2} are the group velocities. $k_1^{(2)}$ and $k_2^{(2)}$ are the group-velocity dispersions at ω_1 *and* ω_2, respectively, $n_2(\omega_1) = 3\ \chi^{(3)}_{1111}\ (\omega_1 = \omega_1 + \omega_1 - \omega_1)/8\ n_0\ (\omega_1)$, and $n_2(\omega_2) = 3\ \chi^{(3)}_{1111}\ (\omega_2 = \omega_2 + \omega_2 - \omega_2)/8\ n_0\ (\omega_2)$ are the nonlinear refractive index coefficients, and $n_0(\omega_i)$ is the linear refractive index. Since the fiber length used in the experiment is much smaller than the dispersion length, which can be calculated to be a few kilometers, the dispersion term in Eqs. (2.50a) and (2.50b) can be neglected.

Changing the variables

$$\tau = t - \frac{z}{v_{g1}}, \tag{2.51}$$

$$z = z' \tag{2.52}$$

and denoting by a_i and α_i the amplitude and the phase of the electric envelope, respectively, A_i can be expressed as

$$A_i\,(z,\tau) = a_i\ \ (z,\tau)\exp\left[i\alpha_i\ \ (z,\tau)\right], \tag{2.53}$$

Where $i = 1, 2$ and τ is the local time of the propagating optical pulse.

Considering the fiber lengths used in the experiment are much smaller than the dispersion lengths, which can be calculated to be a few kilometers, the dispersion term in Eq. (2.50a) can be neglected. Therefore, Eq. (2.50b) further reduces to

$$\frac{\partial a_1}{\partial z} = 0, \tag{2.54a}$$

$$\frac{\partial \alpha_1}{\partial z} = \frac{\omega_0 n_2\,(\omega_1)}{c}\left({a_1}^2 + 2{a_2}^2\right), \tag{2.54b}$$

$$\frac{\partial a_2}{\partial z} + \left(\frac{1}{v_{g1}} - \frac{1}{v_{g2}}\right)\frac{\partial a_2}{\partial \tau} = 0, \tag{2.54c}$$

$$\frac{\partial \alpha_2}{\partial z} = \frac{\omega_0 n_2\,(\omega_2)}{c}\left(2{a_1}^2 + {a_2}^2\right). \tag{2.54d}$$

The analytical solutions for Eqs. (2.54a), (2.54b), (2.54c), and (2.54d) can be obtained as

$$a_1(T) = a_{10}F_1(T), \tag{2.55a}$$

$$\alpha_1\,(L,T) = \frac{\omega_0 n_2\,(\omega_1)}{c}L\left[{a_{10}}^2{F_1}^2(T) + \frac{2}{L}{a_{20}}^2\int_0^L {F_2}^2\,(T - z/L_w)\,dz\right], \tag{2.55b}$$

$$a_1(T) = a_{10}F_1(T), \tag{2.55c}$$

$$\alpha_2\,(L,T) = \frac{\omega_0 n_2\,(\omega_2)}{c}L\left[{a_{20}}^2{F_2}^2(T) + \frac{2}{L}{a_{10}}^2\int_0^L {F_1}^2\,(T + z/L_w)\,dz\right]. \tag{2.55d}$$

where a_{i0} are the amplitudes, $F_i(t)$ are the pulse envelopes, $T = \tau/T_0$, $L_w = T_0/\left(\frac{1}{v_{g2}} - \frac{1}{v_{g1}}\right)$ is the walk-off length of the pump and probe pulses, and T_0 is the $1/e$ pulse duration.

One can obtain the field spectral profiles of XPM by computing the Fourier transformation of its temporal pulse distribution as

$$E_i\,(z, \omega - \omega_i) = \frac{1}{2\pi}\int a_i\,(z, \tau)\exp\left[\left(i\alpha_i\left(z, \tau\right)\right]\right]\exp\left[i\,(\omega - \omega_i)\,\tau\right]d\tau. \tag{2.56}$$

The spectral-intensity distribution of the pulse is given by

$$|E_i\,(z, \omega - \omega_i)|^2. \tag{2.57}$$

2.14.2 Experiment

The experimental arrangement is shown in Fig. 2.39. A 10-Hz mode-locked Continuum Nd:YAG laser system was used to generate linearly polarized laser

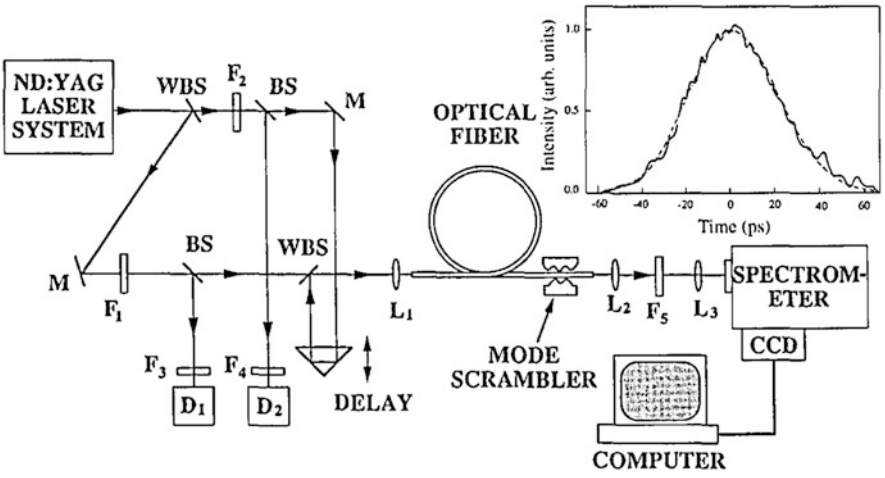

Fig. 2.39 Experimental arrangement: F_1, a set of color and neutral-density filters; F_2–F_3, neutral-density filters; L_1, L_2, 20× microscope objectives; L3, lens; BS's, beam splitters; D_1, D_2, detectors; M's, mirrors. Inset: The pulse shape of the 532-nm laser pulse generated from the laser system. The laser pulse is slightly asymmetric. The leading edge is shorter than the trailing edge. The dashed curve shows a theoretical fit to the pulse. (Reprinted with permission from Wang et al., 1994b © Optical Society of America)

pulses at 1064 and 532 nm. An electronic optical shutter in the laser cavity allows for single-pulse operation. The inset shows an input laser pulse at 532 nm measured with a Hamamatsu 2-ps streak camera. The laser pulse is slightly asymmetrical. The leading edge is shorter than the trailing edge. The dashed curve shows a theoretical fit to the pulse. The leading part of the dashed curve is the front part of a Gaussian pulse with FWHM of 40 ps. The trailing part is the back part of a Gaussian pulse with a FWHM of 50 ps. Because the 532-nm pulse is the second-harmonic generation of the laser pulse at 1064 nm, the pulse width of 1064 nm pulse is approximately $\sqrt{2}$times that of the 532-nm pulse. The pulse shapes are similar. The pulse energies were approximately 2 mJ and 200 nJ for 1064 and 532 nm, respectively. The 1064- and 532-nm laser pulses were separated by a wavelength-selective beam splitter (WBS). These beams were combined by another WBS after propagating along different paths. A polarization rotator was inserted into the 1064-nm beam path to change the polarization to be parallel to that of the 532-nm beam. The optical path of the 532-nm pulse was controlled by variable optical delay. Two sets of filters were used in the two different paths to control the pulse energies. The intensities of the laser pulses were monitored with a photomultiplier tube and a photodiode. The laser pulses were coupled into a 1-m optical fiber with a 20× microscope objective lens. The output signal pulse was collected with a 20× microscope objective lens. An optical fiber with core diameter of 4 μm, a cladding diameter of 125 μm, and a numerical aperture of 0.11 was purchased from Newport. This optical fiber supports a single mode for 1064-nm pulses and multimodes for 532-nm laser pulses. By carefully adjusting the coupling to the optical fiber, we coupled more than 90% of light at 532 nm into the lowest mode of the fiber. The small portion of light at 532 nm coupled into higher modes was removed by a mode scrambler applied 5 cm away from the output end of the optical fiber. The output signal beam was passed through a spectral analysis system consisting of a 1-m spectrometer combined with a computer-controlled CCD camera. A 1200-groove/mm grating blazed at 1000 nm was used in the spectrometer, which enabled us to measure effectively the first-order spectrum of an optical pulse at the 1064-nm region and the second-order spectrum of an optical pulse at the 532-nm region simultaneously. The resolution of the spectral analysis system was 0.01 nm/pixel and 0.005 for the 1064- and 532- nm regions, respectively.

The output XPM spectra of the probe pulse at 532 nm and the SPM spectra of the pump laser pulse at 1064 nm propagating in 1-m optical fiber are shown in Fig. 2.40. The spectrum of the input probe pulse is shown in Fig. 2.40a. The XPM spectra for different initial time delays between the pump and the probe pulses at a constant pump intensity are shown in Fig. 2.40b–d. The SPM spectrum of the pump pulse is shown in Fig. 2.40e. When the pulses coincide at the input end of the fiber, the probe pulse sees only the trailing part of the pump pulse when it propagates in the optical fiber, because of the walk-off effect. The phase of the probe pulse is then modulated by the induced index change caused by the trailing edge of the pump pulse, and the spectrum of the probe pulse is shifted to the anti-Stokes-side only, as shown in Fig. 2.40b. When the probe pulse is 31 ps ahead of the pump pulse at the fiber entrance, the phase of the probe pulse undergoes a symmetric modulation

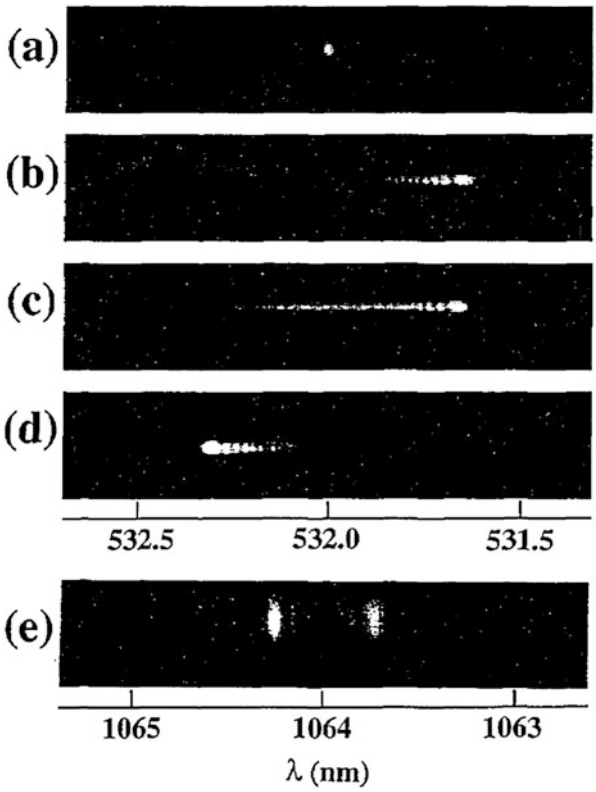

Fig. 2.40 Video display of the SPM spectra of the pump pulse at 1064 nm and the XPM spectra of the probe pulse at 532 nm propagating in 1-m, 4-μm-core optical fiber with different initial time delays between the pump and probe pulses: (**a**) input laser linewidth, (**b**) $t_d = 0$ ps, (**c**) $t_d = 31$ ps, (**d**) $t_d = 63$ ps, (**e**) SPM spectrum of the pump pulse. The peak power of the pump pulse is −2000 W. (Reprinted with permission from Wang et al., 1994b © Optical Society of America)

on both the leading and the trailing edges of the pump pulse in the optical fiber. The XPM spectrum broadens toward both the Stokes and the anti-Stokes sides, as can be seen from Fig. 2.40c. When the probe pulse is initially set approximately 63 ps before the pump pulse, the probe pulse sees only the leading part of the pump pulse in the optical fiber. The spectrum of the probe pulse broadens to the Stokes side only, as displayed in Fig. 2.40d. In addition, the intensity oscillation structures of the XPM and SPM spectra caused by the interference are resolved because of the high spectral resolution of the measurement system. Both the XPM and SPM spectra have large intensity oscillations. In the same spectrum, the oscillation period is smaller near the input frequency and gets larger as the spectrum goes further away from the input frequency. For pump pulses at 1064 nm, Fig. 2.40e shows that the SPM spectral broadening to the Stokes side is larger than that to the anti-Stokes

side. This effect arises from the asymmetric temporal distribution of the input laser pulse. The leading edge of the input laser pulse is shorter than the trailing edge. For all the cases, the spectral broadenings increase as the pump intensity increases.

2.14.3 Discussion

In Fig. 2.41, the digitized experimental spectral curves and the numerical calculations of the changes of the XPM and SPM spectra of the probe and pump pulses are displayed in the left and the right columns, respectively. In the left-hand column of Fig. 2.41, the thick solid curves are the digitized XPM spectral curves of the probe pulse, and the thin solid curves are the experimental SPM spectra of the pump pulse. In the right-hand column, the solid curves are the XPM spectra of the probe pulse, and the dotted curves are the SPM spectra of the pump pulse. The spectra of the input laser pulses are shown in Fig. 2.41a. Figure 2.41b–d show the XPM and SPM spectra for different initial time delays between the probe and the pump pulses at a

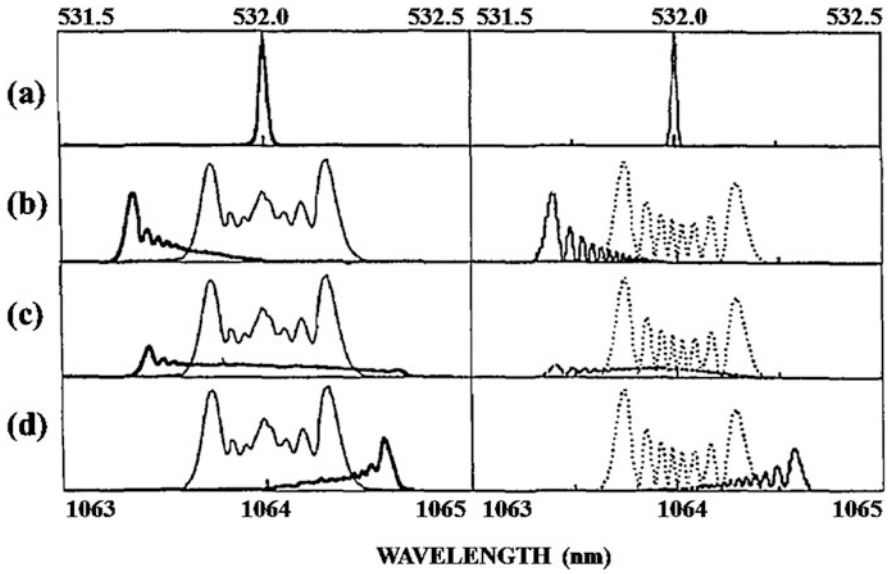

Fig. 2.41 SPM of the pump pulse at 1064 nm and XPM spectra of the probe pulse at 532 nm propagating in an optical fiber with different initial time delays. The left-hand column shows the experimental results, and the right-hand column shows the theoretical calculations. The core diameter of the optical fiber was 4 μm, and $n_2 = 3.2 \times 10^{-16}$ cm^2/W for 532 nm and $n_2 = 1.79 \times 10^{-16}$ cm^2/W for 1064 nm. (**a**) Input laser pulse, (**b**) $t_d = 0$ ps, (**c**) $t_d = 31$ ps, (**d**) $t_d = 63$ ps. The peak power of the pump pulse is 2000 W. (Reprinted with permission from Wang et al., 1994b © Optical Society of America)

constant pump intensity. The theoretical results for $t_d = 0$ and $t_d = 63$ ps reasonably agree with the experimental results shown in Fig. 2.41b–d.

For the best fit of the experimental spectra, $n_2 = 1.79 \times 10^{-16}$ cm^2/W at 1064 nm was used in the calculations, that is ~0.56 times the value for n_2 at 532 rm. Because of the high resolution of the SPM and XPM spectra, small changes of the XPM and SPM spectra caused by the small differences of the nonlinearity can be resolved. By fitting the spectral change, we can measure the small difference between the third-order nonlinearities at the wavelengths of the pump and probe pulses. With our high spectral resolution, depending on the stability of laser pulses, the accuracy of the detected dispersion of the third-order nonlinearity between the pump and the probe wavelengths is estimated to be ~5%.

2.15 Recent Developments of Supercontinuum Generation

Since the discovery made 51 years ago by Alfano and Shapiro (1970a), the supercontinuum generation has been the subject of numerous investigations in a wide variety of nonlinear media and various applications in Physics, Chemistry, Biology, and soon to Medical fields. Over past 24 years, there has been a surge of activity in supercontinuum field using various types of photonic crystal fibers after the first introduction (Russell et al., 1996, 1997). The advancement in the generation of ultrashort laser pulses led to the production of a wider supercontinuum generation that resulted in applications of supercontinuum generation in a diverse range of fields. These applications include optical coherence tomography (Hartl et al., 2001; Hsiung et al., 2004), frequency metrology (Ranka et al., 2000; Jones, 2000; Schnatz & Hollberg, 2003), fluorescence lifetime imaging (Dunsby et al., 2004), optical communications (Takara et al., 2005; Morioka et al., 1993), gas sensing (Sanders, 2002; Ere-Tassou et al., 2003), and many others. The practice of these sources has created a feedback loop whereby the scientists utilizing the supercontinua are demanding better customizable continua to suit their particular applications. This has driven researchers to develop novel methods to produce these continua and to develop theories to understand their formation and aid future development. Rapid progress in supercontinuum generation has been made since 2000. Extremely broad supercontinuum spectra have been produced with various kinds of photonic-crystal optical fibers, optical waveguides, and engineered integrated bulk. Spectrum of supercontinuum generation covers the wider wavelength regions in the deep ultraviolet (DUV), the ultraviolet (UV), the visible, near infrared (NIR), and the infrared (IR).

2.15.1 Nonlinear Refractive Index of Materials Used in Supercontinuum Generation

Buckingham (1955; Boyle et al., 1966; Buckingham & Hibbardas, 1968) expanded on John Kerr's work (Kerr, 1875) by introducing the hyperpolarizability of the first and second kinds. These became most important parameters in nonlinear optics related to the nonlinear index change n_2 as the main mechanism for supercontinuum generation, higher harmonic generation, and attosecond pulse generation. The third-order nonlinearity $\chi^{(3)}$ makes the refractive index to depend on the intensity of light propagating through the medium (Maker et al., 1964; Maker & Terhune, 1965). As optical pulses become shorter and intense, the third-order nonlinearity $\chi^{(3)}$ becomes of increasing interest because its role in Supercontinuum generation via n_2. When optical waves propagate through a medium with the inversion symmetry, third-order nonlinearity can be conveniently described as an intensity dependent index (Yariv, 1975) by average over many optical cycles:

$$n = n_0 + n_2 \left\langle E^2 \right\rangle, \tag{2.58}$$

where n_0 is the linear refractive index, E is the applied optical electric field, and n_2 is the nonlinear refractive index. Buckingham gave the instantaneous index $n(t)$ with the full form of $E(t)$ which forms the response of $n(t)$ to electronic and molecular motions.

Measurements of the nonlinear refractive index were performed for various materials. Tables 2.4a, 2.4b, 2.4c, and 2.4d list measurement results of some optical materials (Bokov, 1974; Milam et al., 1977; Adair et al., 1989; etc.).

The units of that quantity are m^2/W (or cm^2/W) in the SI system, but in older literature, one finds n_2 values in esu units. For the conversion of such units, Eq. (2.59) can be used:

$$\begin{aligned} n_2\left(m^2/W\right) &= \frac{40\pi}{c}\frac{n_2(\text{esu})}{n} \\ &= 4.19 \times 10^{-7} \times \frac{n_2(\text{esu})}{n}\,. \end{aligned} \tag{2.59}$$

where n is the refractive index.

For example, for liquid Kr, $n = 1.30$, $n_2 = 1.36 \times 10^{-13}$ esu

$$\begin{aligned} n_2\left(m^2/W\right) &= 4.19 \times 10^{-7} \times \frac{1.36\times10^{-13}}{1.30}\left(m^2/W\right), \\ &= 4.38 \times 10^{-20}\left(m^2/W\right), \\ &= 4.38 \times 10^{-16}\left(cm^2/W\right). \end{aligned}$$

Table 2.4a Nonlinear index of refraction $n_2 \times 10^{13}$ of several liquids (in cgs esu)

Liquid	$\frac{Z}{(\overline{r})^6} \cdot 10^{-45}$, cm^{-6}	$\gamma \cdot 10^{36}$cgs esu	Onsager Model (9)						K · 10^{13} cgs esu	n_2 ex	theor n_2 Lor(8)
			n_2 hyp	n_2 rad	$n_2^{(0)}$ Kerr	n_2^{int} Kerr	$n_2$qu	(theor)n_2 Ons			
Aragon	3.38	0.59	0.54	1.54				2.08			2.34
Cabon tetrachloride	0.219	9.96	3.66	17.50				21.16	4.76	5.80	27.77
Benzene	0.214	6.46	2.53	21.74	30.00	35.24		59.51	35.00	37.00	87.05
Toluene	0.150	27.20	8.83	25.43	38.84	45.58		79.84	45.40	51.54	116.24
Carbon disulfide	0.262	57.35	37.13	31.50	131.30	157.32	27.64	253.59	194.20	254.95	435.26
Chloroform	0.146	4.80	1.44	4.12	3.59	3.90		9.46	10.00	9.76	17.83
Nitrobenzene	0.219	85.00	23.28	40.07	45.43	73.40		136.75	141.50	144.17	323.70

Recreated according Bokov (1974)

(8) : $n_{2\,\text{Lor}} = 4\pi N L_{\text{Lor}}^4 \alpha_2 / 2n_0$ (9) : $n_{2\,\text{ons}} = \frac{2\pi N}{n_0 G} L_{\text{Ons}}^4 \alpha_2$

Table 2.4b Nonlinear refractive-index coefficients γ of fluoride crystals measured interferometrically using linearly polarized 125 ps, 1064 nm laser pulse and calculated from Eqs. (2.3a and 2.3b)

Material	Structure type	n_D	V	γ (10^{-20}m^2/W)[a]	
				Measured	Calculated
LiF	Cubic (NaCl)	1.392	99	1.05 ± 0.30	1.18
NaF	Cubic (NaCl)	1.326	85	1.37 ± 0.34	1.19
CaF_2	Cubic (fluorite)	1.434	95	1.90 ± 0.26	1.42
SrF_2	Cubic (fluorite)	1.438	92	1.76 ± 0.29	1.51
BaF_2	Cubic (fluorite)	1.475	82	2.85 ± 0.57	1.97
CdF_2	Cubic (fluorite)	1.576	61	3.87 ± 0.54	3.93
PbF_2	Cubic (fluorite)	1.769	34	11.7 ± 2.90	13.97
MgF_2	Tetragonal (rutile)	1.378 (*o*)1.389 (*e*)	108	0.92 ± 0.31	0.99
LaF_3	Hexagonal (tysonite)	1.603 (*o*)1.600 (*e*)	57	3.95 ± 0.72	4.63
CeF_3	Hexagonal (tysonite)	≈1.60	≈55	4.06 ± 0.93	4.85
$LiYF_4$	Tetragonal (scheelite)	1.457 (*o*)1.477 (*e*)	93	1.72 ± 0.20	1.56

From Milam et al. (1977)

[a]To convert to n_2(esu), multiply γ(m^2/W) by $2.39 \pm 10^6 n$

(3) $n_2\left(10^{-13}\text{esu}\right) = K\frac{(n_d-1)\left(n_d^2+2\right)^2}{v\left[1.517+\left(n_d^2+2\right)(n_d+1)v/6n_d\right]^{1/2}}$

2.15.2 *Mid-Infrared Supercontinuum Generation Covering 1.4–13.3 μm*

The mid-infrared spectral region is of great technical and scientific interest because most molecules display fundamental vibrational absorptions in this region, leaving distinctive spectral fingerprints (Schliesser et al., 2012; Allen, 1998).

The interaction of mid-IR radiation with a given sample provides a spectral fingerprint useful for identification of the sample. The mid-IR spectrum results from the absorption of specific frequencies of mid-IR radiation based on the chemical structure of the sample. For this reason, the peaks and troughs in a mid-IR spectrum are very specific to the sample measured. This makes mid-IR spectroscopy well suited for a wide range of applications involving materials identification and characterization for measurements ranging from the analysis of fuels to food safety and detection of counterfeit materials. These applications and many others benefit from the fundamental bands measured with mid-IR, which yield a higher intensity, less convoluted spectra than the overtone and combination bands measured with near-IR and visible radiation.

Mid-IR spectroscopy is widely used by researchers and educators for basic and applied research and for teaching labs in Physics, Chemistry, and Biomedical courses, such as early cancer diagnostics (Seddon, 2011), gas sensing (Allen, 1998; Eggleton et al., 2011), and food quality control (Wegener et al., 1999).

A mid-infrared supercontinuum spanning 1.4–13.3 μm is generated using short pieces of ultrahigh numerical-aperture step-index chalcogenide glass optical fiber by

Table 2.4c Nonlinear- and linear-refractive index of optical crystals (*o* denotes ordinary, *e* extraordinary)

	Linear –index data		Nonlinear-index data	
Sample	n(1.06 μm)	Abbe number v_d	Measured $n_2(10^{-13}$esu)	Calculated $n_2(10^{-13}$esu)
LiF [100]	1. 3866[a]	98.0	0.26	0.40
NaF [100]	1. 3213[a]	85.2	0.34	0.38
KF [100]	1. 3583[a]	97.9	0.75	0.36
NaCl [100]	1. 5312[a]	42.9	1.59	2.28
KC1 [100]	1. 4792[a]	44.1	2.01	1.84
NaBr [100]	1.6228[a]	31.7	3.26	4.74
KBr [100]	1. 5435[a]	33.7	2.93	3.41
MgF_2(*o*)	1. 3735[b]	104.9	0.25	0.34
CaF_2 [100]	1. 4285[c]	95.1	0.43	0.49
SrF_2 [100]	1. 4328[b]	93.9	0.50	0.50
CdF_2 [100]	1. 56[d]	61.0	3.95	1.37
BaF_2 [100]	1. 4682[b]	81.8	0.67	0.70
LaF_3 (*o*)	1.60*	57.0	1.4	1.78
CeF_3 (*o*)	~1.60[c]		1.3	
AgCl (polycryst.)	2.020[b]	21.2	23.3	23.0
MgO [100]	1. 72[c]	53.4	1.61	2.8
CaO [100]	1. 83[e]		5.20	
SrO [l10]	1. 81[e]		5.07	
ZnO (*e*)	1. 96[c]	11.6	23.0	57.6
ZnO (*o*)	1. 99[c]	12.3	25.0	45.0
$A1_2O_3$(*o*)	1. 75[c]	71.8	1.23	1.9
$A1_2O_3$(*e*)	1. 75[c]	75.2	1.30	1.8
Ga_2O_3	1. 96[b]		5.80	
Y_2O_3	1. 92[a]	37.5	5.33	7.2
Er_2O_3	1. 96[f]		4.53	
SiO_2 (fused)	1. 4496[c]	67.8	0.85	0.83
SiO_2 (quartz) (*o*)	1. 5342[c]	71.6	1.12	1.06
SiO_2 (quartz) (*e*)	1. 5429[c]	70.1	1.16	1.13
TiO_2	2. 48[b]	9.8	55.8	189
ZrO_2	2. 12[b]	35.8	5.8	12.6
$BeAl_2O_4$	1.73[b]	72.5	1.46	1.74
$MgAl_2O_4$	1. 73[b]	60.6	1.50	2.3
$CaMgSi_2O_6$	1. 67[g]		1.73	
$YAIO_3$ (γ)	1. 933[b]	51.2	3.37	4.88
Y_3A15O_{12} (YAG)	1. 822[b]	52.4	2.7	3.6

(continued)

Table 2.4c (continued)

Sample	Linear –index data		Nonlinear-index data	
	n(1.06 μm)	Abbe number v_d	Measured $n_2(10^{-13}$esu)	Calculated $n_2(10^{-13}$esu)
$Gd_3Sc_2Al_3O_{l2}$ (GSAG)	1. 891[h]	48.0	4.0	5.6
$Gd_3Sc_2Ga_3O_{12}$ (GSGG)	1. 943[i]	37.3	5.5	8.0
$Gd_3Ga_5O_{12}$ (GGG)	1. 945[b]	37.6	5.8	8.0
$Y_3Ga_5O_{12}$ (YGG)	1. 912[j]	40.0	5.2	5.8
$La_3Lu_2Ga_3O_{12}$ (LLGG)	1.930[i]	36.4	5.8	8.2
$SrTiO_3$	2. 31[c]	13.6	26.7	83.0
$CaCO_3$ (*o*)	1. 6425[c]	47.6	1.11	2.7
$CaCO_3$ (*e*)	1. 4795[c]	76.8	0.83	0.79

Reprinted with permission from Adair et al. (1989) © The American Physical Society

Table 2.4d Nonlinear refractive index of optical materials

Materials	Wavelength	Nonlinear index (n_2)
Ar (gas)	800 nm	1.08×10^{-19} cm^2/W bar (Wang et al., 2013)
	1800 nm	6.65×10^{-20} cm^2/W bar (Wang et al., 2013)
	1055 nm	10.9×10^{-20} cm^2/W (Bree et al., 2010)
Ar (liquid)	530 nm	2.04×10^{-16} cm^2/W (Alfano, 1972)
Kr (liquid)	530 nm	4.38×10^{-16} cm^2/W (Alfano, 1972)
BK7	810 nm	3.625×10^{-16} cm2/W (Lu et al., 2012)
Methanol (liquid)	1064 nm	1.8×10^{-15} cm^2/W (Rau et al., 2008)
CdS	532 nm	-3.79×10^{-11} cm^2/W (Ganeev et al., 2003)
As_2S_3	1064 nm	5.09×10^{-10} cm^2/W (Ganeev et al., 2003)
GaAs	1060 nm	4×10^{-14} cm^2/W (Hurlbut et al., 2007)
Si	1600 nm	5.5×10^{-14} cm^2/W (Dremetsika et al., 2016)

launching intense ultrashort pulses with a central wavelength of 6.3 μm (Petersen et al., 2014). Typical output spectrum and beam profile are shown in Fig. 2.42.

2.15.3 Enhanced Bandwidth of Supercontinuum Generated in Microstructured Fibers

Coherent octave spanning supercontinuum can be generated in photonic crystal fiber by launching into the fiber femtosecond pulses with a wavelength located near the zero-dispersion wavelength (λ_{ZD}) of the photonic crystal fiber (Holzwarth et al.,

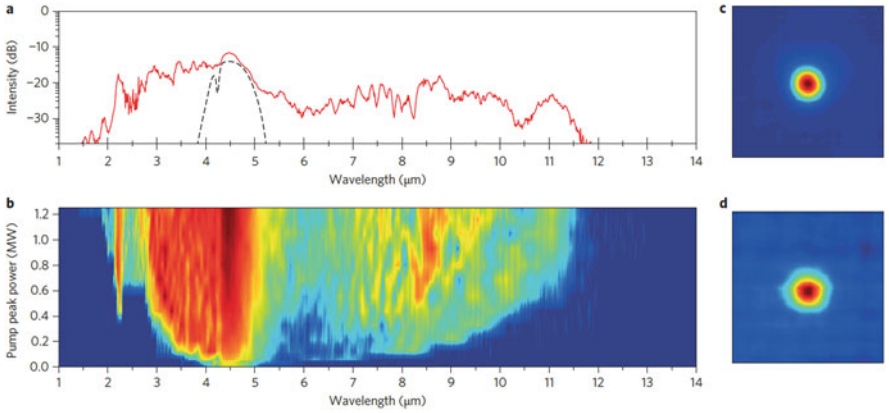

Fig. 2.42 Experimental supercontinuum generation results with the pump centered at 4.5 μm. (**a**) Input pump spectrum (dashed line) and spectral profile at maximum pump power (solid line), showing a relatively flat supercontinuum (2.08–10.29 μm at −20 dB from the signal peak) with distinct soliton peaks above the zero dispersion wavelength of ~5.83 μm, especially at 11 μm. (**b**) Spectral evolution with increasing pump peak power, showing a gradual redshift of distinct soliton peaks above the zero dispersion wavelength, and a combination of SPM and dispersive waves below the pump wavelength. (**c**, **d**) Fiber output near-field beam profile corresponding to the spectrum in a for all wavelengths (**c**) and beam profile for wavelengths above 7.3 μm only (**d**), showing that the long wavelengths are still confined to the core. (Reprinted from Petersen et al., 2014 © Macmillan Publishers Limited)

2000). For a pump wavelength on the anomalous side of λ_{ZD}, it has been shown that the fundamental mechanism leading to the supercontinuum generation mainly involves two distinct physical effects: Amplification of dispersive waves matched in phase with the pump extends the supercontinuum to the blue (Husakou & Hermann, 2002, 2003; Akhemediev & Karlsson, 1995), whereas pulse splitting and multiple soliton self-frequency shifts are responsible for the spreading of the supercontinuum into the infrared (Genty et al., 2002; Dudley et al., 2002).

Designing a photonic crystal fiber so that it has two λ_{ZD}'s, one in the visible (λ_{ZDV}) and another in the vicinity of 1500 nm (λ_{ZDI}), and properly adjust the pump wavelength, a substantial increase of the bandwidth of the supercontinuum in the infrared has been obtained while still efficiently generating the blue wavelength components (Genty et al., 2004a, b). Figure 2.43 shows the typical supercontinuum spectra.

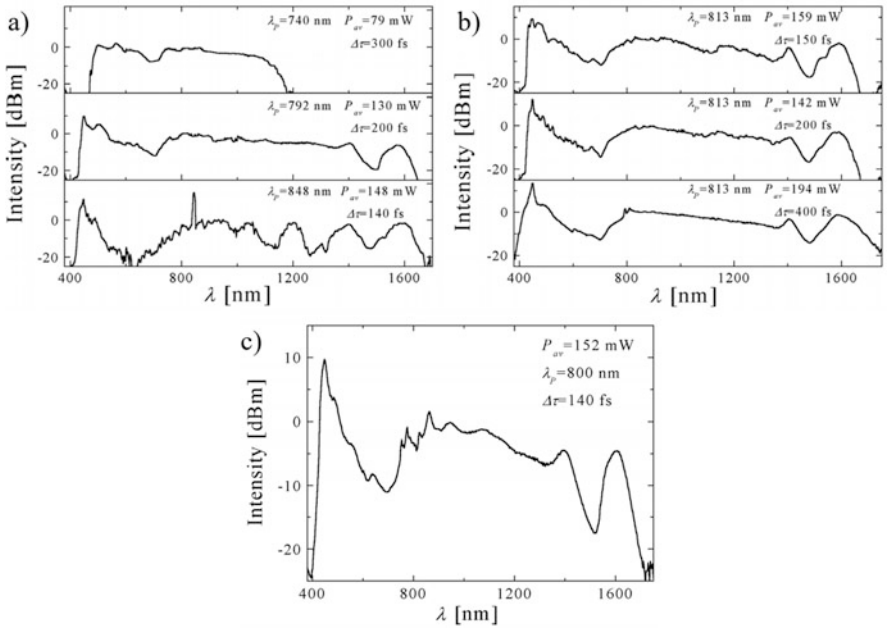

Fig. 2.43 Supercontinuum spectrum recorded when (**a**) tuning the pump wavelength and (**b**) varying the input pulse. (**c**) Supercontinuum generated in 50 cm of fiber with visible $\lambda_{ZDV} = 690$ nm and infrared $\lambda_{ZDI} = 1390$ nm. (Reprinted with permission from Genty et al., 2004b © Optical Society of America)

2.15.4 Deep-Ultraviolet to Mid-Infrared Supercontinuum Generation

Triggered by a tremendous number of applications, such as semiconductor metrology and inspection (Stokowski & Vaez-Iravani, 1998), pump-probe spectroscopy (Riedle et al., 2013; Petersen et al., 2018a), pollution monitoring (Popov et al., 1997), optical coherence tomography, and imaging (Colley et al., 2007; Petersen et al., 2018b), fiber-based laser sources capable of covering the electromagnetic spectrum from DUV (wavelengths <350 nm) up to mi-IR have attracted the scientific attention around the globe. One of the most promising routes toward development of ultrabroad bandwidth sources is supercontinuum generation.

Most reports on supercontinuum generation in the literature are based on solid-core silica photonic crystal fibers (PCF) where the micro-structured cladding of the fiber allows tailoring of the group velocity dispersion (GVD), which is an important property that greatly influences the nonlinear effects (Dudley et al., 2006). Despite silica solid-core PCF-based supercontinuum sources now being commercially available, they can only operate in a limited transmission range around 350–2300 nm due to the limited transparency window of the silica material.

In 2015, Jiang et al. reported for the first time the fabrication of a fluoride (ZBLAN) glass-based solid-core PCF with high air-filing fraction, and they demonstrated a broad supercontinuum spanning more than three octaves in the spectral range of 200–2500 nm (Jiang et al., 2015).

Experimental demonstration of multioctave supercontinuum generation spanning from DUV to mid-IR in a gas-filled HC-ARF pumped directly in the mid-IR region at 2460 nm using a tunable optical parametric amplifier (OPA) system was first reported in 2019 (Adamu et al., 2019). By coupling 100 fs, 20 μJ pulses into a specially designed argon (Ar) filled HC-ARF under 30 bar pressure, soliton self-compression dynamics enabled broadening from 200 to 4000 nm. Furthermore, it was experimentally demonstrated how the pulse energy and the pressure have a crucial role in the mid-IR spectral broadening and emission of DWs in the DUV. Typical spectra are shown in Fig. 2.44.

The supercontinuum embedded in a 4.3-octave-wide spectrum spans from 200 nm up to 4000 nm when 8 μJ, 100 fs pulses are injected into the fiber filled with Ar at a pressure of 30 bar. A total measured average output power of 5 mW (at 1 kHz

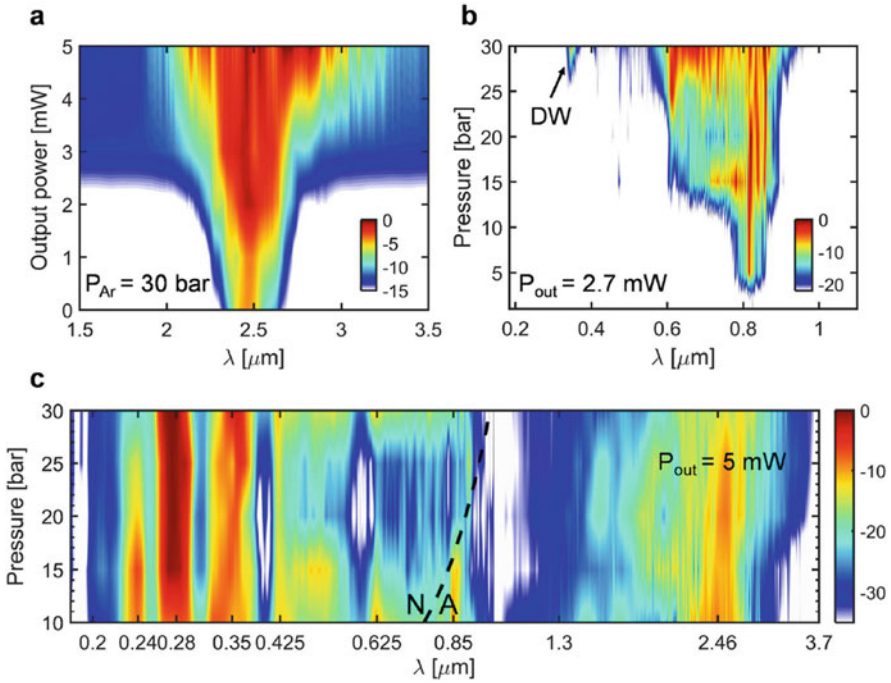

Fig. 2.44 (**a**) Measured spectral evolution and DW formation in the near/mid-IR range indicating the spectrum broadening as a function of measured output power for a fixed pressure of 30 bar. (**b**) Spectral broadening and DW emission as a function of pressure in the DUV/visible. (**c**) Pressure dependent evolution of the spectrum at a fixed low power of 5 mW over the full spectrum from 10 up to 30 bar with a step of 5 bar. (Reprinted from Adamu et al., 2019)

repetition rate) was obtained with a strong resonant DW emission at 275 nm. Finally, it was experimentally demonstrated how the pump energy and pressure increases the nonlinearity resulting in increased mid-IR spectral broadening and efficient DW emission in the DUV range. The current work constitutes an efficient route toward ultrafast source for spectroscopy both in the mid-IR molecular fingerprinting and in the DUV spectral region.

2.15.5 Summary of Selected Supercontinuum Generation Since 2000

Because of its ability to confine light in hollow cores or with confinement characteristics not possible in conventional optical fiber, photonic crystal fiber (PCF) (Knight et al., 1996), the nonlinearity can be increased and the zero dispersion wavelength can be engineered in PCF. These two properties make PCF an excellent medium for supercontinuum generation. There have been a lot of work for supercontinuum generation using PCF (Dudley et al., 2006). There are also other areas of development of supercontinuum generation, including the development of fibers to include new material, production techniques, and tapers, generating supercontinuum in gases, crystal waveguides, and gas-filled hollow-fibers.

An in-depth discussion of these achievements is beyond this chapter. Table 2.5 highlights the major achievements in supercontinuum generation since 2000.

2.16 Overview

Supercontinuum generation is the generation of bursts of E&M which cover wide band of frequency in the so-called "Maxwell Rainbow" most noted as in visible earlier in the "white light," which can be obtained by passing intense picosecond or femtosecond pulses through various materials in gases, liquids, and solids. The supercontinuum is an universal effect and enabling technology. Supercontinuum now covers most of Maxwell Rainbow, the X ray, XUV, UV, Visible, NIR, MIR, IR, THz, and RF spectra zones. The nonlinear response of the medium n_2 and the pulse envelope yield a phase modulation that usually initiates the wide frequency broadening (up to 10,000 cm^{-1}). The extreme femtosecond laser pulse changes the carrier envelope phase (CEP) in time from electronic cloud and molecular changes causing the ultrasuper broadening and higher harmonic generation over large portion of the Maxwell Rainbow. The phase modulation can be generated by the pulse itself, a copropagating pump pulse, or the copropagating stronger pulse in cross-phase modulation (XPM). These different configurations are called self-phase modulation (SPM), induced-phase modulation (IPM), and cross-phase modulation (XPM), respectively. The SPM process for supercontinuum generation in various

Table 2.5 Brief summary of major achievements on supercontinuum generation in condensed matter since 2000

Investigator	Year	Material	Pump wavelength, pulse width, power/energy	Spectrum	Process
Ranka, J. K., R. S. Windeler, and A. J. Stentz	2000	Photonic crystal fiber (air-silica)	790 nm, 100 fs, 800 pJ	390–1600 nm	SPM, Raman scattering
Birks, T. A., W. J. Wadsworth, and P. St. J. Russell	2000	Tapered fiber (1.8 μm)	850 nm, 200 fs, 3.9 nJ	370–1545 nm	SPM, Raman scattering
Husakou, A. V., and J. Herrmann	2001	Photonic crystal fibers	770 nm, 10 fs, 3.3 TW/cm^2	500–1300 nm	Fission of higher-order solutions
Provino, L., J. M. Dudley, H. Maillotte, N. Grossard, R. S. Windeler, and B. J. Eggleton	2001	Photonic crystal fibers	532 nm, 0.8 ns, 400 W (peak)	450–800 nm	Stimulated Raman scattering, FWM
Coen, S., A. H. L. Chau, R. Leonhardt, J. D. Harvey, J. C. Knight, W. J. Wadsworth, and P. St. J. Russell	2001	Photonic crystal fibers	647 nm, 60 ps, 675 W (peak)	400 to >1000 nm	Stimulated Raman scattering, phase-matched parametric process
Genty, G., M. Lehtonen, H. Ludvigsen, J. Broeng, and M. Kaivola	2002	Photonic crystal fibers	804 nm, 100 fs, 45 mW (average, 80 MHz)	400 to >1400 nm	SPM, FWM, Raman scattering, Raman-shifted solitons, soliton self-frequency shifting (SSFS)
Lehtonen, M.; Genty, G.; Ludvigsen, H.; Kaivola, M.	2003	Birefringent photonic crystal fiber	798 nm, 100 fs, 140 mW (average, 80 MHz)	400–1750 nm	Raman scattering, soliton self-frequency shifting (SSFS), perturbation of multiple solutions, FWM

Hundertmark, H., D. Kracht, D. Wandt, C. Fallnich, V. V. R. K. Kumar, A. K. George, J. C. Knight, and P. St. J. Russell	2003	Photonic crystal fibers	1550 nm, 60 fs, 200 pJ	400–1750 nm	Raman scattering, soliton self-frequency shifting (SSFS)
Genty, G., M. Lehtonen, and H. Ludvigsen	2004a	Photonic crystal fibers	790 nm, 27 fs, 118 mW (average, 80 MHz)	450–1600 nm	Soliton formation, dispersive wave generation, XPM
Hilligsøe, K. M., T. V. Andersen, H. N. Paulsen, C. K. Nielsen, K. Mølmer, S. Keiding, R. Kristiansen, K. P. Hansen, and J. J. Larsen	2004	Photonic crystal fibers with two λ_{ZD}'s	790 nm, 80 fs, 700 pJ	Two peaks with inner edges at ~740 nm and ~950 nm, and two outer edges move outward with increasing pulse energy	SPM, phase-matched FWM
Genty, G., M. Lehtonen, H. Ludvigsen, and M. Kaivola,	2004b	Photonic crystal fibers with two λ_{ZD}'s	813 nm, 400 fs, 194 mW (average)	390–1800 nm	Raman scattering, amplification of dispersive wave generations, soliton self-frequency shifting (SSFS)
Hagan, C. L., J.W. Walewski, and S. T. Sanders	2006	ZBLAN fiber	1550 nm, 900 fs, 25 nJ	1800–3400 nm	SPM, FWM, Raman scattering
Domachuk, P., N. A. Wolchover, M. Cronin-Golomb, A. Wang, A. K. George, C.M.B. Cordeiro, J.C. Knight, and F. G. Omenetto	2008	Photonic crystal fibers	1550 nm, 100 fs, 1.9 nJ	789–4870 nm	***
Qin, G., X. Yan, C. Kito, M. Liao, C. Chaudhari, T. Suzuki, and Y. Ohishia	2009	Fluoride fiber	1450 nm, 180 fs, 4 MW (peak)	~350–6280 nm	SPM, Raman scattering, FWM

(continued)

Table 2.5 (continued)

Investigator	Year	Material	Pump wavelength, pulse width, power/energy	Spectrum	Process
Heidt, A. M., A. Hartung, and H. Bartelt	2010	Optical nanofibers	400 nm, 100 fs, 5 nJ	200–580 nm	SPM, OWB, FWM
Stark, S. P., J. C. Travers, and P. St. J. Russell,	2012	Photonic crystal fibers	800 nm, 130 fs, 2 nJ	280–1600 nm	SPM, soliton breathing, stimulated Raman scattering
Halir, R., Y. Okawachi, J. S. Levy, M. A. Foster, M. Lipson, and A. L. Gaeta	2012	Silicon nitride waveguides.	1300 nm, 200 fs, 160 pJ	665–2025 nm	SPM, third-harmonic generation, and self-steepening
Kartashov, D, S. Ališauskas, A. Pugžlys, A, Voronin, A, Zheltikov, M, Petrarca, P, Béjot, J, Kasparian, J.-P, Wolf, and A, Baltuška	2012	Argon (4.5 bars)	3900 nm, 80 fs, 0.1 TW (peak)	350–5000 nm	Filamentation, high-order nonlinear (n_2–n_{10}) SPM, THG, FTH
Petersen, C. R., U. Møller, I. Kubat, B. Zhou, S. Dupont, J. Ramsay, T. Benson, S. Sujecki, N. Abdel-Moneim, Z. Tang, D. Furniss, A. Seddon, and O. Bang,	2014	Step-index chalcogenide glass optical fiber	6300 nm, 100 fs, 2.29 MW (peak)	1400–13,300 nm	Soliton fission, dispersive wave generation, trapping potential, parametric amplification
Safioui, J., F. Leo, B. Kuyken, S.-P. Gorza, S. K. Selvaraja, R. Baets, P. Emplit, G. Roelkens, and S. Massar	2014	Amorphous silicon waveguides	1560 nm, 1 ps, 15.1 W	1470–1770 nm	SPM, MI, FWM

Klimczak, M., B. Siwicki, P. Skibiński, D. Pysz, R. Stępień, A.Heidt, C. Radzewicz, and R. Buczyński	2014	All-solid soft-glass photonic fiber	1550 nm, 75 fs, 200 kW	900–2300 nm	SPM, OWB, FWM
Epping, J. P., T. Hellwig, M. Hoekman, R. Mateman, A. Leinse, R. G. Heideman, A. van Rees, P. J.M. van der Slot, C. J. Lee, C. Fallnich, and K.-J. Boller	2015	High-confinement Si_3N_4 integrated optical waveguides	1064 nm, 115 fs, 590 pJ	470–2130 nm	SPM, XPM, FWM, self-steepening
Jiang, X., N. Y. Joly, M. A. Finger, F. Babic, G. K. L. Wong, J. C. Travers, and P. J. Russell	2015	ZBLAN photonic crystal fibre	1042 nm, 140 fs, 830 nJ	200–2500 nm	SPM, XPM, FWM, soliton fission, dispersive wave generation; THG, XPM from blue-shifted solitons
Belli, F., A. Abdolvand, W. Chang, J. C. Travers, and P. St. J. Russel	2015	Kagomé-PCF filled with hydrogen	805 nm, 30 fs, 2.5 uJ	124 to beyond 1200 nm	SPM, self-steepening, shock formation, Raman-XPM
Boggio, J. M. C., A. O. Moñux, D. Modotto, T. Fremberg, D. Bodenmüller, D. Giannone, M. M. Roth, T. Hansson, S. Wabnitz, E. Silvestre, and L. Zimmermann	2016	Multicladding silicon nitride (Si_xN_y) waveguides	1560 nm, 85 fs, 110 pJ	410–2400 nm	SPM, XPM, self-steepening, dispersive wave generation, phase-matched FWM, THG
Xiang, B, X. Ren, S. Ruan, L. Wang, P. Yan, H. Han, M. Wang, and J. Yin,	2016	Yttrium orthosilicate crystal	800 nm, 100 fs, 6 GW (peak)	380–1100 nm	SPM, XPM, MPE-enhanced SPM

(continued)

Table 2.5 (continued)

Investigator	Year	Material	Pump wavelength, pulse width, power/energy	Spectrum	Process
Wang, N., J.-H. Cai, X. Qi, S.-P. Chen, L.-J. Yang, and J. Hou	2018	Photonic crystal fibers	976 nm, 353 ps, 15.1 W (average, 4.5 MHz)	350–2400 nm	Soliton self-frequency shifting, FWM, dispersive wave generation, XPM
Adamu, A. I., Md. S. Habib, C. R. Petersen, J. E. A. Lopez, B. Zhou, A. Schülzgen, M. Bache, R. Amezcua-Correa, O. Bang, and C. Markos	2019	Ar-filled hollow-core antiresonant fiber	2460 nm, 100 fs, 8 μJ	200–4000 nm	SPM, soliton self-compression, dispersive wave generation
Yu, M., B. Desiatov, Y. Okawachi, A. L. Gaeta, and M. Loncar	2019	Lithium-niobate waveguide	1506 nm, 160 fs, 185 pJ	400–2400 nm	SPM, SHG, SHG-XPM, sum frequency generation
Zhang, N., X. Peng, Y. Wang, S. Dai, Y. Yuan, J. Su, G. Li, P. Zhang, P. Yang, and X. Wang	2019	Te-based chalcogenide tapered fiber	5500 nm, 150 fs, 22 mW (1 kHz)	1700–12,700 nm	SPM, OWB
Saini, T. S., T. H. Tuan, T. Suzuki, and Y. Ohishi	2020	Tapered chalcogenide fiber	2600 nm, 200 fs, 10.12 kW (peak)	1600–3700 nm	SPM, OWB

materials was reviewed in this chapter. These latter two processes are closely related to each other and are described by Baldeck et al. (Chap. 4) and Agrawal (Chap. 3).

In the early beginning days of supercontinuum generation using an 8-ps laser at 530 nm, typical Stokes sweeps were 4400 cm^{-1} in a calcite crystal of length 4 cm, 3900 cm^{-1} in a quartz crystal of length 4.5 cm, 1100 cm^{-1} in extradense flint glass of length 7.55 cm, 3900 cm^{-1} in NaCl of length 4.7 cm, and 4200 cm^{-1} in both BK-7 and LBC-1 glasses of length 8.9 cm. Sweeps on the anti-Stokes side were typically 6100 cm^{-1} in calcite, 5500 cm^{-1} in quartz, 7300 cm^{-1} in NaCl, and 7400 cm^{-1} in BK-7 and LBC-1 glasses. An infrared supercontinuum spanning the range from 3 to 14 μm can be obtained by passing an intense laser pulse generated from a CO_2 laser through GaAs, AgBr, ZnSe, and CdS crystals. Near- and medium-infrared spectral sweeps of 3200 cm^{-1} on the Stokes side and 4900 cm^{-1} on the anti-Stokes side can be realized by passing a strong 1.06-μm pulse through a KBr crystal of length 10 cm. Sweeps on the order of 1000 cm^{-1} are observed to both the red and blue sides of 530 nm in liquid argon. Similar spectral sweeps are observed in liquid and solid krypton arising from electronic mechanism for SPM. Using a picosecond laser train of wavelength 530 nm, the spectra were broadened up to 3000 cm^{-1} to either side of the laser frequency in a 5-cm-long magnetic $KNiF_3$ single crystal. Production of SPM near electronic levels of PrF_3 crystal and enhancement of supercontinuum in water by addition of Zn^{2+} and K^+ cations have been also discussed. The temporal properties of supercontinuum pulses have been described. Higher-order effects on SPM arising from dispersion, self-focusing, self-steepening, and initial pulse chirping were briefly described.

SPM will continue to be an important nonlinear process in science and technology and has been one of the most important ultrafast nonlinear optical processes for more than 50 years since the advent of ultrashort laser pulses.

In most recent developments (Alfano et al., 2021a), ultrasupercontinuum (USC) broadening has been theoretically stimulated from the slow nonelectronic response to the fifth- and third-order susceptibilities under the influence of an extremely high-intensity femtosecond laser pulse to produce spectra broadening changes extending from extreme UV to DC. The theoretical results show that a high-intensity pulse as high as on the order of ~10^{16} W/m^2 can influence the fourth-order refractive index arising from fifth-order susceptibility large enough that the nonlinear $n_4 {I_0}^2$ term to overtakes the $n_2 I_0$ term to produce the ultrasupercontinuum broadening in liquids such as CS_2 and rare-gas liquids such as Argon. There has been experimental verification that the supercontinuum extends from X-rays, UV to MIR by many researchers using various states of matter.

In addition, an electronic cloud distortion model is also proposed (Alfano et al., 2021b) based on the optical cycle response of rare-gas molecules to explain the High-order Harmonic Generation (HHG) and supercontinuum generation from the interaction of high-intensity ultrafast pulses. The theory reveals the salient experimental features of HHG: three regimes based on electronic self-phase modulation (ESPM) from nonlinear Kerr index n_2, the cutoff frequency using the method of the stationary phase on ESPM, and spectral broadening about the N harmonics supporting the theoretical ansatz presented in this paper with prior supporting

experimental results. The outcome from ESPM is a supercontinuum background superimposed with the sharp HHG which was experimentally observed before. The model also shows that the odd higher harmonic modes can be coupled in phase by Kerr index change to generation the attosecond laser pulses.

The uses of supercontinuum as an enabler will be important for many applications to understand the fundamentals of the underlying physics in biology, chemistry, condensed matter, and medicine processes. In communication and computation, the bandwidths of supercontinuum will enhance by increasing the bits/sec to unheard of limits!

A.1 Appendix: Nonlinear Wave Equation with Group Velocity Dispersion

We start with Maxwell equations for the electric and magnetic fields E and H in Gaussian units

$$\begin{aligned} \nabla \times \mathbf{E} &= -\tfrac{1}{c}\tfrac{\partial \mathbf{B}}{\partial t}, \\ \nabla \times \mathbf{H} &= \tfrac{1}{c}\tfrac{\partial \mathbf{D}}{\partial t} + \tfrac{4\pi}{c}\mathbf{J}, \\ \nabla \cdot \mathbf{D} &= 4\pi\rho \\ \nabla \cdot \mathbf{B} &= 0. \end{aligned} \tag{A.1}$$

The helping equations are $\mathbf{D} = \varepsilon\mathbf{E}$ and $\mathbf{B} = \mu\mathbf{H}$, and $\mathbf{J}$ and ρ are the current and charge densities, respectively. For nonmagnetic material, $\mathbf{B} \approx \mathbf{H}$. The refractive index of an isotropic material possessing nonlinearity can be written as

$$n(\omega) = [\varepsilon(\omega)]^{1/2} = n_0(\omega) + n_2|\mathbf{E}|^2, \tag{A.2}$$

where $n_0(\omega)$ is the linear refractive index, and n_2 the nonlinear refractive index. In the absence of sources, from Maxwell equations, one can readily obtain the wave equation

$$\nabla^2\mathbf{E}(\mathbf{r}, t) - \frac{1}{c^2}\frac{\partial^2}{\partial t^2}\mathbf{D}_L(\mathbf{r}, t) = \frac{2n_0n_2}{c^2}\frac{\partial^2}{\partial t^2}\left(|\mathbf{E}|^2\mathbf{E}(\mathbf{r}, t)\right), \tag{A.3}$$

where $\mathbf{D}_\mathrm{L}(\mathbf{r}, t)$ is the linear electric displacement vector. In obtaining the equation, we have used $\nabla \times (\nabla \times \mathbf{E}) = \nabla(\nabla \cdot \mathbf{E}) - \nabla^2\mathbf{E} \approx -\nabla^2\mathbf{E}$ and neglected the $(n_2)^2$ term.

The electric field can be written as

$$\mathbf{E}(\mathbf{r}, t) = \Phi(x, y)\,\mathbf{E}(z, t), \tag{A.4}$$

where $\Phi(x, y)$ is the transverse distribution function. Substitute Eq. (A.4) into the wave equation, and averaging over transverse coordinates, we have

$$\frac{\partial^2}{\partial z^2}\mathbf{E}(z,t) - \frac{1}{c}\frac{\partial^2}{\partial t^2}\mathbf{D}_L(z,t) = \frac{2n_0\overline{n}_2}{c^2}\frac{\partial^2}{\partial t^2}|\mathbf{E}(z,t)|^2\mathbf{E}(z,t). \tag{A.5}$$

We have neglected the $\partial^2/\partial x^2$ and $\partial\ ^2/\partial y\ ^2$ terms. The effective nonlinear refractive index $\overline{n}_2$ is

$$\overline{n}_2 = \frac{\int n_2\Phi^2(x,y)\,dxdy}{\int \Phi^2(x,y)\,dxdy} \approx \frac{1}{2}n_2. \tag{A.6}$$

Using a plane wave approximation with $(k_0z - \omega_0t)$ representation, a linearly polarized electric field propagating along z direction can be written as

$$\mathbf{E}(z,t) = \hat{e}A(z,t)\exp\left[i\left(k_0z - \omega_0t\right)\right], \tag{A.7}$$

where $\hat{e}$ is the unit vector of polarization of electric field, ω_0 the carrier frequency, k_0 the carrier wave number, and $A(z, t)$ the pulse envelope function. The form of $\mathbf{D}_L$ (z, t) becomes

$$\mathbf{D}_L(z,t) = \int_{-\infty}^{+\infty} n_0^2(\omega)\,\tilde{E}(z,\omega)\exp(-i\omega t)\,d\omega, \tag{A.8}$$

where

$$\tilde{E}(z,\omega) = \frac{1}{2\pi}\int_{-\infty}^{+\infty} E(z,t)\exp(i\omega t)\,dt. \tag{A.9}$$

If the $(\omega_0t - k_0z)$ representation is used, one obtains sign changes in the final reduced wave equation.

Using the foregoing equations, we can write the linear polarization term on the left-hand side of the one-dimensional wave equation as

$$\begin{aligned} &-\tfrac{1}{c^2}\tfrac{\partial^2}{\partial t^2}\mathbf{D}_L(z,t) = -\tfrac{1}{c^2}\textstyle\int_{-\infty}^{+\infty}\left(-\omega^2\right)n_0^2(\omega)\,\tilde{E}(z,\omega)\exp(-i\omega t)\,d\omega \\ &= \tfrac{1}{2\pi}\textstyle\int_{-\infty}^{\infty}\int_{-\infty}^{\infty}k^2(\omega)\,A\left(z,t'\right)\exp\left[i\omega\left(t'-t\right)\right]\exp\left[i\left(k_0z-\omega_0t'\right)\right]d\omega dt'. \end{aligned} \tag{A.10}$$

The derivation of the wave equation then proceeds by expanding $k^2(\omega)$ about the carrier frequency ω_0 in the form:

$$k^2(\omega) \approx k_0^2 + 2k_0k_0^{(1)}(\omega-\omega_0) + k_0k_P^{(2)}(\omega-\omega_0)^2 + \cdots, \tag{A.11}$$

where $k_0 = k(\omega_0)$ is the propagation constant, $k_0^{(1)} = \frac{\partial k}{\partial \omega}\big|_{\omega=\omega_0}$ is the inverse of group velocity, and $k_0^{(2)} = \frac{\partial^2 k}{\partial \omega}\Big|_{\omega=\omega_0}$ is the inverse of group velocity of dispersion. It is then possible to evaluate the integral of Eq. (A.10) by using the convenient delta function identities

$$\frac{1}{2\pi}\int_{-\infty}^{\infty} \exp\left[i\left(\omega-\omega_0\right)\left(t'-t\right)\right]\ d\omega = \delta\left(t'-t\right) \tag{A.12}$$

as well as

$$\frac{1}{2\pi}\int_{-\infty}^{\infty} \left(\omega-\omega_0\right)\exp\left[i\left(\omega-\omega_0\right)\left(t'-t\right)\right]\ d\omega = i\delta^{(1)}\left(t'-t\right), \tag{A.13}$$

and

$$\frac{1}{2\pi}\int_{-\infty}^{\infty} \left(\omega-\omega_0\right)^2\exp\left[i\left(\omega-\omega_0\right)\left(t'-t\right)\right]\ d\omega = -\delta^{(2)}\left(t'-t\right). \tag{A.14}$$

In these relations, $\delta^{(n)}(t)$ is an nth-order derivative of the Dirac delta function, with the property that

$$\int_{-\infty}^{\infty} \delta^{(n)}\left(t-t_0\right) f(t)dt = \frac{d^n f(t)}{\partial t^n}\Big|_{t=t_0} \tag{A.15}$$

when applied to a function $f(t)$. Substitute Eq. (A.11) into Eq. (A.10) and use Eqs. (A.12) to (A.15), the second term on the left-hand side of Eq. (1.5) becomes

$$\begin{aligned}
-\tfrac{1}{c^2}\tfrac{\partial^2}{\partial t^2}\mathbf{D}_L(z,t) &= \tfrac{1}{2\pi}\textstyle\int_{-\infty}^{\infty}\int_{-\infty}^{\infty}\left[k_0^2 + 2k_0k_0^{(1)}\left(\omega-\omega_0\right) + k_0k_0^{(2)}(\omega-\omega_0)^2\right]A\left(z,t'\right)\\
&\quad\times\exp\left[i\omega\left(t'-t\right)\right]\exp\left[i\left(k_0z-\omega_0t\right)\right]d\omega dt'\\
&= \textstyle\int_{-\infty}^{\infty}\left[k_0^2\delta\left(t'-t\right) + i2k_0k_0^{(1)}\delta^{(1)}\left(t'-t\right) - k_0k_0^{(2)}\delta^{(2)}\left(t'-t\right)\right]A\left(z,t'\right)\\
&\quad\times\exp\left[i\left(k_0z-\omega_0t\right)\right]dt'\\
&= \left[k_0^2A + i2k_0k_0^{(2)}\tfrac{\partial A}{\partial t} - k_0k_0^{(2)}\tfrac{\partial^2 A}{\partial t^2}\right]\exp\left[i\left(k_0z-\omega_0t\right)\right].
\end{aligned} \tag{A.16}$$

Neglecting the second derivative of $A(z,t)$ with respect to z and $\frac{\partial^2}{\partial t^2}|A(z,t)|^2$. $A(z,t)$, the first term on the left-hand side and the term on the right-hand side of Eq. (1.5) are simply

$$\frac{\partial^2 E(z,t)}{\partial z^2} \approx \left[-k_0^2A(z,t) + i2k_0\frac{\partial A(z,t)}{\partial z}\right]\exp\left[i\left(k_0z-\omega_0t\right)\right], \tag{A.17}$$

and

$$\frac{2n_0\bar{n}_2}{c^2}\frac{\partial^2}{\partial t^2}|E|^2E \approx -\frac{n_0n_2\omega_0^2}{c^2}|A|^2A\exp\left[i\left(k_0z-\omega_0t\right)\right], \tag{A.18}$$

respectively.

Inserting Eqs. (A.16) to (A.18) into Eq. (1.5), the wave equation for electric field reduces to the wave equation for the pulse envelope

$$i\left(\frac{\partial A}{\partial z}+\frac{1}{v_g}\frac{\partial A}{\partial t}\right)-\frac{1}{2}k_0^{(2)}\frac{\partial^2A}{\partial t^2}+\frac{\omega_0}{2c}n_2|A|^2A=0, \tag{A.19}$$

where $v_g \equiv 1/k_0^{(1)}$ is the group velocity. In Eq. (A.19), the first two terms describe the envelope propagation at the group velocity v_g; the third term determines the temporal pulse broadening due to group velocity dispersion; the fourth characterizes the second order of the nonlinear polarization, which is responsible for the self-phase modulation effect and spectral broadening. Neglecting the group velocity dispersion term in Eq. (A.19), we obtain

$$\frac{\partial A}{\partial z}+\frac{1}{v_g}\frac{\partial A}{\partial t}=i\frac{\omega_0}{2c}n_2|A|^2A. \tag{A.20}$$

This is Eq. (2.2).

References

Adair, R., Chase, L. L., & Payne, S. A. (1989). Nonlinear refractive index of optical crystals. *Physical Review B, 39*, 3337–3350.

Adamu, A. I., Habib, M. S., Petersen, C. R., Lopez, J. E. A., Zhou, B., Schülzgen, A., Bache, M., Amezcua-Correa, R., Bang, O., & Markos, C. (2019). Deep-UV to mid-IR supercontinuum generation driven by mid-IR ultrashort pulses in a gas-filled hollow-core fiber. *Scientific Reports, 9*, 4446.

Agrawal, G. P., & Potasek, M. J. (1986). Nonlinear pulse distortion in single-mode optical fibers at the zero-dispersion wavelength. *Physical Review A, 33*, 1765–1776.

Akhemediev, N., & Karlsson, M. (1995). Cherenkov radiation emitted by solitons in optical fibers. *Physical Review A, 51*, 2602–2607.

Alfano, R. R. (1972). *Interaction of picosecond laser pulses with matter. GTE Technical Report TR 72–330*. Published as Ph.D. thesis at New York University.

Alfano, R. R. (1986). The ultrafast supercontinuum laser source. In *Proceeding of the international conference laser '85* (pp. 110–122). STS Press.

Alfano, R. R., & Shapiro, S. L. (1970a). Emission in the region 4000–7000 A via four-photon coupling in glass. Phys. Rev. Lett. 24, 584–587; Observation of self-phase modulation and small scale filaments in crystals and glasses. Phys. Rev. Lett. 24, 592–594; Direct distortion of electronic clouds of rare-gas atoms in intense electric fields. *Physical Review Letters, 24*, 1219–1222.

Alfano, R. R., & Shapiro, S. L. (1970b). Picosecond spectroscopy using the inverse Raman effect. *Chemical Physics Letters, 8*, 631–633.

Alfano, R. R., Gersten, J., Zawadzkas, G., & Tzoar, N. (1974). Self-phase-modulation near the electronic resonances of a crystal. *Physical Review A, 10*, 698–708.

Alfano, R. R., Ho, P. P., Fleury, P., & Guggeneheim, H. (1976). Nonlinear optical effects in antiferromagnetic $KNiF_3$. *Optics Communication, 19*, 261–264.

Alfano, R. R., Wang, Q. Z., Jimbo, T., & Ho, P. P. (1987). Induced spectral broadening about a second harmonic generated by an intense primary ultrashort laser pulse in ZnSe crystals. *Physical Review A, 35*, 459–462.

Alfano, R. R., Mazhar, S. F. B., Sharonov, M., & Shi, L. (2021a). Ultra-supercontinuum and enhanced ultra-supercontinuum broadening from fifth- and third-order susceptibility from self-phase modulation for isotropic media with extremely intense femtosecond pulses. *Submitted to Optical Letter*.

Alfano, R. R., Mazhar, S. F. B., Sharonov, M., & Shi, L. (2021b). Higher harmonic and supercontinuum generation arising from electronic self-phase modulation under extreme ultrafast laser pulses. *Submitted to Scientific Reports*.

Allen, M. G. (1998). Diode laser absorption sensors for gas-dynamic and combustionflows. *Measurement Science and Technology, 9*, 545–562.

Auston, D. H. (1977). In S. L. Shapiro (Ed.), *Ultrafast light pulses*. Springer.

Baldeck, P. L., Raccah, F., & Alfano, R. R. (1987a). Observation of self-focusing in optical fibers with picosecond pulses. *Optics Letters, 12*, 588–589.

Baldeck, P. L., Ho, P. P., & Alfano, R. R. (1987b). Effects of self-, induced-, and cross-phase modulations on the generation of ps and fs white light supercontinuum. *Revue de Physique Appliquée, 22*, 1877–1894.

Belli, F., Abdolvand, A., Chang, W., Travers, J. C., St, P., & Russell, J. (2015). Vacuum-ultraviolet to infrared supercontinuum in hydrogen-filled photonic crystal fiber. *Optica, 2*, 292–300.

Birks, T. A., Wadsworth, W. J., & Russell, P. S. J. (2000). Supercontinuum generation in tapered fibers. *Optics Letters, 25*, 1415–1417.

Boggio, J. M. C., Moñux, A. O., Modotto, D., Fremberg, T., Bodenmüller, D., Giannone, D., Roth, M. M., Hansson, T., Wabnitz, S., Silvestre, E., & Zimmermann, L. (2016). Dispersion-optimized multicladding silicon nitride waveguides for nonlinear frequency generation from ultraviolet to mid-infrared. *Journal of the Optical Society of America B: Optical Physics, 33*, 2402–2413.

Bokov, O. G. (1974). Theory of the nonlinear refractive index of liquids. *Soviet Physics – JETP, 40*, 923–928.

Boyle, L. L., Buckingham, A. D., Disch, R. L., & Dunmur, D. A. (1966). Higher polarizability of the helium atom. *The Journal of Chemical Physics, 45*, 1318–1323.

Bree, C., Demircan, A., & Steinmeyer, G. (2010). Method for computing the nonlinear refractive index via Keldysh theory. *IEEE Journal of Quantum Electronics, 46*, 433–437.

Brewer, R. G., & Lee, C. H. (1968). Self-trapping with picosecond light pulses. *Physical Review Letters, 21*, 267–270.

Buckingham, A. D. (1955). Theoretical studies of the Kerr effect II: The influence of pressure. *The Proceedings of the Physical Society. Section A, 68*, 910–919.

Buckingham, A. D., & Hibbard, P. G. (1968). Polarizability and hyperpolarizability of the helium atom. *Symposia of the Faraday Society, 2*, 41–47.

Busch, G. E., Jones, R. P., & Rentzepis, P. M. (1973). Picosecond spectroscopy using a picosecond continuum. *Chemical Physics Letters, 18*, 178–185.

Chinn, S. R., Zeiger, H., & O'Connor, J. (1971). Two-magnon Raman scattering and exchange interactions in antiferromagnetic $KNiF_3$ and K_2NiF_4 and ferrimagnetic $RbNiF_3$. *Physical Review B: Condensed Matter and Materials Physics, 3*, 1709–1735.

Coen, S., Chau, A. H. L., Leonhardt, R., Harvey, J. D., Knight, J. C., Wadsworth, W. J., & Russell, P. S. J. (2001). White-light supercontinuum generation with 60-ps pump pulses in a photonic crystal fiber. *Optics Letters, 26*, 1356–1358.

Colley, C. S., Hebden, J. C., & Delpy, D. T. (2007). Mid-infrared optical coherence tomography. *The Review of Scientific Instruments, 78*, 123108.

Corkum, P., Ho, P. P., Alfano, R. R., & Manassah, J. (1985). Generation of infrared supercontinuum covering 3–14 μm in dielectrics and semiconductors. *Optics Letters, 10*, 624–626.

DeMartini, F., Townes, C. H., Gustafson, T. K., & Kelly, P. L. (1967). Self-steepening of light pulses. *Physics Review, 164*, 312–322.

Domachuk, P., Wolchover, N. A., Cronin-Golomb, M., Wang, A., George, A. K., Cordeiro, C. M. B., Knight, J. C., & Omenetto, F. G. (2008). Over 4000 nm bandwidth of mid-IR supercontinuum generation in sub-centimeter segments of highly nonlinear tellurite PCFs. *Optics Express, 16*, 7161–7168.

Dorsinville, R., Delfyett, P., & Alfano, R. R. (1987). Generation of 3 ps pulses by spectral selection of the supercontinuum generated by a 30 ps second harmonic Nd: YAG laser pulse in a liquid. *Applied Optics, 27*, 16–18.

Dremetsika, E., Dlubak, B., Gorza, S.-P., Ciret, C., Martin, M.-B., Hofmann, S., Seneor, P., Dolfi, D., Massar, S., Emplit, P., & Kockaert, P. (2016). Measuring the nonlinear refractive index of graphene using the optical Kerr effect method. *Optics Letters, 41*, 3281–3284.

Dudley, J. M., Provino, L., Grossard, N., Maillotte, H., Windeler, R. S., Eggleton, B. J., & Coen, S. (2002). Supercontinuum generation in air-silica microstructured fibers with nanosecond and femtosecond pulse pumping. *Journal of the Optical Society of America B: Optical Physics, 19*, 765–771.

Dudley, J. M., Genty, G., & Coen, S. (2006). Supercontinuum generation in photonic crystal fiber. *Reviews of Modern Physics, 78*, 1135–1184.

Dunsby, C., Lanigan, P. M. P., McGinty, J., Elson, D. S., Requejo-Isidro, J., Munro, I., Galletly, N., McCann, F., Treanor, B., Onfelt, B., Davis, D. M., Neil, M. A. A., & French, P. M. W. (2004). An electronically tunable ultrafast laser source applied to fluorescence imaging and fluorescence lifetime imaging microscopy. *Journal of Physics D: Applied Physics, 37*, 3296–3303.

Eggleton, B. J., Luther-Davies, B., & Richardson, K. (2011). Chalcogenide photonics. *Nature Photonics, 5*, 141–148.

Epping, J. P., Hellwig, T., Hoekman, M., Mateman, R., Leinse, A., Heideman, R. G., van Rees, A., van der Slot, P. J. M., Lee, C. J., Fallnich, C., & Boller, K.-J. (2015). On-chip visible-to-infrared supercontinuum generation with more than 495 THz spectral bandwidth. *Optics Express, 23*, 19596–19604.

Ere-Tassou, M., Przygodzki, C., Fertein, E., & Delbarre, H. (2003). Femtosecond laser source for real-time atmospheric gas sensing in the UV – Visible. *Optics Communication, 220*, 215–221.

Fleury, P. A., Hayes, W., & Guggenheim, H. J. (1975). Magnetic scattering of light in $K(NiMg)F_3$. *Journal of Physics C, 8*, 2183–2189.

Fork, R. L., Shank, C. V., Hirliman, C., Yen, R., & Tomlinson, J. (1983). Femtosecond white-light continuum pulse. *Optics Letters, 8*, 1–3.

Fork, R. L., Brito Cruz, C. H., Becker, P. C., & Shank, C. V. (1987). Compression of optical pulses to six femtoseconds by using cubic phase compensation. *Optics Letters, 12*, 483–485.

Ganeev, R. A., Ryasnyansky, A. I., Tugushev, R. I., & Usmanov, T. (2003). Investigation of nonlinear refraction and nonlinear absorption of semiconductor nanoparticle solutions prepared by laser ablation. *Journal of Optics A: Pure and Applied Optics, 5*, 409–417.

Genty, G., Lehtonen, M., Ludvigsen, H., Broeng, J., & Kaivola, M. (2002). Spectral broadening of femtosecond pulses into continuum radiation in microstructured fibers. *Optics Express, 10*, 1083–1098.

Genty, G., Lehtonen, M., & Ludvigsen, H. (2004a). Effect of cross-phase modulation on supercontinuum generated in microstructured fibers with sub-30 fs pulses. *Optics Express, 12*, 4614–4624.

Genty, G., Lehtonen, M., Ludvigsen, H., & Kaivola, M. (2004b). Enhanced bandwidth of supercontinuum generated in microstructured fibers. *Optics Express, 12*, 3471–3480.

Gersten, J., Alfano, R., & Belic, M. (1980). Combined stimulated Raman scattering in fibers. *Physical Review A, 21*, 1222–1224.

Gomes, A. S. L., Gouveia-Neto, A. S., Taylor, J. R., Avramopoulos, H., & New, G. H. C. (1986). Optical pulse narrowing by the spectral windowing of self-phase modulated picosecond pulses. *Optics Communication, 59*, 399.

Hagan, C. L., Walewski, J. W., & Sanders, S. T. (2006). Generation of a continuum extending to the midinfrared by pumping ZBLAN fiber with an ultrafast 1550-nm source. *IEEE Photonics Technology Letters, 18*, 91–93.

Halir, R., Okawachi, Y., Levy, J. S., Foster, M. A., Lipson, M., & Gaeta, A. L. (2012). Ultrabroadband supercontinuum generation in a CMOS-compatible platform. *Optics Letters, 37*, 1685–1687.

Hartl, I., Li, X. D., Chudoba, C., Ghanta, R. K., Ko, T. H., Fujimoto, J. G., Ranka, J. K., & Windeler, R. S. (2001). Ultrahigh-resolution optical coherence tomography using continuum generation in an air–silica microstructure optical fiber. *Optics Letters, 26*, 608–610.

Heidt, A. M., Hartung, A., & Bartelt, H. (2010). Deep ultraviolet supercontinuum generation in optical nanofibers by femtosecond pulses at 400-nm wavelength. *Proceedings of SPIE, 7714*(771407), 1–9.

Hellwarth, R. W., Cherlow, J., & Yang, T. T. (1975). Origin and frequency dependence of nonlinear optical susceptibilities of glasses. *Physical Review B, 11*, 964–967.

Hilligsøe, K. M., Andersen, T. V., Paulsen, H. N., Nielsen, C. K., Mølmer, K., Keiding, S., Kristiansen, R., Hansen, K. P., & Larsen, J. J. (2004). Supercontinuum generation in a photonic crystal fiber with two zero dispersion wavelengths. *Optics Express, 12*, 1045–1054.

Ho, P. P., & Alfano, R. R. (1978). Coupled molecular reorientational relaxation kinetics in mixed binary liquids directly measured by picosecond laser techniques. *The Journal of Chemical Physics, 68*, 4551–4563.

Ho, P. P., & Alfano, R. R. (1979). Optical Kerr effect in liquids. *Physical Review A, 20*, 2170–4564.

Ho, P. P., Li, Q. X., Jimbo, T., Ku, Y. L., & Alfano, R. R. (1987). Supercontinuum pulse generation and propagation in a liquid carbon tetrachloride. *Applied Optics, 26*, 2700–2702.

Holzwarth, R., Udem, T., Hansch, T. W., Knight, J. C., Wadsworth, W. J., & Russell, P. S. J. (2000). Optical frequency synthesizer for precision spectroscopy. *Physical Review Letters, 85*, 2264–2267.

Hsiung, P.-L., Chen, Y., Ko, T. H., Fujimoto, J. G., de Matos, C. J. S., Popov, S. V., Taylor, J. R., & Gapontsev, V. P. (2004). Optical coherence tomography using a continuous-wave, high-power, Raman continuum light source. *Optics Express, 12*, 5287–5295.

Hundertmark, H., Kracht, D., Wandt, D., Fallnich, C., Kumar, V. V. R. K., George, A. K., Knight, J. C., St, P., & Russell, J. (2003). Supercontinuum generation with 200 pJ laser pulses in an extruded SF6 fiber at 1560 nm. *Optics Express, 11*, 3196–3201.

Hurlbut, W. C., Lee, Y.-S., Vodopyanov, K. L., Kuo, P. S., & Fejer, M. M. (2007). Multiphoton absorption and nonlinear refraction of GaAs in the mid-infrared. *Optics Letters, 32*, 668–670.

Husakou, A. V., & Herrmann, J. (2001). Supercontinuum generation of higher-order solitons by fission in photonic crystal fibers. *Physical Review Letters, 87*, 203901-1–203901-4.

Husakou, A. V., & Herrmann, J. (2002). Supercontinuum generation, four-wave mixing, and fission of higherorder solitons in photonic-crystal fibers. *Journal of the Optical Society of America B: Optical Physics, 19*, 2171–2182.

Husakou, A. V., & Herrmann, J. (2003). Supercontinuum generation in photonic crystal fibers made from highly nonlinear glasses. *Applied Physics B: Lasers and Optics, 77*, 227–234.

Jiang, X., Joly, N. Y., Finger, M. A., Babic, F., Wong, G. K. L., Travers, J. C., St, P., & Russell, J. (2015). Deep-ultraviolet to mid-infrared supercontinuum generated in solid-core ZBLAN photonic crystal fiber. *Nature Photonics, 9*, 133–139.

Jimbo, T., Caplan, V. L., Li, Q. X., Wang, Q. Z., Ho, P. P., & Alfano, R. R. (1987). Enhancement of ultrafast supercontinuum generation in water by addition of Zn^{2+} and K^{+} cations. *Optics Letters, 12*, 477–479.

Jones, D. J. (2000). Carrier-envelope phase control of femtosecond mode-locked lasers and direct optical frequency synthesis. *Science, 288*, 635–639.

Jones, W. J., & Stoicheff, B. P. (1964). Inverse Raman spectra: Induced absorption at optical frequencies. *Physical Review Letters, 13*, 657–659.

Kartashov, D., Ališauskas, S., Pugžlys, A., Voronin, A., Zheltikov, A., Petrarca, M., Béjot, P., Kasparian, J., Wolf, J.-P., & Baltuška, A. (2012). White light generation over three octaves by femtosecond filament at 3.9 μm in argon. *Optics Letters, 37*, 3456–3458.

Kerr, J. (1875). A new relation between electricity and light: Dielectrified media birefringent. *Philosophical Magazine, 50*, 337–348.

Klimczak, M., Siwicki, B., Skibiński, P., Pysz, D., Stępień, R., Heidt, A., Radzewicz, C., & Buczyński, R. (2014). Coherent supercontinuum generation up to 2.3 μm in all-solid soft-glass photonic crystal fibers with flat all-normal dispersion. *Optics Express, 28*, 18824–18832.

Knight, J. C., Birks, T. A., Russell, P. S. J., & Atkin, D. M. (1996). All-silica single-mode optical fiber with photonic crystal cladding. *Optics Letters, 21*, 1547–1549.

Knox, K., Shulman, R. G., & Sugano, S. (1963). Covalency effects in $KNiF_3$. II. Optical studies. *Physics Review, 130*, 512–516.

Kobayashi, T. (1979). Broadband picosecond light generation in phosphoric acid by a mode-locked laser. *Optics Communication, 28*, 147–149.

Lallemand, P. (1966). Temperature variation of the width of stimulated Raman lines in liquids. *Applied Physics Letters, 8*, 276–277.

Lehtonen, M., Genty, G., Ludvigsen, H., & Kaivola, M. (2003). Supercontinuum generation in a highly birefringent microstructured fiber. *Applied Physics Letters, 82*, 2197–2199.

Levenson, M. D., & Bloembergen, N. (1974). Dispersion of the nonlinear optical susceptibility tensor in centrosymmetric media. *Physical Review B, 10*, 4447–4463.

Li, Q. X., Jimbo, T., Ho, P. P., & Alfano, R. R. (1986). Temporal distribution of picosecond supercontinuum generated in a liquid measured by a streak camera. *Applied Optics, 25*, 1869–1871.

Lu, X., Liu, Q., Liu, Z., Sun, S., Ding, P., Ding, B., & Hu, B. (2012). Measurement of nonlinear refractive index coefficient using emission spectrum of filament induced by gigawatt-femtosecond pulse in BK7 glass. *Applied Optics, 51*, 2045–2050.

Magde, D., & Windsor, M. W. (1974). Picosecond flash photolysis and spectroscopy: 3,3′-diethyloxadicarbocyanine iodide (DODCI). *Chemical Physics Letters, 27*, 31–36.

Maker, P. D., & Terhune, R. W. (1965). Study of optical effects due to an induced polarization third order in the electric field strength. *Physics Review, 137*, A801–A818.

Maker, P. D., Terhune, R. W., & Savage, C. M. (1964). Intensity-dependent changes in the refractive index of liquids. *Physical Review Letters, 12*, 507–509.

Marcuse, D. (1980). Pulse distortion in single-mode optical fibers. *Applied Optics, 19*, 1653–1660.

McTague, J., Fleury, P., & DuPre, D. (1969). Intermolecular light scattering in liquids. *Physics Review, 188*, 303–308.

Milam, D., Webert, M. J., & Glass, A. J. (1977). Nonlinear refractive index of fluoride crystals, *Applied Physics Letters, 31*, 822–824.

Morioka, T., Mori, K., & Saruwatari, M. (1993). More than 100-wavelength-channel picosecond optical pulse generation from single laser source using supercontinuum in optical fibers. *Electronics Letters, 29*, 862–864.

Nakashima, N., & Mataga, N. (1975). Picosecond flash photolysis and transient spectral measurements over the entire visible, near ultraviolet and near infrared regions. *Chemical Physics Letters, 35*, 487–492.

Petersen, C. R., Møller, U., Kubat, I., Zhou, B., Dupont, S., Ramsay, J., Benson, T., Sujecki, S., Abdel-Moneim, N., Tang, Z., Furniss, D., Seddon, A., & Bang, O. (2014). Mid-infrared supercontinuum covering the 1.4–13.3 μm molecular fingerprint region using ultra-high NA chalcogenide step-index fibre. *Nature Photonics, 8*, 830–834.

Petersen, C. R., Moselund, P. M., Huot, L., Hooper, L., & Bang, O. (2018a). Towards a table-top synchrotron based on supercontinuum generation. *Infrared Physics & Technology, 91*, 182–186.

Petersen, C. R., Prtljaga, N., Farries, M., Ward, J., Napier, B., Lloyd, G. R., Nallala, J., Stone, N., & Bang, O. (2018b). Mid-infrared multispectral tissue imaging using a chalcogenide fiber supercontinuum source. *Optics Letters, 43*, 999–1002.

Popov, A. A., Sherstnev, V. V., Yakovlev, Y. P., Baranov, A. N., & Alibert, C. (1997). Powerful mid-infrared light emitting diodes for pollution monitoring. *Electronics Letters, 33*, 86–88.

Provino, L., Dudley, J. M., Maillotte, H., Grossard, N., Windeler, R. S., & Eggleton, B. J. (2001). Compact broadband continuum source based on microchip laser pumped microstructured fibre. *Electronics Letters, 37*, 558–560.

Qin, G., Yan, X., Kito, C., Liao, M., Chaudhari, C., Suzuki, T., & Ohishia, Y. (2009). Ultrabroadband supercontinuum generation from ultraviolet to 6.28 μm in a fluoride fiber. *Applied Physics Letters, 95*, 161103.

Ranka, J. K., Windeler, R. S., & Stentz, A. J. (2000). Visible continuum generation in air-silica microstructure optical fibers with anomalous dispersion at 800 nm. *Optics Letters, 25*, 25–27.

Rau, I., Kajzar, F., Luc, J., Sahraoui, B., & Boudebs, G. (2008). Comparison of Z-scan and THG derived nonlinear index of refraction in selected organic solvents. *Journal of the Optical Society of America B: Optical Physics, 25*, 1738–1747.

Riedle, E., Bradler, M., Wenninger, M., Sailer, C. F., & Pugliesi, I. (2013). Electronic transient spectroscopy from the deep UV to the NIR: Unambiguous disentanglement of complex processes. *Faraday Discussions, 163*, 139–158.

Russell, P. S. J., Knight, J. C., Birks, T. A., & Atkin, D. M. (1996). All-silica single-mode optical fiber with photonic crystal cladding. *Optics Letters, 21*, 1547–1549.

Russell, P. S. J., Birks, T. A., & Knight, J. C. (1997). Endlessly single-mode photonic crystal fiber. *Optics Letters, 22*, 961–963.

Safioui, J., Leo, F., Kuyken, B., Gorza, S.-P., Selvaraja, S. K., Baets, R., Emplit, P., Roelkens, G., & Massar, S. (2014). Supercontinuum generation in hydrogenated amorphous silicon waveguides at telecommunication wavelengths. *Optics Express, 22*, 3089–3097.

Saini, T. S., Tuan, T. H., Suzuki, T., & Ohishi, Y. (2020). Coherent Mid-IR supercontinuum generation using tapered chalcogenide step-index optical fiber: Experiment and modelling. *Scientific Reports, 10*, 2236.

Sanders, S. T. (2002). Wavelength-agile fiber laser using group-velocity dispersion of pulsed supercontinua and application to broadband absorption spectroscopy. *Applied Physics B, 75*, 799–802.

Schliesser, A., Picqué, N., & Hänsch, T. W. (2012). Mid-infrared frequency combs. *Nature Photonics, 6*, 440–449.

Schnatz, H., & Hollberg, L. W. (2003). Optical frequency combs: From frequency metrology to optical phase control. *The IEEE Journal of Selected Topics in Quantum Electronics, 9*, 1041–1058.

Seddon, A. B. (2011). A prospective for new mid-infrared medical endoscopy using chalcogenide glasses. *International Journal of Applied Glass Science, 2*, 177–191.

Shank, C. V., Fork, R. L., Yen, R., & Stolen, R. H. (1982). Compression of femtosecond optical pulses. *Applied Physics Letters, 40*, 761–763.

Sharma, D. K., Yid, R. W., Williams, D. F., Sugamori, S. E., & Bradley, L. L. T. (1976). Generation of an intense picosecond continuum in D_2O by a single picosecond 1.06 μ pulse. *Chemical Physics Letters, 41*, 460–465.

Shen, Y. R. (1984). *The principles of nonlinear optics*. Wiley.

Stark, S. P., Travers, J. C., St, P., & Russell, J. (2012). Extreme supercontinuum generation to the deep UV. *Optics Letters, 37*, 770–772.

Stokowski, S., & Vaez-Iravani, M. (1998). Wafer inspection technology challenges for ULSI manufacturing. In *AIP conference proceedings* (Vol. 449, pp. 405–415). AIP.

Stolen, R. H., & Lin, C. (1978). Self-phase modulation in silica optical fibers. *Physical Review A, 17*, 1448–1453.

Takara, H., Ohara, T., Mori, K., Sato, K., Yamada, E., Inoue, Y., Shibata, T., Abe, M., Morioka T., & Sato, K-I. (2005). More than 1000 channel optical frequency chain generation from single supercontinuum source with 12.5GHz channel spacing. *Electronics Letters, 36*, 2089–2090.

Topp, M. R., & Orner, G. C. (1975). Group velocity dispersion effects in picoseconds spectroscopy. *Optics Communication, 13*, 276.

Walrafen, G. E. (1972). Stimulated Raman scattering and the mixture model of water structure. *Advances in Molecular Relaxation Processes, 3*, 43–49.

Wang, Q. Z., Ji, D., Yang, L., Ho, P. P., & Alfano, R. R. (1989). Self-phase modulation in multimode optical fibers with modest high power. *Optics Letters, 14*(11), 578–580.

Wang, Q. Z., Liu, Q. D., Liu, D., Ho, P. P., & Alfano, R. R. (1994a). High-resolution spectra of self-phase modulation in optical fibers. *Journal of the Optical Society of America B: Optical Physics, 11*, 1084–1089.

Wang, Q. Z., Liu, Q. D., Ho, P. P., Walge, E. K., & Alfano, R. R. (1994b). High-resolution spectra of cross-phase modulation in optical fibers. *Optics Letters, 19*, 1636–1638.

Wang, D., Leng, Y., & Xu, Z. (2013). Measurement of nonlinear refractive index coefficient of inert gases with hollow-core fiber. *Applied Physics B: Lasers and Optics, 111*, 447–452.

Wang, N., Cai, J.-H., Qi, X., Chen, S.-P., Yang, L.-J., & Hou, J. (2018). Ultraviolet-enhanced supercontinuum generation with a mode-locked Yb-doped fiber laser operating in dissipative-solitonresonance region. *Optics Express, 26*, 1689–1696.

Wegener, J., Wilsonand, R. H., & Tapp, H. S. (1999). Mid-infrared spectroscopy for food analysis: Recent new applications and relevant developments in sample presentation methods. *Trends in Analytical Chemistry, 18*, 85–93.

Xiang, B., Ren, X., Ruan, S., Wang, L., Yan, P., Han, H., Wang, M., & Yin, J. (2016). Visible to near-infrared supercontinuum generation in yttrium orthosilicate bulk crystal and ion implanted planar waveguide. *Scientific Reports, 6*, 31612-1–31612-7.

Yang, G., & Shen, Y. R. (1984). Spectral broadening of ultrashort pulse in a nonlinear medium. *Optics Letters, 9*, 510–512.

Yariv, A. (1975). *Quantum electronics* (2nd ed.p. 499). Wiley.

Yu, W., Alfano, R. R., Sam, C. L., & Seymour, R. J. (1975). Spectral broadening of picosecond 1.06 mm pulse in KBr. *Optics Communication, 14*, 344.

Yu, M., Desiatov, B., Okawachi, Y., Gaeta, A. L., & Loncar, M. (2019). Coherent two-octave-spanning supercontinuum generation in lithium-niobate waveguides. *Optics Letters, 44*, 1222–1225.

Zhang, N., Peng, X., Wang, Y., Dai, S., Yuan, Y., Su, J., Li, G., Zhang, P., Yang, P., & Wang, X. (2019). Ultrabroadband and coherent mid-infrared supercontinuum generation in Te-based chalcogenide tapered fiber with all-normal dispersion. *Optics Express, 27*, 10311–10319.